Function of RIM4 in cerebellar circuits

Dissertation
zur
Erlangung des Doktorgrades (Dr. rer. nat.)
der
Mathematisch-Naturwissenschaftlichen Fakultät
der
Rheinischen Friedrich-Wilhelms-Universität Bonn

vorgelegt von

Eva Maria Breithausen
geb. Schönhense

aus

Werl

Bonn, Mai 2023

Angefertigt mit Genehmigung der Mathematisch-Naturwissenschaftlichen Fakultät

der Rheinischen Friedrich-Wilhelms-Universität Bonn

1. Gutachterin:	**Prof. Dr. Susanne Schoch McGovern**
2. Gutachter:	**Prof. Dr. Albert Haas**

Tag der Promotion:	24.11.2023
Erscheinungsjahr:	2023

Index

List of Figures

List of Tables

1 Abstract

RIMs (Rab3-interacting molecules) are multidomain proteins, enriched at presynaptic active zones. The large isoforms (RIM1 α/β, RIM2 α/β) have been shown to be important for mediating presynaptic active zone function by coupling synaptic vesicles to voltage-gated calcium channels and by regulating neurotransmitter release as well as presynaptic plasticity. The functional role of the small RIM isoforms, RIM3 and RIM4, in particular *in vivo* has so far remained unresolved. Previous studies showed that constitutive RIM4 knock-out (KO) mice developed spontaneous episodes of strong hind limb impairments with rapid movements accompanied by weight loss after weaning, whereas constitutive RIM3 KO mice did not exhibit obvious motor impairments.

Since movement generation and execution is mainly processed in cerebellar structures, we focused in this study on the potential functions of RIM4 in cerebellar circuits. Using mice expressing lacZ under the endogenous RIM4- or RIM3-promotor, we show that RIM4 as well as RIM3 are non-uniformly distributed on a cellular level in the mouse brain. Highest RIM4 expression was observed in the cerebellum and highest RIM3 expression was observed in the thalamus. Furthermore, experiments in primary neuronal cultures unveiled that *Rims4* gene expression was regulated by increased neuronal activity. In addition, we showed in this study that the deletion of RIM4 did not alter the cerebellar and cortical transcriptome and proteome of constitutive RIM4 KO mice.

In order to examine if the observed motor impairments of constitutive RIM4 KO mice resulted from a dysfunction in the cerebellum, we generated $\text{Pcp2}_{\text{Mpin}}\text{-Cre}_{\text{tg}}\text{:RIM4}^{\text{fl/fl}}$ mice, in which Cre recombination is mainly restricted to cerebellar Purkinje cells. These mice develop episodically occurring motor impairments similar to constitutive RIM4 KO mice. To further characterize this mouse line and the occurrence of the episodic motor impairments, *in vivo* single unit recordings in freely moving $\text{Pcp2}_{\text{Mpin}}\text{-Cre}_{\text{tg}}\text{:RIM4}^{\text{fl/fl}}$ mice were performed. These recordings unveiled no alterations in cerebellar firing frequency under baseline conditions. However, the cerebellar firing frequency was reduced during the motor episodes of the $\text{Pcp2}_{\text{Mpin}}\text{-Cre}_{\text{tg}}\text{:RIM4}^{\text{fl/fl}}$ mice, induced by a single injection of caffeine. Taken together, we propose that RIM4 in Purkinje cells is required to maintain normal electrophysiological properties of the cerebellar network and in turn, RIM4 deficiency results in a phenotype resembling human ataxias and dyskinesias.

2 Introduction

2.1 The synapse: a specialized neuronal compartment

Brain functions rely on the communication of neurons that transmit signals with high temporal and spatial precision. Synapses are specialized neuronal compartments that mediate this signal transduction. Although many synaptic connections are highly specialized, synapses can be classified as either electrical or chemical. Electrical synapses transduce fast signals via gap junction channels, which consist of hemichannels and form direct connections between adjacent cells. Whereas, chemical synapses are composed of a pre- and a postsynaptic neuronal terminal, separated by the synaptic cleft (20 - 40 nm). In contrast to the electrical synapse, information transmission at the chemical synapse depends on neurotransmitters that are released via synaptic vesicles from the presynaptic active zone (Figure 2.1, reviewed in Südhof, 2012).

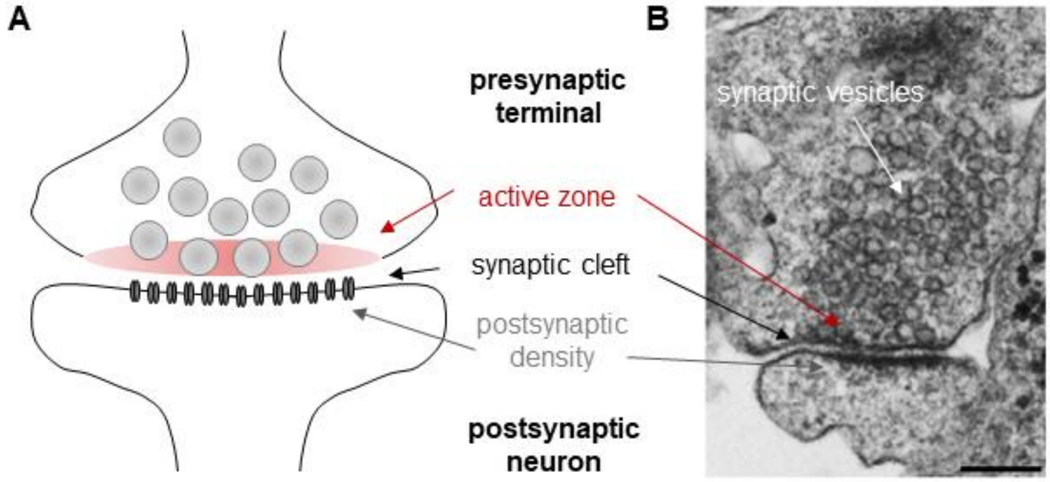

Figure 2.1: Synapse composition. (A) Principle structure of a chemical synapse. The presynaptic terminal comprises the release machinery together with neurotransmitter-filled synaptic vesicles (indicated in gray). Neurotransmitters are released at the active zone into the synaptic cleft and bind to receptors located at the postsynaptic density of the postsynaptic neuron. **(B)** Electron micrograph of a hippocampal synapse with the principle synaptic structures. Scale bar = 200 nm. Adapted from Kaeser et al., 2011; Südhof, 2012.

The presynaptic active zone consists of a dense protein network and has been shown to be crucial for neurotransmitter release (Couteaux and Pécot-Dechavassine, 1970). Ultrastructural studies have demonstrated that the active zone is precisely aligned with the postsynaptic density of the postsynaptic neuron (Dani et al., 2010; Tang et al., 2016). This dense protein network is referred to as the cytomatrix at the active zone (CAZ). The CAZ proteins are very insoluble and were therefore only identified using antibodies, genetic mutations or protein-protein interactions (reviewed in Südhof 2012). The key multidomain proteins of the CAZ are Rab3A-interacting molecule (RIM), RIM-binding protein (RIM-BP), Munc-13, α-Liprin and ELKS (protein rich in the amino acids E (glutamic acid), L (leucine), K (lysine), S (serine)). In addition, the large proteins Piccolo and Bassoon have been shown to be associated with active zones (Figure 2.2; tom Dieck et al. 1998).

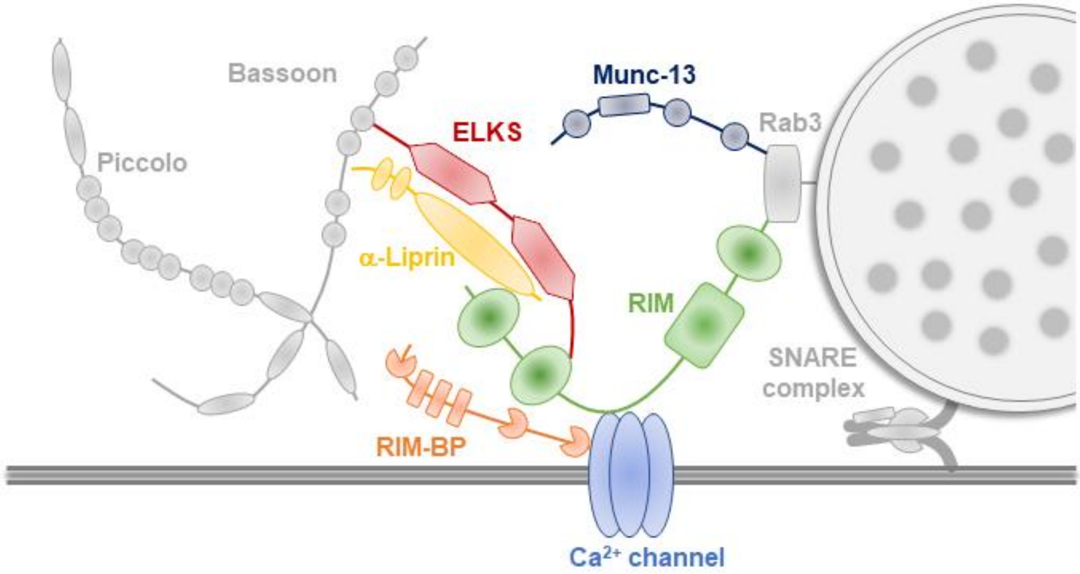

Figure 2.2: Structure of the cytomatrix at the active zone. Principle structure of the cytomatrix at the active zone. Different proteins have been shown to be associated to the CAZ and are directly or indirectly involved in the tethering of calcium channels to presynaptic vesicles. Thereby, ensuring correct neurotransmitter release. Adapted from Kaeser et al., 2011.

All CAZ proteins are composed of different sets of protein domains. This domain structure allows the interaction with each other but also with other synaptic proteins and the formation of a dense protein scaffold. The CAZ organizes the release and retrieval of synaptic vesicles and regulates changes in release during short-term and long-term forms of synaptic plasticity (reviewed in Schoch and Gundelfinger 2006). The synaptic vesicle exocytosis is triggered by the arrival of action potentials in the presynaptic terminal (Katz and Miledi, 1969).

At the postsynaptic terminal, the released neurotransmitters bind to ionotropic or metabotropic receptors in the postsynaptic density and elicit diverse postsynaptic responses. Briefly, ionotropic receptors undergo conformational changes upon neurotransmitter binding thereby opening the channel pore and allowing ion flux over the membrane. Whereas neurotransmitter binding of postsynaptic metabotropic receptors activates the production of intracellular second messengers such as cAMP or diacyglycerol, which are involved in intracellular cellular signaling cascades.

In summary, the synapse plays an important role in the communication between neurons. Accordingly, the correct function of the machinery in the synapse is crucial and a central protein involved in the synaptic vesicle exocytosis are the RIM proteins.

2.2 The RIM protein family

RIM proteins are one of the central scaffold proteins in the assembly of the CAZ due to multiple interactions with other presynaptic proteins. Specifically, RIM proteins have been shown to be responsible for neurotransmitter release. The RIM protein family consists of 7 different isoforms, generated from different promotor regions of in total 4 *Rims* genes. Only RIM1α and RIM2α contain the full set of protein domains: The N-terminal zinc finger domain, a PDZ domain and two C-terminal C2 domains, the C2A- and C2B-domain (Wang et al., 1997). In comparison to RIM1/2α, the RIM1β isoform possesses a shorter N-terminus and RIM2β lacks the zinc finger domain completely (Figure 2.3).

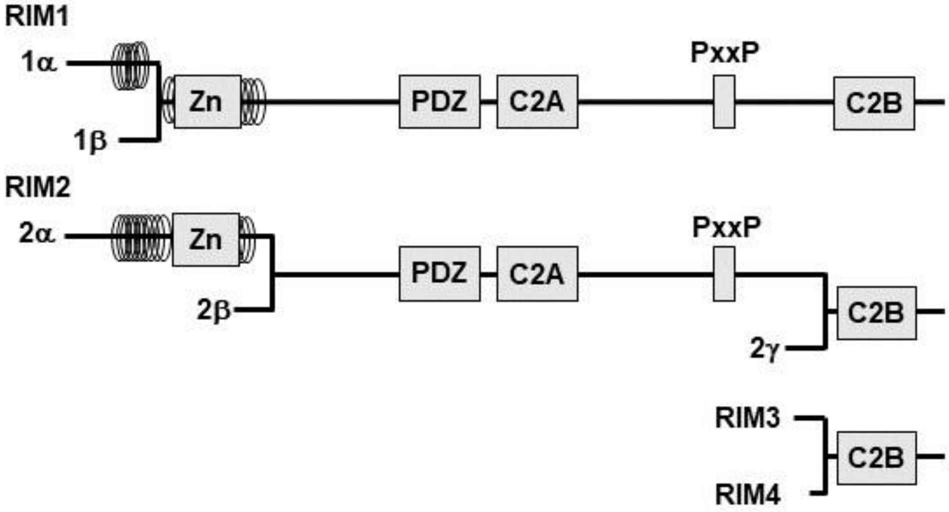

Figure 2.3: The multidomain RIM protein family. The RIM protein family consists of 7 different multidomain isoforms. The full set of domains is only present in RIM1/2α whereas all other isoforms are shorter and obtain only a subset of protein domains. Rab3-binding sequences are depicted as coils surrounding the N-terminal Zn^{2+}-finger domain. Adapted from Kaeser et al., 2011.

Due to their N-terminal zinc finger domain and the adjacent α-helix, α-RIMs are capable to bind to the C2A domain of Munc13-1 and to Rab3A which is located at synaptic vesicles. For example, in *C.elegans* as well as in cell culture experiments the interaction of RIM1α and Munc13-1 has been shown to be crucial for the regulation of the presynaptic readily releasable vesicle pool by tethering and priming synaptic vesicles to the active zone (Betz et al., 2001; Koushika et al., 2001). With the generation of RIM1α and RIM2α knock-out (KO) mice, insights into the vertebrate *in vivo* function of the large RIM isoforms were obtained. The KO of RIM1α leads to severe changes in synaptic transmission but did neither change the density and size of synapses, nor the synaptic ultrastructure, for example synaptic vesicle density or number of docked synaptic vesicles (Castillo et al., 2002; Schoch et al., 2002). In addition, the synaptic protein composition is almost unaltered in RIM1α KO mice. Only presynaptic Munc13-1 levels are reduced to 60%, probably due to its direct binding to RIM1α. Yeast two-hybrid screens and GST pull-down assays further identified Rab3A, Synaptotagmin 1 and α-Liprins as direct interaction partners of RIM1α, supporting the potential presynaptic scaffolding function of this RIM isoform (Schoch et al., 2002). Electrophysiological studies using hippocampal slices from RIM1α-mutant mice indicated a reduced neurotransmitter release probability in absence of RIM1α, due to a reduction in the readily releasable vesicle pool (Schoch et al., 2002).

Interestingly, the single KO of RIM2α does not lead to changes in neurotransmission and short-term synaptic plasticity, most probably due to the high homology to RIM1α which in turn can compensate for effects after RIM2α deletion (Schoch et al., 2006). However, deletion of both proteins (RIM1α/2α) in mice is lethal and synaptic transmission in E18.5 double knock-out (DKO) embryos is dramatically impaired.

Presynaptic neurotransmitter release is mainly mediated by N- and P/Q-type calcium channels, but also R-type calcium channels can contribute to the Ca^{2+} influx into the presynaptic terminal that ultimately leads to neurotransmitter release. In contrast, T- and L-type calcium channels are not involved in presynaptic transmitter release (Castillo et al., 1994; Dietrich et al., 2003). Synapses with mutant RIM proteins that lack the PDZ-domain show a reduction in calcium channel expression together with a shift in the Ca^{2+}-dependence of release. Moreover, RIM proteins bind via their proline-rich sequences to RIM-BP, a presynaptic protein that in turn binds to presynaptic calcium channels (Hibino et al., 2002; Kaeser et al., 2011; Südhof, 2012). Accordingly, RIMs can tether calcium channels to the presynaptic CAZ via a direct, PDZ-domain involving mechanism and an indirect mechanism via the connection to RIM-BP. Further studies showed that the large RIM isoforms are necessary to enrich calcium channels at the presynaptic CAZ and to tightly couple the calcium channels to readily releasable synaptic vesicles. Hence, ablation of large RIM isoforms results in a strongly reduced number of readily releasable vesicles as well as a slowing of the fast release component, pointing towards an additional vesicle-docking function of RIM1 and RIM2 (Han et al., 2011).

RIM proteins also comprise two C-terminal C2 domains. However, the function of the RIM C2A and C2B domains remain poorly understood. *In vitro* studies identified several interactors of these domains, for instance α-Liprin, Ca^{2+}-channel β-subunits and Synaptotagmins (Coppola et al., 2001; Kaeser et al., 2012; Schoch et al., 2002). Interestingly, the RIM C2B domain involves a lysine-rich polybasic stretch, a motif that binds to phosphatidylinositol 4,5-bisphosphate (PIP_2; Corbalan-Garcia and Gómez-Fernández, 2014; de Jong et al., 2018). A recent study identified the C2-domains of RIM as a binding partner of PIP_2 and showed that disruption of the C2B-PIP_2 connection lead to impaired synaptic transmission in RIM1/2 DKO neurons (de Jong et al., 2018).

Apart from the large isoforms, the RIM protein family contains 3 small isoforms, RIM2γ/3/4, which show a high structural homology among each other and consist only of the C2B domain and a short unique N-terminus (Figure 2.4; Wang and Südhof, 2003). The functional relevance of these small isoforms is largely unknown and needs further investigation to fully understand their physiological roles.

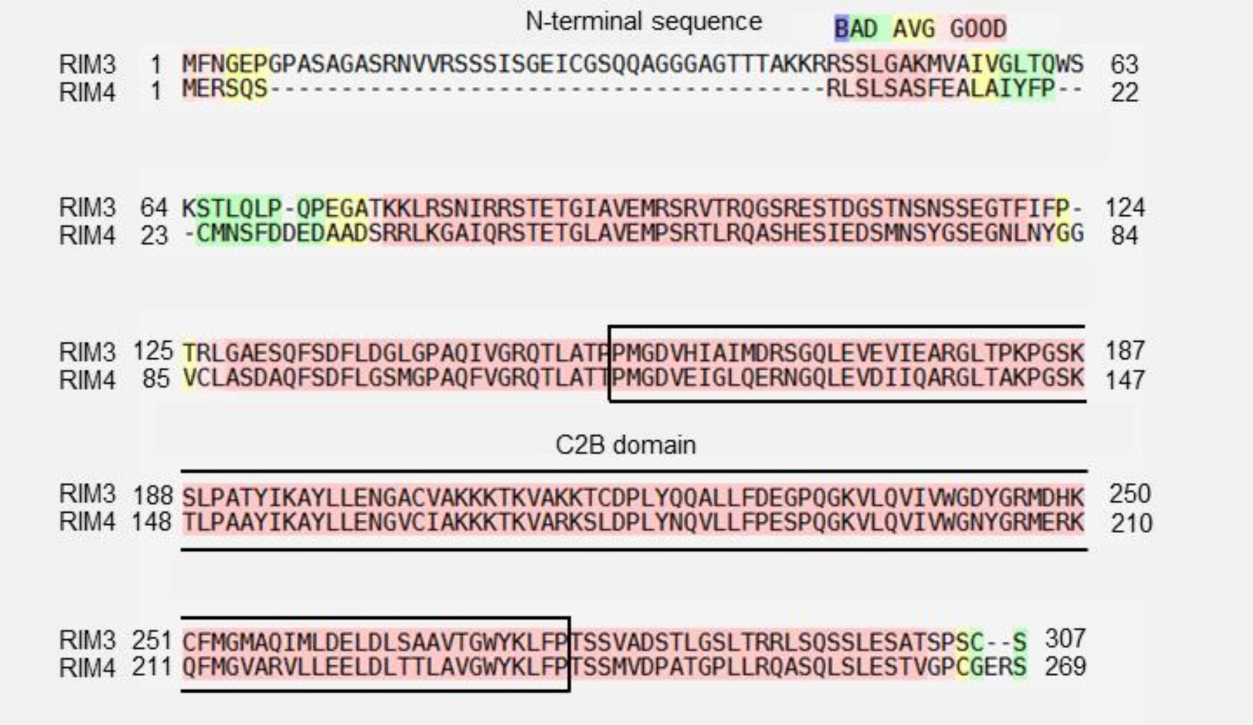

```
RIM3   1 MFNGEPGPASAGASRNVVRSSSISGEICGSQQAGGGAGTTTAKKRRSSLGAKMVAIVGLTQWS  63
RIM4   1 MERSQS---------------------------------------RLSLSASFEALAIYFP--  22

RIM3  64 KSTLQLP-QPEGATKKLRSNIRRSTETGIAVEMRSRVTRQGSRESTDGSTNSNSSEGTFIFP- 124
RIM4  23 -CMNSFDDEDAADSRRLKGAIQRSTETGLAVEMPSRTLRQASHESIEDSMNSYGSEGNLNYGG  84

RIM3 125 TRLGAESQFSDFLDGLGPAQIVGRQTLATPPMGDVHIAIMDRSGQLEVEVIEARGLTPKPGSK 187
RIM4  85 VCLASDAQFSDFLGSMGPAQFVGRQTLATTPMGDVEIGLQERNGQLEVDIIQARGLTAKPGSK 147

RIM3 188 SLPATYIKAYLLENGACVAKKKTKVAKKTCDPLYQQALLFDEGPQGKVLQVIVWGDYGRMDHK 250
RIM4 148 TLPAAYIKAYLLENGVCIAKKKTKVARKSLDPLYNQVLLFPESPQGKVLQVIVWGNYGRMERK 210

RIM3 251 CFMGMAQIMLDELDLSAAVTGWYKLFPTSSVADSTLGSLTRRLSQSSLESATSPSC--S 307
RIM4 211 QFMGVARVLLEELDLTTLAVGWYKLFPTSSMVDPATGPLLRQASQLSLESTVGPCGERS 269
```

Figure 2.4: RIM3 and RIM4 are highly homologous. High homology of RIM3 and RIM4 amino acid sequences (depicted in red), displayed by sequence alignment performed with the bioinformatics program Tcoffee (http://tcoffee.crg.cat/). Both isoforms contain a short, unique N-terminus. Amino acid sequence inside the box belongs to the homologous C2B domain.

2.2.1 Neuronal expression of RIM3 and RIM4

In contrast to RIM1 and RIM2, much less is known about the distribution and function of the small RIM isoforms RIM3 and RIM4 in neuronal cells and tissues. Both, RIM3 and RIM4 protein expression levels increase during development and reach a plateau value around postnatal day 20, similar to the large RIM isoforms (Alvarez-Baron et al., 2013; Kaeser et al., 2008). RIM3 and RIM4 are expressed in many brain regions that either are specific for one or express both isoforms. Within brain regions expressing both isoforms, the expression of RIM3 and RIM4 may also overlap or be specific for distinct layers or subregions. Specifically, *in situ* hybridization studies showed that RIM3 is expressed in the granule cell layer of the cerebellum, in the dentate gyrus of the hippocampus, in the external and plexiform layer of the olfactory bulb, cortical layer III as well as in the thalamus. Whereas, RIM4 expression is restricted to the granule cell and Purkinje cell layer of the cerebellum, the CA1 region in the hippocampus, the mitral cell layer and periglomerular cells in the olfactory bulb and all cortical layers (Alvarez-Baron et al., 2013; Liang et al., 2007).

In contrast to the subcellular distribution of the large RIM isoforms, RIM3 and RIM4 are not exclusively found at presynaptic active zones (Wang et al., 1997). In fact, it could be shown that RIM3 is mainly expressed in the soma and dendrites of neurons and is strongly enriched in the nucleus whereas RIM4 is uniformly distributed in axons and dendrites and present at pre- and postsynaptic compartments (Alvarez-Baron et al., 2013; Katrin Michel, Ph.D. Thesis). Other studies indicate that RIM3 is enriched at postsynaptic densities suggesting its importance on a functional level for postsynaptic information reception or processing (Liang et al., 2007). Furthermore, bioinformatic analysis of RIM3 and RIM4 amino acid sequences unveiled a nuclear localization signal in the N-terminus of RIM3 and a nuclear export signal in the C2B domain of RIM3 and RIM4. It could be shown that the nuclear localization signal in the RIM3 amino acid sequence is responsible for the localization of RIM3 to the nucleus (Katrin Michel, Ph.D. Thesis).

Taken together, the small RIM isoforms RIM3 and RIM4 are widely distributed in the brain. Although RIM3 and RIM4 are often expressed within the same brain regions, they exhibit different subregional expression patterns. This suggests that RIM3 and RIM4 may fulfill region-specific functions in the brain. Furthermore, the subcellular distribution of RIM3 and RIM4 within a single neuron is much different from the subcellular distribution of the large isoforms RIM1 and RIM2, pointing towards a different functional relevance of small RIM isoforms.

2.2.2 RIM3 and RIM4 interactions with other proteins

Protein interactions are the mechanism of choice underlying several biological processes inside cells, for instance signal transduction or transport. Large RIM isoforms have been shown to interact with multiple proteins at the presynaptic CAZ to ensure precisely timed neurotransmitter release. Especially, the C2B domains of RIM proteins have been shown to bind to α-Liprins, Synaptotagmin 1 and β-subunits of voltage-gated calcium channels (Coppola et al., 2001; Kaeser et al., 2011; Schoch et al., 2002; Wang and Südhof, 2003). However, less is known about potential interaction partners of the small RIM isoforms, RIM3 and RIM4. Due to the high homology of the C2B domain, studies suggested that also the small RIM proteins interact with Liprin-α and voltage-gated calcium channels (Uriu et al., 2010; Wang and Südhof, 2003).

Liprin-α is enriched at presynaptic CAZs and involved in the regulation of the presynaptic organization and the release of neurotransmitter in response to network activity via binding to large RIM isoforms as well as ELKS (reviewed in Torres and Inestrosa, 2018). GST-pulldown assays showed that GST-Liprin 3α captures the small RIM isoforms RIM2γ/3/4, suggesting that the C2B domain of these proteins is a Liprin-binding site (Wang and Südhof, 2003). Furthermore, immunoprecipitation of RIM3 and RIM4 together with Liprin-α showed similar results (Uriu et al., 2010). However, nuclear magnetic resonance (NMR)-analysis of the highly evolutionary conserved RIM1α C2B domain unveiled that the C2B domain alone is not able to interact with the suggested binding-region of Liprin-α. Accordingly, the C2B domain may require additional RIM1α sequences preceding the C2B domain to ensure correct binding (Guan et al., 2007). This finding was supported by a more recent study, identifying that RIM3 and RIM4 do not bind to Liprin-α via their C2B domain in contrast to RIM1 and RIM2. However, both RIM3 and RIM4 are able to bind to specific lipids in the cell membrane, namely phosphatidylinositol 4,5-bisphosphate (PIP_2) to a similar extend as RIM1 (de Jong et al., 2018).

Other studies identified a direct binding of the RIM1 C2B domain and the β4-subunit of presynaptic voltage-gated calcium channels, thereby modulating synaptic release via sustaining Ca^{2+} influx through inhibition of channel activation and anchoring synaptic vesicles in the vicinity of voltage-gated calcium channels (Kiyonaka et al., 2007). Interestingly, similar results were obtained for RIM3 and RIM4. GST-pulldown and co-immunoprecipitation experiments identified besides RIM1 and RIM2 also RIM3 and RIM4 as binding partners of voltage-gated calcium channel β-subunits. In addition, the relative amounts of pulled down β-subunits suggested that RIM3 has a higher binding affinity to neuronally expressed β_3- and β_{4b}-subunits, compared to RIM4. In general, binding affinities of RIM3 and RIM4 to β4-subunits are an order of magnitude lower compared to those of RIM1α and RIM2α, pointing towards a potential different function in presynaptic release (Kiyonaka et al., 2007; Uriu et al., 2010).

A proteomics approach with whole brain extracts as well as synaptosomal preparations was used to further identify potential binding partners of RIM3 and RIM4. Most of the identified binding partners in whole brain homogenates could be related to functional categories such as ‘growth and neuronal development’, ‘adhesion molecules’ and ‘proteins involved in intracellular traffic’, whereas only a low number of synaptic proteins could be detected. In contrast, synaptosomal preparations unveiled a large group of ‘synaptic proteins’ as potential interaction partners of RIM3 and RIM4, followed by ‘cytoskeletal proteins’ and ‘proteins involved in intracellular traffic’ (Katrin Michel, Ph.D. Thesis), indicating a broad range of potential functions of RIM3 and RIM4.

In addition to the interaction with other cellular proteins, the C2B domain of RIM proteins has been shown to form dimers with weak affinity with itself. The dimer formation may be strengthened by sequences N-terminal to the C2B domain or by other protein-interactions that participate in organizing the active zone and thus may increase the local RIM concentration (Guan et al., 2007). In contrast, a more recent study showed by analytical ultracentrifugation that the homodimer affinity for C2B domains of RIM proteins is very weak, thus making it very unlikely to be physiological relevant (de Jong et al., 2018).

In conclusion, RIM3 and RIM4 have different interaction partners to which they mainly bind via their evolutionary conserved C2B domain. These findings imply that both proteins may play important roles in cellular functions apart from presynaptic neurotransmitter release as it was shown for the large RIM isoforms.

2.2.3 Neuronal functions of RIM3 and RIM4

To date, only a few studies investigated potential functions of RIM3 and RIM4 in neurons. As already mentioned above, the broad subcellular distribution of these small RIM isoforms as well as the plethora of potential interactions partners suggests that RIM3 and RIM4 fulfill different functions in neurons compared to the large isoforms RIM1 and. In addition, the variation of interaction partners, ranging from synaptic to other cellular proteins, further point towards a broad functional spectrum.

An important function of the large RIM isoforms is the previously reported tethering of presynaptic voltage-gated calcium channels, mainly P/Q- and N-type channels to active zones (Kaeser et al., 2011). Interestingly, RIM3 and RIM4 have been found to directly bind to voltage-gated calcium channel β-subunits, thereby modulating presynaptic Ca^{2+}-influx and exocytosis. Furthermore, it has been suggested that in contrast to RIM1 and RIM2, the small RIM isoforms suppress anchoring of neurotransmitter-containing vesicles to voltage-gated calcium channels (Uriu et al., 2010). Additionally, it was reported that the C2B domain of RIM3 binds to the C-terminus of the $Ca_v1.3$ α-subunit found in inner hair cells of the cochlea, supporting a potential interaction of small RIM isoforms with presynaptic voltage-gated calcium channels (Picher et al., 2017).

Apart from their potential modulation of presynaptic voltage-gated calcium channels, *in vitro* and *in vivo* studies unveiled that RIM3 and RIM4 are important proteins involved in dendritic and axonal outgrowth and arborization during development. Knock-down of RIM3 or RIM4 in rat primary hippocampal neurons reduced the dendritic complexity of neurons as well as the number of dendritic spines. Moreover, the loss of synaptic contacts after knock-down of RIM3 or RIM4 *in vitro* was demonstrated by reduced miniature excitatory postsynaptic current (mEPSC) frequencies whereas the mEPSC amplitudes following RIM4 knock-down were unchanged. Since the cellular Golgi apparatus is necessary for membrane transport and dendritic and axonal outgrowth, further studies showed that the knock-down of RIM3 and RIM4 resulted in an abnormal Golgi structure, suggesting a potential role of both proteins in Golgi trafficking, leading to the previously described cellular phenotype (Alvarez-Baron et al., 2013, Katrin Michel, Ph.D. Thesis).

In summary, the small RIM isoforms, RIM3 and RIM4, seem to be involved in divergent neuronal functions, such as the involvement in presynaptic Ca^{2+}-dependent exocytosis as well as dendritic and axonal outgrowth and arborization. However, the underlying mechanisms how RIM3 and RIM4 are involved on a molecular level needs further investigation.

2.2.4 Association of RIM3 and RIM4 with neuronal disorders

In recent years, alterations in synaptic transmission and dysfunction of neuronal networks have been linked to mutations of synaptic proteins and therefore referred to as synaptopathies. The large RIM isoforms as central CAZ components play a key role in presynaptic neurotransmitter release. Interestingly, the knock-out of RIM1α in mice has been shown to be related to schizophrenia-like behaviors (Blundell et al., 2010; Powell et al., 2004). Furthermore, the *Rims1* gene was identified as a candidate gene for schizophrenia, autism and intellectual disability in genome-wide association studies (GWAS; Fromer et al., 2014; Iossifov et al., 2012; Khan et al., 2016; Pers et al., 2016).

Oligonucleotide-microarrays identified an increase in *Rims3* gene expression in the amygdala of schizophrenia patients. The amygdala is part of the limbic system in the brain involved in emotion processing and its malfunctioning is a major symptom of schizophrenia (Weidenhofer et al., 2006). In addition, RIM3 was associated with autism spectrum disorder in children. The *Rims3* gene was found in a genome-wide expression profiling study and in a patient with microdeletions in the C2B domain (Kumar et al., 2010; Nishimura et al., 2007). Single amino-acid mutations in the RIM3 protein associated with autism were shown to alter the interaction with β-subunits of voltage-gated calcium channels and impair functional properties of P/Q- and N-type calcium channels. This in turn lead to the hypothesis that altered presynaptic voltage-gated calcium channels are involved in autism phenotypes (Takada et al., 2015). In addition, also RIM4 was associated with autism in an epidemiological study in an isolated population in the Faroe Islands. Individuals with autism without intellectual disability carried *de novo* deleterious variants of the *Rims4* gene (Leblond et al., 2019).

Parkinson’s disease is characterized by α-synuclein accumulations in the brain and symptoms like movement abnormalities, but also dementia and depression. In a study, investigating α-synuclein accumulation in the hippocampus, RIM3 expression was reduced in conjunction with an altered ultrastructural architecture of hippocampal synapses (Kohl et al., 2016). Another study showed that increased neuronal activity in the brain, for example during epileptic seizures leads to upregulation of RIM4 (Hermey et al., 2013). In conclusion, RIM proteins in general are associated with a variety of neurological disorders, that often involve a synaptic dysfunction. Several studies have linked the small RIM isoforms with potential functions in schizophrenia, autism, Parkinson’s disease and epilepsy.

2.3 Constitutive RIM3 and RIM4 knock-out mice

First insights of RIM3 and RIM4 functional relevance in neurons were obtained mainly by *in vitro* studies. However, to further understand mechanistically in which and how RIM3 and RIM4 might be involved in neuronal processes, *in vivo* knock-out studies were needed. They provide the benefit of studying specific cellular mechanisms in distinct parts of the brain but also the influence on the whole organism.

2.3.1 Generation of constitutive RIM3 and RIM4 knock-out mice

For the investigation of potential functions of the small RIM isoforms RIM3 and RIM4 in a more physiological environment, constitutive knock-out mice were generated. The insertion of a splice acceptor lacZ gene trap cassette disrupted the endogenous RIM3 or RIM4 transcripts and lead to constitutive 'knock out first' (KO 1^{st}) RIM3 or RIM4 mice (Figure 4.1). Real-time PCR and immunoblot analysis revealed that the gene and protein levels were decreased in cortex, hippocampus and cerebellum of constitutive RIM3 or RIM4 KO mice (Katrin Michel, Ph.D. Thesis). Furthermore, pups of heterozygous RIM3 and RIM4 breedings were viable and undistinguishable upon their genotype. Both constitutive KO 1^{st} mouse lines were born at mendelian ratios with 25% wildtype, 50% heterozygous and 25% KO litters (Katrin Michel, Ph.D. Thesis).

2.3.2 RIM4 knock-out mice develop episodically occurring motor impairments

Constitutive RIM3 KO 1^{st} mice as well as constitutive RIM4 KO 1^{st} mice develop normally during the first 3 weeks after birth. However, around postnatal day 20 constitutive RIM4 KO 1^{st} mice stop to gain weight at the same rate as their WT and heterozygous littermates (Katrin Michel, Ph.D. Thesis). At the same time, the KO mice develop episodically occurring motor impairments. This phenotype is characterized by strong hind limb impairments, sometimes even the forelimbs are affected. In between periods of extensive movement, phases of complete immobility appear in which the hind limbs are stretched out and rigid. Video monitoring of the KO mice unveiled that these motor impairments occur approximately once per day and last up to 4 hours. During the time without episodic motor impairments, the mice showed no abnormal behavior (Katrin Michel, Ph.D. Thesis).

In a first set of motor behavior experiments it was demonstrated that constitutive RIM4 KO 1^{st} mice are weaker and show impaired balance and fine motor coordination. Interestingly, it was possible to induce the episodically occurring motor impairments by single injections of ethanol or caffeine in the constitutive KO 1st mice (Katrin Michel, unpublished data). This induction was also shown for other mouse models with similar motor-related phenotypes (Tara et al., 2018). An important brain region for motor coordination is the cerebellum. Therefore, RIM4 may be of particular importance in the cerebellum and a dysfunction may cause the motor impairments observed in the constitutive RIM4 KO 1st mice.

2.4 The cerebellum: a key brain region for motor coordination

Several years before the neuronal architecture of the cerebellum was described by Camillo Golgi and Ramon y Cajal, a number of lesion studies, mainly performed by Luigi Ronaldo and Marie-Jean-Pierre Fluorens, identified the cerebellum as being important for normal movement and motor coordination (reviewed in Ito, 2002). Even though a lot has been learned about the information processing in cerebellar circuits, further investigations are needed to fully reveal the cerebellar contributions to motor coordination and learning.

The cerebellum is divided into clear anatomical substructures, which in concert form neuroanatomical circuits with only a small number of neuronal subtypes. The surface of the cerebellum is folded ('folia'), and the inner part consists of white matter in which several deep nuclei are found. The cerebellum is divided by transverse fissures which separate the anterior from the posterior lobes and the body of the cerebellum from the smaller flocculonodular lobes. All lobes expand over the complete cerebellum from the midline to the lateral end (Basson and Wingate, 2013; Kandel 5th edition). In the anterior-posterior direction, two furrows separate the cerebellum into three parts: two outer cerebellar hemispheres and the inner cerebellar vermis (Figure 2.5 A). Parasagittally, the cerebellar vermis can be divided in 10 different lobules, corresponding to the folia in which a uniform layering of cell types can be found (Figure 2.5 B; Larsell, 1937).

As explained in detail below, the cerebellum is segmented in 3 compartments: The vestibulocerebellum, the spinocerebellum and the cerebrocerebellum. The vestibulocerebellum includes the flocculonodular lobes and is the most primitive part of the cerebellum. It receives input from vestibular and visual projections which then further project to the vestibular nuclei in the brain stem. The vestibulocerebellum is therefore involved in balance, vestibular reflexes and eye movements (Voogd et al., 1996; Kandel et al., 2013). The spinocerebellum instead, consists of the median and paramedian zone of the cerebellar hemispheres as well as the vermis. Furthermore, it is the only part receiving input from the spinal cord and being involved in movement of distal and proximal muscles together with eye movements from vestibular inputs. In contrast, the cerebrocerebellum contains the lateral cerebellar hemispheres and mainly receives input from several areas of the cerebral cortex. This compartment is associated with highly skilled movements including speech (Kandel et al., 2013; Purves et al., 2001).

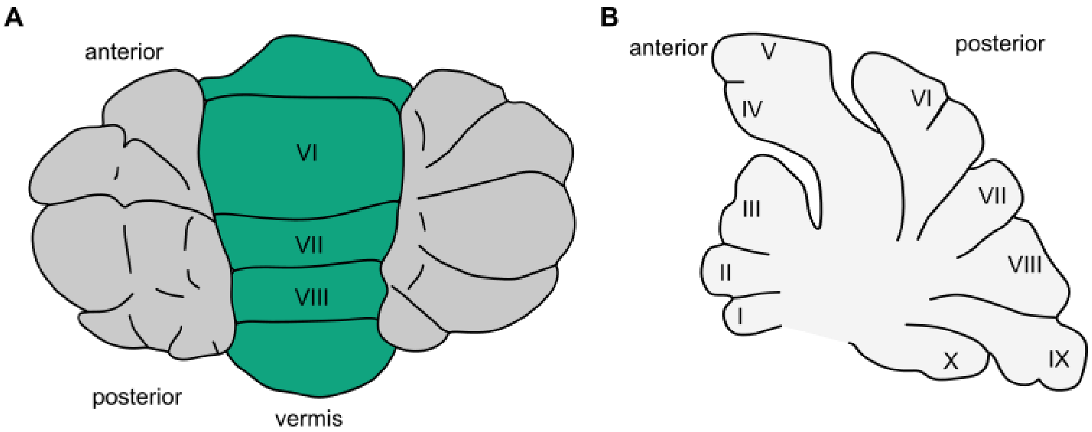

Figure 2.5: The organization of the cerebellar cortex. A: Dorsal view of the cerebellum, which is divided transversely by fissures and by two orthogonal running furrows. These furrows separate the outer cerebellar hemispheres (gray) from the inner cerebellar vermis (green). **B:** Parasagittal view of the cerebellar vermis region. Corresponding to the folia, the vermis is subdivided into lobules I to X. Modified from Basson and Wintage, 2013.

The cerebellum exhibits a very modular organization (Figure 2.6). The regular morphology and the compartmentalization result in a high cellular connectivity and thus allows fast information processing (Ito, 2006). In the gray matter of the cerebellum, the neurons are located in three layers: The outer molecular layer, the Purkinje cell layer and the inner granule cell layer. The most abundant neuronal cell type in the cerebellum are granule cells, which send their unmyelinated axons to the superficial molecular layer where they form parallel fibers. These glutamatergic fibers run in parallel to the long axis of a folium and make contacts with dendrites of several Purkinje cells (Saab and Willis, 2003). In addition, GABAergic stellate and basket cells are also located in the molecular layer, forming inhibitory contacts to Purkinje cells. Another type of interneuron located in the molecular layer, the Golgi cells, send inhibitory projections to granule cells. In addition, excitatory unipolar brush cells also regulate the activity of granule cells in some cerebellar lobules (Mugnaini et al., 2011). An additional, more recently discovered cell type are Lugaro cells which form connections with basket and Golgi cells and receive input from serotonergic afferent fibers and recurrent Purkinje cell collaterals. Interestingly, Lugaro cell firing induces rhythmic activity in local neural circuits (Dieudonné and Dumoulin, 2000; Kalinichenko and Pushchin, 2018). Input from other brain regions reaches the cerebellar circuits via mossy fibers or climbing fibers. The mossy fiber pathway excites Purkinje cells indirectly via granule cells and their parallel fibers, resulting in Purkinje cell simple spiking. In contrast, climbing fibers originate always from the contralateral inferior olive in the brain stem and directly form synapses with the proximal dendrites of Purkinje cells. Theses synapses have been shown to be involved in the generation of so called complex spikes (De Zeeuw et al., 1998; Saab and Willis, 2003). Notably, climbing fibers make contact with one Purkinje cell only, but can form up to 26.000 synapses on a single cell (Ito, 2001).

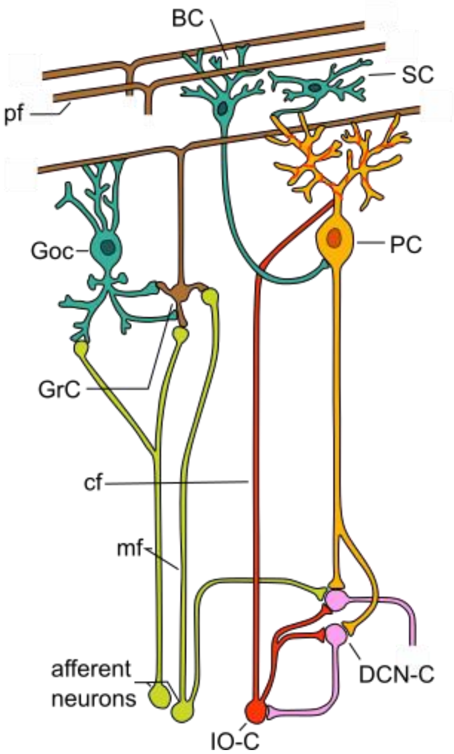

Figure 2.6: Cerebellar circuits. The cerebellar cortex includes several cell types such as granule cells (GrC), Golgi cells (Goc), Purkinje cells (PC) as well as stellate and basket cells (SC, BC). All these cell types are interconnected and form a cerebellar circuit. Inputs are derived from mossy fibers (mf), originating from brain stem or spinal cord nuclei, parallel fibers (pf) coming from granule cells or climbing fibers (cf), which originate from the inferior olive (IO-C). Cerebellar output is transmitted via the deep cerebellar nuclei (DCN-C), which at the same time inhibit the IO-C. Adapted from D'Angelo and Casali, 2012.

Several studies documented that the cerebellum sends projections to cortical and subcortical brain regions. The potentially most investigated cerebello-cerebro connections are the motor and somatosensory loops. Here, the ventrolateral thalamic nuclei project to the cortical layer IV and V in the primary motor area (M1), whereas the primary somatosensory area (S1) is innervated by projections from the intragranular and superficial cortical layers which receive their afferents from the intralaminar nuclei of the thalamus (Molinari et al., 2002). Apart from the motor and somatosensory loops, the cerebellum is closely interconnected with the parietal lobe and the prefrontal lobe via the ventrolateral thalamic nuclei (Kusunoki et al., 2000).

In conclusion, the cerebellum contributes to the generation and control of motor movements via interactions with a variety of brain regions. Additionally, not only motor processes are controlled by the cerebellum, but it is also involved in cognition and reward-related learning. Accordingly, malfunctions, for example via the loss of synaptic proteins, in the highly interconnected and complex cerebellar circuitry can have dramatic impact on motor coordination and has been suggested to be involved in human diseases, such as ataxias.

2.5 Mouse models of cerebellar ataxia

Cerebellar ataxias in humans are described as the poor coordination of movements, balance and gait and as a result of a dysfunction of the cerebellum. Ataxias are rare diseases with a varying prevalence between 1-40:100.000 (Becker, 2014).

In recent years, many different mouse models characterized by phenotypic signs of cerebellar ataxia were described. A plethora of genetic mutations, alterations in ion channel assembly and changes in neuronal signaling circuits have been indicated as the mechanism underlying the observed ataxia-related phenotypes. As explained herein above, Purkinje cells are the sole output of cerebellar circuits and are important for motor coordination and execution. Plenty of evidence arose from several studies that ion channel mutations altering the intrinsic firing properties of cerebellar Purkinje cells are involved in the generation of ataxia (reviewed in Hoxha et al., 2018).

Voltage-gated calcium channels are responsible for Ca^{2+} entry upon membrane depolarization. The P/Q-type voltage-gated calcium channel or $Ca_v2.1$ is highly expressed in cerebellar Purkinje cells (Craig et al., 1998; Westenbroek et al., 1995) and mutations in the α-subunit of these channels are associated with episodic ataxia type-2 (EA2), hemiplegic migraine-1 and spinocerebellar ataxia type 6 (SCA6) in humans (Jen et al., 2007; Ophoff et al., 1996; Rajakulendran et al., 2012). In mice, spontaneous mutations of the corresponding *Cacna1a* gene lead to ataxic phenotypes: *tottering* (Fletcher et al., 1996), *leaner* (Tsuji and Meier, 1971), *rolling* (Oda, 1973), *rocker* (Zwingman et al., 2001) and *wobbly* mice (Xie et al., 2007). These mice show functional alterations of Purkinje cells, for instance reduced firing frequency or precision in pacemaking activity but also morphological defects such as Purkinje cell loss and dendritic atrophy (Burgess and Noebels, 1999; Fletcher et al., 1996; Hoxha et al., 2018; Mori et al., 2000; Walter et al., 2006). Mutations targeting the β_4-subunit of voltage-gated calcium channels affect the function of Purkinje cells as well as their dendritic morphology, leading to ataxia and focal motor seizures, very similar to the *tottering* phenotype (*lethargic* mice; Benedetti et al., 2016; Burgess et al., 1997). Additionally, a mutation of the voltage-gated calcium channel $\alpha2\delta2$-subunit reduced Ca^{2+} currents in cerebellar Purkinje cells leading to an ataxic, wide-based gait as well as paroxysmal dyskinesia in mice (*ducky* mice; Barclay et al., 2001; Snell, 1955).

Voltage-gated potassium (K_v) channels are involved in the control of the membrane potentials and thus neuronal excitability. Mutations in the K_v4.3-underlying *Kcnd3* gene are associated with spinocerebellar ataxia type 19 and 22 (SCA19/22) which displays a heterogeneity of symptoms in patients. Interestingly, a study investigating the function of K_v4.3 mutations identified the mutated protein having a dominant negative effect on trafficking and surface expression of normal K_v4.3 channels. This points to the fact that K_v4.3 miss localization or functioning may lead to Purkinje cell loss, neurodegeneration and ataxia (Duarri et al., 2015). In addition, the large conductance voltage- and Ca^{2+}-activated K^+ (BK) channel knock-out mice ($BK^{-/-}$ mice) develop motor impairments in particular, tremor, abnormal gait and motor learning. Purkinje cells of $BK^{-/-}$ mice show changes in electrophysiological properties (Sausbier et al., 2004) and Purkinje cell-specific ablation of BK channels resulted in a similar ataxic phenotype (Chen et al., 2010).

Metabotropic glutamate receptor 1 (mGluR1) knock-out mice show an ataxic gait, impaired climbing fiber elimination and deficient long-term depression (LTD; Aiba et al., 1994; Kano et al., 1997). A decreased expression of mGluR1 by deletion of the transcription factor retinoid-related orphan receptor α (RORα) results in gait abnormalities and reduced motor coordination in mice (*staggerer* mice; Jarvis et al., 2002; Sidman et al., 1962). Apart from loss of mGluR1 function, several studies report involvement of mGluR1 gain of function mutations in spinocerebellar ataxia type 2 (SCA2).

A first link between RIM proteins and disorders involving deficits in motor coordination has been shown for the paroxysmal nonkinesigenic dyskinesia (PNKD) protein. *PNKD*$^{-/-}$ mice obtain nigrostriatal defects in neurotransmission with reduced dopamine levels in the striatum (Lee et al., 2012). Furthermore, the locus of PNKD mutations has been mapped and the gene, myofibrillogenesis regulator 1 (*MR-1*) has been identified in several patients. The mouse homolog of *MR-1*, *BRP17* has been shown to be widely expressed in the brain. Among other regions, *BRP17* is expressed in granule and Purkinje cells of the cerebellum (Lee et al., 2004). Interestingly, RIM1 and RIM2 have been identified as interaction partners of the PNKD protein. Furthermore, PNKD has been suggested to antagonize the action of RIM in modulation of synaptic transmitter release (Shen et al., 2015).

In summary, the number of different potential alterations indicates that several factors are needed to keep the variability of Purkinje cell firing within a narrow range to produce the correct output signal leading to precise movement and motor coordination. The occurrence of the episodic motor impairments in constitutive RIM4 KO1st mice led to the conclusion that the deletion of RIM4 could play a role in the generation of ataxia-like symptoms in mice.

3 Aims of the study

Recent studies suggested a potential role of RIM3 and RIM4 in neuronal outgrowth and arborization by regulating intracellular vesicular trafficking processes. Furthermore, a proteomics approach identified several interaction partners of RIM3 and RIM4, such as cytoskeleton or nuclear proteins, suggesting a broad range of potential cellular functions of small RIM isoforms. The generation of constitutive RIM3 and RIM4 KO mice supported the hypothesis that both proteins in turn might have different cellular functions. Constitutive RIM3 KO develop normally, whereas constitutive RIM4 KO mice develop episodically occurring motor impairments. To further elucidate the functional relevance of RIM4 and to a minor extend RIM3 in neuronal circuits the following aims will be addressed.

As a first goal of this study, we aim to identify neuronal genes and proteins that are potentially regulated by RIM4. Therefore, we will define brain regions with high RIM4 expression using mice expressing lacZ under the endogenous RIM4 promotor. I turn, tissue of these brain regions from previously generated constitutive RIM4 KO 1st and RIM4 constKO mouse lines is used for transcriptomic and proteomic analyses. Since the large RIM isoforms are mainly involved in synapse-related functions for instance synaptic plasticity, we will additionally analyze if RIM4 expression is regulated in an activity-dependent manner which would point towards a potentially synaptic function of RIM4.

As a second aim we will further characterize the episodically occurring motor impairments by the generation of Purkinje cell-specific RIM4 KO mice. We will answer the question if this cell type-specific RIM4 deletion is sufficient to induce similar episodic motor impairments in mice. Furthermore, we will use the newly generated mouse line to specifically identify the *in vivo* impact of RIM4 in information processing of cerebellar Purkinje cells which are the main cell type involved in cerebellar motor coordination and movement.

Independent of RIM4 function, we will investigate if the presynaptic protein ELKS is an interaction partner of SRPK2, a recently identified presynaptic protein kinase. Using a super-resolution microscopy approach, we will further examine if SRPK2 modulates the synaptic ultrastructure by the interaction with ELKS.

Taken together, this study will mainly provide new insights into the functional role of RIM4 on a cellular level in a physiological environment to further understand how this protein is involved in the generation of cerebellar motor coordination and movement. To a smaller extend this study will additionally focus on three other proteins, RIM3 as well as ELKS and SRPK2, to give further insights into their functional relevance in the brain and, more specifically, at synapses.

4 Materials and Methods

Chemicals were obtained from Sigma-Aldrich (Taufkirchen, Germany) and Carl Roth GmbH (Karlsruhe, Germany) unless otherwise indicated. Materials are mentioned in the text where necessary. Antibodies and primers used in the experiments are listed in chapter 10.1 (List of Antibodies and Primers). Statistical data analysis was performed with GraphPad Prism version 8.4.1.

4.1 Mouse husbandry

All animal experiments were performed in accordance with the guidelines of the Bonn University Medical School Animal Care Committee. Mice were housed with a maximum of 5 animals per cage in an animal facility with an alternating 12-hour dark/light cycle at 22 ± 2 °C and 55 ± 10% humidity. Water and food were provided ad libitum.

4.2 Generation of RIM3 and RIM4 mouse models

Null mice for RIM3 and RIM4 were generated as described previously in Katrin Michel, Ph.D. Thesis. Briefly, the international Knock-out Mouse Project consortium (KOMP) generated embryonal stem cells carrying the knock-out construct which was designed to create three different mouse lines for both, RIM3 and RIM4. The first line after germline transmission constituted a ‘knock-out first’ allele. Here, the insertion of a splice acceptor lacZ gene cassette disrupted the endogenous RIM3 or RIM4 transcript respectively resulting in a constitutive knock-out (constitutive KO 1st; Figure 4.1). After confirmation of successful gene targeting, mice were crossed against flippase (Flp) recombinase-transgenic mice, leading to the removal of the lacZ and the neomycin cassette (Dymecki, 1996) to generate RIM3^{floxed} or RIM4^{floxed} mice (RIM3$^{fl/fl}$; RIM4$^{fl/fl}$).

In the next step, these mice were mated with transgenic mice that express Cre recombinase ubiquitously (B6.C-Tg(Pgk1-cre)1Lni/CrsJ; (Lallemand et al., 1998) to create constitutive RIM3 and RIM4 KO mice (RIM3const KO, RIM4const KO). In addition, homozygous male RIM4$^{fl/fl}$ mice were mated with female Pcp2-Cre$_{tg}$ mice (stock number 004146; B6.129-Tg(Pcp2-cre)2Mpin/J; Barski et al., 2000) purchased from The Jackson Laboratory in order to generate cerebellar Purkinje cell-specific RIM4 KO mice (Pcp2$_{M}$-Cre$_{tg}$:RIM4$^{fl/fl}$; further breeding details are explained in chapter 10.1). For verification of Purkinje cell-specific Cre recombinase expression in Pcp2$_{Mpin}$-

Cre$_{tg}$:RIM4$^{fl/fl}$ mice, homo- and heterozygous Pcp2$_{M}$-Cre$_{tg}$:RIM4 were bred with tdTomato-reporter mice (B6.Cg-Gt(ROSA)26Sor$^{tm9(CAG-tdTomato)Hze}$/J) from ongoing breedings in the lab, generating Pcp2$_{M}$-Cre$_{tg}$:tdTom:RIM4$^{fl/+}$ or Pcp2$_{M}$-Cre$_{tg}$:tdTom:RIM4$^{+/+}$ mice. Primers and protocols used for genotyping of RIM3 and RIM4 KO mouse lines are listed in the Appendix Table 6.

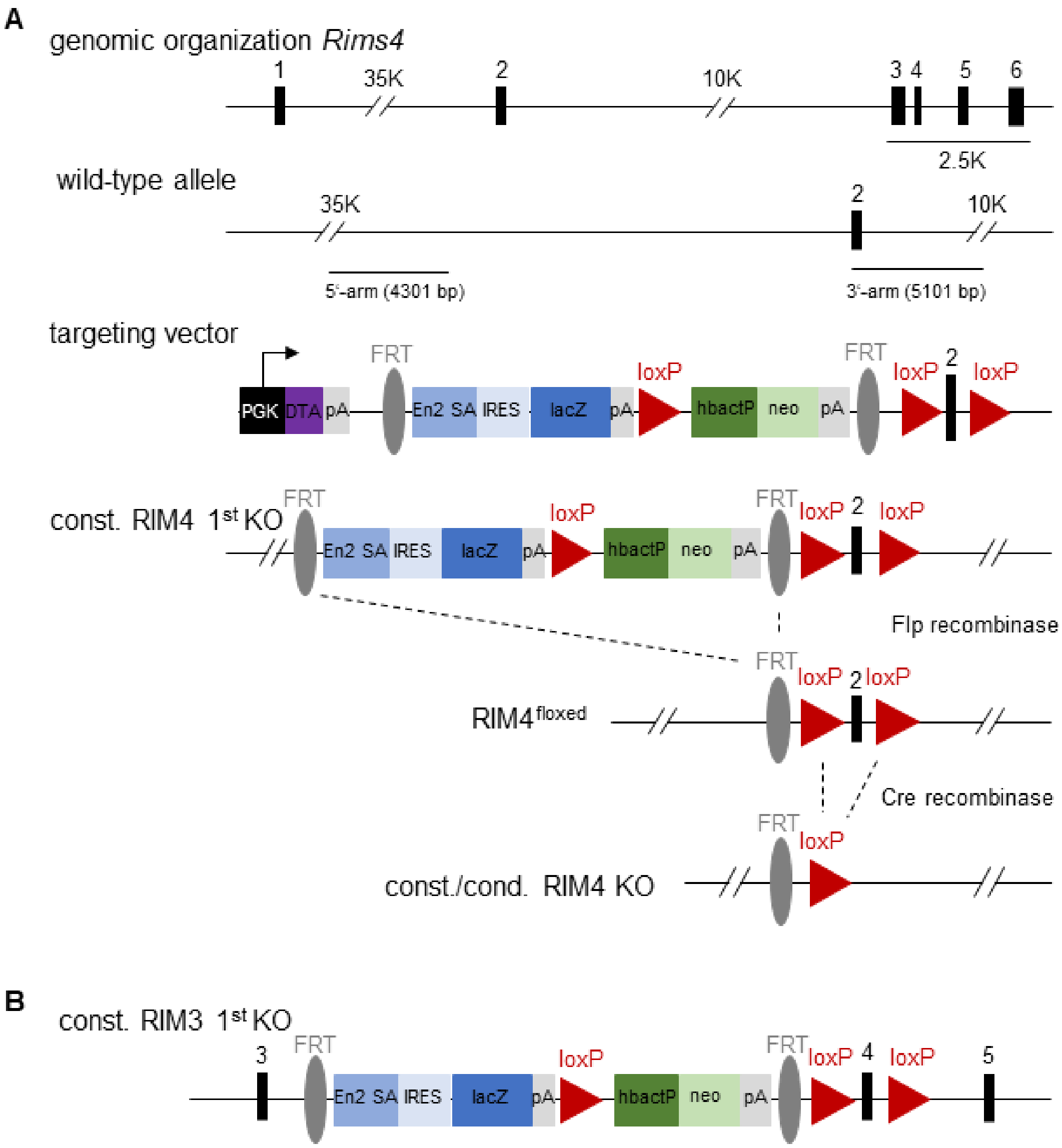

Figure 4.1: Generation of constitutive and conditional RIM3 and RIM4 knock-out mice. (A) Insertion of a LacZ splice acceptor cassette in between exon 1 and 2 introduces splicing of RIM4 after exon 1 and causes disruption of normal protein expression (constitutive RIM4 KO 1st). FLP-mediated recombination leads to the excision of the splice acceptor cassette and reconstitutes normal RIM4 protein expression (RIM4^{floxed}). Cre recombinase-mediated recombination results in the excision of exon 2 and thereby abolishes RIM4 protein expression (constitutive / conditional RIM4 KO). **(B)** Introduction of the gene trap cassette between exon 3 and 4 of the Rims3 gene leads to splicing of RIM3 after exon 3 and disrupts protein expression (constitutive RIM3 KO 1st). Similar to the knock-out strategy for RIM4 shown in (A), RIM3^{floxed} and constitutive/conditional RIM3 KO mice can be generated from constitutive RIM3 KO 1st mice (Adapted from Katrin Michel, Ph.D. Thesis).

4.3 Molecular biological methods

4.3.1 Polymerase chain reaction

Polymerase chain reaction (PCR) was used to amplify DNA fragments. The standard PCR-mastermix contained the double-stranded DNA of interest, single-stranded primer pairs and the EconoTaq PLUS GREEN 2x polymerase mix (Lucigen, WI, USA) in the following concentrations:

Table 1: Components for the PCR mastermix to amplify DNA fragments of interest.

Component	**Concentration**
EconoTaq PLUS GREEN 2x Master Mix	1x
5’ primer	1 µM
3’ primer	1 µM
Template DNA	100 ng/µl

The mastermix was completed with water to a final volume of 10 µl per reaction and the amplification reactions were performed in a thermocycler (Bio-Rad, CA, USA). In an initial step the DNA was denaturated at 95°C for 5 minutes, followed by 35 cycles with 30 sec denaturation at 95°C, a 40 sec annealing step at 50-59°C and an extension step at 72°C for 1 min per kilo base pair. The final extension was performed at 72°C for 10 min. Amplified PCR products were separated by size on agarose gels (1-2%) and band sizes were analyzed with the ChemiDoc imaging system (Bio-Rad, CA, USA).

4.3.2 mRNA isolation and cDNA synthesis

Total mRNA of primary cortical neurons of C57Bl/6N mice, cultured in 24-well plates, was isolated with the RNeasy Midi kit (Qiagen, Germany) according to the manufacturers protocol for ‘Isolation of total mRNA from Animal Cells’. For mRNA isolation from tissue, the RNeasy Midi kit was used according to the manufacturer protocol for ‘Isolation of total mRNA from Animal Tissues’. Constitutive RIM3 1st KO and RIM4 1st KO as well as WT control mice, 15-20 weeks old, were anesthetized with isoflurane and decapitated. For RIM3 1st KO mice, cortical and thalamic tissue was separated from the rest of the brain and directly frozen in liquid nitrogen. mRNA isolation of constitutive RIM4 1st KO mice was performed with cortical and cerebellar tissue, also directly frozen in liquid nitrogen. mRNA samples were stored at -80°C.

For cDNA synthesis of previously isolated mRNA from cell cultures or tissues the RevertAid H Minus First Strand cDNA Synthesis kit (Thermo Fisher Scientific, MA, USA) was used according to the manufacturers protocol. cDNA samples were diluted 1:10 with RNase-free water and stored at -20°C.

4.3.3 Quantitative real-time PCR

Quantitative real-time PCR (qRT-PCR) was performed in triplicates of each sample on a CFX384 Touch Real-Time PCR Detection System (Bio-Rad, CA, USA) using the following mastermix concentrations:

Table 2: Mastermix components for qRT-PCR.

Component	**Concentration**
Maxima SYBR Green/ROX qPCR Master Mix (2x)	1x
5’ primer	0.3 µM
3’ primer	0.3 µM

The mastermix was completed with a 1:10 dilution of the previously synthetized cDNA and RNase-free water to a final volume of 6.25 µl per reaction. The amplification started with an initial denaturation step at 95°C for 10 min. Following, 40 cycles of 15 sec denaturation at 95°C, 60 sec annealing at 59°C and 40 sec extension at 72°C. Applied oligonucleotide primer pairs are listed in Appendix Table 9.

Gene expression was calculated at the $\Delta\Delta C_t$-value relative to the internal reference gene *β-actin*. Since RIM1/2 β-isoforms are highly homologous to the respective α-isoforms and contain only a unique N-terminus that is too short to allow the alignment of specific primer pairs, gene expression values for the RIM1β and RIM2β isoforms were calculated. Therefore, the relative *Rims1*α expression was subtracted from the total *Rims1* expression and the relative *Rims2*α and *Rims2*γ expression was subtracted from the total *Rims2* expression, respectively.

4.3.4 RNA *in situ* hybridization

RIM4const KO male mice and WT controls, 4-6 weeks old, were deeply anesthetized with Fentanyl 0.05 mg/kg, Midazolam 5 mg/kg and Medetomidin 0.5 mg/kg. Animals were transcardially perfused with 4% PFA, the brains were removed and post-fixed with 4% PFA overnight at 4°C. Next, brains were rinsed in PBS and cryoprotected in 15% and 30% sucrose in PBS. After embedding in optimal cutting temperature compound (OCT, Tissue Tek), 20 µm thick sections were cut on a cryostat. The cutting, staining and imaging procedure was carried out by Erick Martinez, AG Blaess, University Clinic Bonn. RNA *in situ* hybridization on frozen sections was performed using RNAscope Fluorescent Multiplex Detector Reagents (323110, ACDBio, CA, USA) according to the manufacturer's instructions for fixed frozen tissue (User Manual: 323100-USM). Probes for RIM4 (Mm-RIM4-C3: 540041-C3) were designed by ACDBio. Following *in situ* hybridization, the sections were counterstained with Fluoro Nissl Green (1:150, Thermo Fisher Scientific, MA, USA) and Hoechst. Sections were rinsed three times in PBS + 0.1% Tween20 (PBT), three times in PBS and mounted in Aqua-PolyMount (18606, Polyscience Inc., PA, USA). Imaging was performed on a Zeiss Axio Observer inverted fluorescent microscope using 40x or 63x objectives (EC Plan-Neofluar, Zeiss, Germany) and structured illumination (ApoTome, Zeiss, Germany). The AxioVision MosaiX software was used to stitch images. For quantification, 40x images were used. Fluorescent puncta of single cells (Purkinje cells, cortical cells of layer III/IV and hippocampal cells) were counted in ImageJ. In total, 50 cells per mouse and brain region were analyzed.

4.3.5 RNA sequencing

Cerebellar tissue was prepared from constitutive RIM4 KO 1st mice of both genders 15-20 weeks old. For cortical tissue, RIM4const KO mice of both genders 4-6 weeks old were used. All mice were anesthetized with isoflurane and decapitated. Constitutive RIM4 WT mice in the same age range were used as controls. The cerebellum and the cortex of constitutive RIM4 mice were extracted and directly frozen in liquid nitrogen.

RNA sequencing of cerebellar tissue was performed by the AG Schulze, LIMES Institute, University Bonn. The tissue was lysed in Trizol with a Precellys homogenizer. RNA was isolated by using the miRNeasy Kit according to the manufacturer's instructions. The quality control and quantification of isolated RNA was performed on the Tapestation 2200 (Agilent Technologies Inc., CA, USA). RNA sequencing library construction was performed with the Illumina TruSeq RNA Sample Prep Kit V2 (total RNA input: 100 ng) according to the manufacturer's instructions.

Sequencing was conducted according to sequencing protocols from Illumina on a HiSeq1500 sequencer (Illumina Inc., CA, USA).

Bioinformatic data processing of RNA sequencing of cerebellar tissue was performed by the AG Schulze, LIMES Institute, University Bonn. The generated fastq files were aligned to the mouse genome (mm10). The data was processed by the removal of outliers and a normalization using the Bioconductor R-package DESeq2 (Love et al., 2014). Subsequently, RNA quantification and differential expression analysis was conducted using the Partek Genomics Suite (Partek Inc., MO, USA) performing an ANOVA model.

3'-RNA sequencing of cortical tissue was performed by the Next Generation Sequencing (NGS) Core Facility, Medical Faculty, University Bonn. Total mRNA was isolated from the previously gained tissue samples by using the RNeasy Midi Kit according to the manufacturer's instructions for 'Isolation of total mRNA from Tissue Samples', as described in chapter 4.3.2. RNA sequencing library construction for cortical mRNA (mRNA input: 500 ng) was performed with the QuantSeq 3'-mRNA-seq Library Prep kit (Lexogen, Austria) according to the manufacturer's instructions. Sequencing was conducted according to the 3' RNA sequencing protocols from Illumina on a HiSeq2500 system (Illumina Inc., CA, USA), generating 50 bp reads.

Bioinformatic data processing of 3'-RNA sequencing of cortical tissue was performed by the Bioinformatics Core Facility, Medical Faculty, University of Bonn. After trimming of Illumina Universal Adapter with cutadapt (Martin, 2011) reads were aligned to the mouse genome (mm10) with STAR (Dobin et al., 2013). Afterwards, featureCounts (Liao et al., 2014) was used to assign reads to genes based on the definitions of ENSEMBL release GRC38.94. Inclusion criteria for counting were as follows: uniquely mapped, matching strand and overlap with a single gene, for example non-ambiguous assignment. Statistical analysis was performed with the Bioconductor R-package DESeq2 (Love et al., 2014) and multiple testing adjusted p-values were obtained. Only genes with at least 2 read counts across all samples were considered for the analysis.

4.4 Cell culture

4.4.1 Transfection of neuronal cultures

Neuronal cultures were transfected at day in vitro (DIV) 2-6. For Lipofectamine transfection, the Basal Medium Eagle (BME) medium of the primary neuronal cultures was replaced by Opti-Minimal Essential Medium (MEM; Life Technologies) for 30 min at 37°C and 5% CO_2. The BME medium was stored at 37°C. Next, a dilution of plasmids and Lipofectamine2000 (Life Technologies) was prepared in Opti-MEM. In a following step, the Lipofectamine dilution was added to the plasmid dilution dropwise while vortexing. This solution was then incubated for 20 min at room temperature before adding it to the neurons. The neurons were then incubated for 2h at 37°C and 5%CO_2. Subsequently, the previously added solution was removed, the neurons were washed 2 times with Opti-MEM and were further incubated with the original BME medium.

4.5 Biochemical methods

4.5.1 Immunoblotting

Constitutive RIM3 WT and KO as well as constitutive RIM4 WT and KO mice of both genders, 15-20 weeks old, were anesthetized with isoflurane and decapitated. For constitutive RIM3 mice, thalamic tissue was removed and directly frozen in liquid nitrogen, whereas for constitutive RIM4 mice, cerebellar tissue was extracted and directly frozen in liquid nitrogen. Frozen tissue samples were homogenized with a tissue grinder in 2 ml/mg PBS pH 7.4 including a protease inhibitor cocktail (cOmplete, Roche). Subsequently, 6x Laemmlibuffer containing 378 mM TRIS-hydrochlorid, 30% glycerol, 12% sodium dodecyl sulfate (SDS), 0.06% bromphenolblue and 10% β-mercaptoethanol was added to the samples. Proteins were denaturated for 5 min at 95°C and sonicated.

In the next step, proteins were separated by SDS polyacrylamide gel electrophoresis (SDS-PAGE) and blotted on nitrocellulose or polyvinylidene difluoride (PVDF) membranes with 45 mA overnight at 4°C. To prevent unspecific antibody binding, membranes were incubated for 2 hours with 5% milk in PBS + 0.1% Triton-X100 (PBST). Afterwards, primary antibodies were incubated in 5% milk in PBST for 1.5 hours at room temperature (Appendix Table 11). Following three washing steps with PBS for 10 min each, blots were incubated with IRDye secondary antibodies for 45 min at room temperature and then scanned with an infrared scanning system (Odyssey, LI-COR, Germany). For analysis, the Fiji plugin 'Analyze gels' was used (Schindelin et al., 2012).

4.5.2 Mass spectrometry

RIM4const KO and WT male mice, 4-6 weeks old, were anesthetized with isoflurane and decapitated. The cortex and the cerebellum were isolated and homogenized with a tissue grinder in lysis buffer containing: 2% SDS, 50 mM TRIS/HCl pH 7.4, 2 mM EGTA, 2 mM EDTA, cOmplete protease inhibitor, 2 mM phenylmethylsulfonyl fluoride (PMSF), 5 mM sodium fluoride (NaF), 2 mM β-glycerophosphate, phosphatase inhibitor cocktail (Merck, Germany) and PhosphoSTOP (Roche).

Peptide preparation, LC-MS measurements and primary data analysis were performed by Dr. Marc Sylvester and the Mass Spectrometry Core Facility, Medical Faculty, University Bonn. Cell lysates were subjected to in solution preparation of peptides on centrifugal filter units modified from Leon et al., 2013; Manza et al., 2005; Masuda et al., 2008; Wiśniewski et al., 2009. In brief, solutions containing 50 µg protein were loaded onto centrifugal filter units with a 10 kDa cutoff modified PES membrane (Pall Filtersystems, Germany) and reduced with 20 mM Dithiothreitol (DTT) at 55°C for 30 min. Alkylation of thiol groups was done with 40 mM acrylamide for 30 min at room temperature. After digestion, peptides were collected and sodium deoxycholate (SDC) was precipitated with trifluoroacetic acid (TFA, 2% final). Peptides were vacuum concentrated, redissolved in 20 mM triethylammonium bicarbonate buffer (TEAB) and labeled with isobaric TM10plex reagents (Thermo Fisher Scientific, CA, USA). Redissolved and pooled peptides containing 70% acetonitrile, 0.1% formic acid (FA) were dried and fractionated to 12 fractions by isoelectric point with Offgel fractionator (Aligent Technologies, CA, USA). For LC-MS measurements, peptide separation was performed on a Dionex Ultimate 3000 RSLC nano HPLC system (Dionex GmbH, Germany). Peptides were dissolved in 0.1% FA (solvent A) and injected onto a C18 trap column (20mm length, 100µm inner diameter, ReproSil-Pur 120 C18-AQ, 1.9µm). Peptides were separated during a linear gradient from 2% to 35% solvent B (90% acetonitrile, 0.1% FA) within 120 min at 300nl/min. The nanoHPLC was coupled to an Orbitrap Fusion Lumos mass spectrometer (Thermo Fisher Scientific, CA, USA). Peptide ions between 330 and 1500 m/z were scanned in the Orbitrap detector every 3 seconds with a resolution of 120000 (maximum fill time 50 ms, AGC target $4x10^5$). In a top-speed method, peptides were subjected to collision induced dissociation for identification (CID: 0.7 Da isolation, threshold intensity 5000, normalized energy 35%) and fragments analyzed in the linear ion trap with target 10^4 and maximum fill time 50 ms. Fragmented peptide ions were excluded from repeat analysis for 20 sec. Top 5 fragment ions were chosen for synchronous precursor selection and fragmented with higher energy CID (HCD: 2 Da isolation, 65% collision energy) for detection of reporter ions in the Orbitrap analyzer (resolution 50000, maximum fill time 86 ms, target 10^5). Raw data processing was performed with Proteome Discover software 2.2.0.388 (Thermo Fisher Scientific, CA, USA). Peptide identification was done with an in-house Mascot server version 2.6.1 (Matrix Science Ltd). MS data were searched against Mus musculus sequences from SwissProt (2018/07) and contaminants (cRAP; (Mellacheruvu et al., 2013). Tryptic peptides with up to two missed cleavages were searched. Propionamine on cysteins and TMT10-plex on N-termini and lysines were set as static modifications. Mascot results were evaluated by the percolator algorithm version 3.00 as implemented in the Proteome Discoverer (Käll et al., 2008). Spectra with identifications below 1% q-value were sent to a second round of database search with semitryptic enzyme specificity (one missed cleavage allowed). Protein N-terminal acetylation, methionine oxidation, TMT on N-termini, serine, and thyrosine were then set as dynamic modifications. TMT on lysine kept static. Reporter ion intensities were extracted from the MS3 level (most confident centroid) with application of lot specific isotope corrections. Actual FDR values were typically ≤ 0.8% (peptide spectrum matches), ≤ 1.2% (peptides) and 1.0% (proteins).

Bioinformatic data processing was performed by the Bioinformatics Core Facility, Medical Faculty, University of Bonn. The downstream statistical analysis of the PSM-level MS data was carried out in the R environment (R version 3.5.1) with an in-house developed workflow. Prior to the statistical inference, the miss-qualified and non-unique peptides were filtered out from the data. In addition, the proteins which were detected or quantified by a single feature (single-hit proteins) were also removed. The data were variance-stabilized and transformed using the default method from VSN package (Huber et al., 2002). The normalized data were then rolled-up from peptide-level to protein-level by Tukey’s median polish procedure. The statistical inference for analyzing protein expression was executed using the moderated t-test from the R package limma (Ritchie et al., 2015) with default parameters and the estimated p-values were adjusted for multiple testing by the Benjamini and Hochberg method.

4.5.3 Bioinformatic analysis of transcriptomics and proteomics data sets

Differentially expressed genes and proteins of transcriptomics and proteomics data sets were identified applying thresholds of log2 (fold change) > 1 for transcriptomics and proteomics data sets. Additionally, the adjusted p-values had to be lower than 0.05 ($-\log_{10}$ p-value > 1.3). Principal component analysis (PCA) was performed with the online tool ClustVis (https://biit.cs.ut.ee/clustvis/) by importing individual gene and protein read counts per sample.

4.6 Histological methods

4.6.1 Immunocytochemistry

C56Bl/6N mouse primary cortical cultures were fixed on DIV14-16 with 4% PFA for 15 min at room temperature. Afterwards, cells were washed 3 times with PBS for 10 min and permeabilized with 0.3% Triton-X100 in PBS for 10 min. During the blocking step, cells were incubated with 10% normal goat serum (Life Technologies, CA, USA), 1% bovine serum albumin (BSA) and 0.1% Triton-X100 in PBS for 1 hour. Primary antibodies were incubated overnight in the same blocking solution at 4°C. Following three washing steps with PBS for 10 min each, fluorescent-labeled secondary antibodies were applied for three hours at room temperature (Appendix Table 10). The cells were washed again three times with PBS for 10 min and the coverslips were mounted with Moviol for microscopic analysis.

4.6.2 Immunohistochemistry

Constitutive RIM3 KO 1st and RIM4const KO mice as well as WT controls were deeply anesthetized with Fentanyl 0.05 mg/kg, Midazolam 5 mg/kg and Medetomidin 0.5 mg/kg and transcardially perfused with 4% PFA. The brains were removed and post-fixed with 4% PFA overnight at 4°C. Brain slices (50-70 µm thick) were cut on a vibratome (Microm HM600V) and collected in 12-well culture plates, filled with PBS. Slices were incubated in permeabilization solution containing 0.5% Triton-X100 in PBS for 1 hour. Afterwards, primary antibodies were incubated overnight in 0.5% Triton-X100 in PBS at 4°C. Following three washing steps in PBS for 10 min each fluorescent-labeled secondary antibodies were applied separately in 0.5% Triton-X100 in PBS for three hours at room temperature. For a nuclear staining, slices were additionally incubated with 4',6-Diamidin-2-phenylindol (DAPI; 1:100) in 0.5% Triton-X100 in PBS for 1h at room temperature. Following three washing steps in PBS for 10 min, slices were mounted with

Moviol for further analysis. Image acquisition was performed with a laser-scanning confocal microscope (A1/Ti) with a 40x objective and the NIS-Elements 4.0 acquisition software (Nikon Europe BV, Netherlands). Image analysis was performed in ImageJ (Schindelin et al., 2012).

4.6.3 β-Galactosidase expression

Constitutive RIM3 KO 1st and constitutive RIM4 KO 1st mice of both genders, 8-12 weeks old, were anesthetized with isoflurane and decapitated. The brains were rapidly removed and acute sagittal slices (400 µm thick) were cut on a vibratome (Microm HM600V). Slices were collected in 12-well culture plates, filled with PBS. For β-galactosidase staining, the β-galactosidase reporter gene staining kit (Sigma-Aldrich, Taufkirchen, Germany) was used according to the manufacturer's instructions. In short, slices were incubated for 20 min at room temperature with fixation solution and afterwards washed twice with PBS. Subsequently, slices were incubated with staining solution, containing X-Gal overnight at 37°C on a shaker. On the next day, the staining solution was removed, the slices were washed once with PBS and completely fixed with 4% PFA overnight at 4°C. The slices were washed three times for 10 min each with PBS and inserted in 1% agar for resectioning to receive slices with 70 µm thickness. Subsequently, slices were mounted with Moviol. Image acquisition was performed in collaboration with the Microscopy Core Facility, University Bonn on an AxioScanZ1 slide scanner (10x objective, 0.45 N.A., Zeiss, Germany). Images were processed with the Zen2.0 software (Zeiss, Germany).

4.7 Characterization of RIM4 mouse models

4.7.1 Verification of Purkinje cell-specific Cre recombinase expression

Pcp2$_{M}$-Cre$_{tg}$:tdTom:RIM4$^{fl/+}$ or Pcp2$_{M}$-Cre$_{tg}$:tdTom:RIM4$^{+/+}$ litters were anesthetized with isoflurane, the brains were removed and fixed in 4% PFA overnight at 4°C. The tissue was cut on a vibratome (50 µm thick, Microm HM600V, Thermo Fisher Scientific, CA, USA) and collected in 12-well culture plates, filled with PBS. Images of the slices were taken on a fluorescent microscope (Zeiss, Germany) and tdTomato-expressing cells in the cerebellum as well as in other brain regions were documented.

4.7.2 Cerebellar *in vivo* tetrode recordings

4.7.2.1 Microdrive building and implantation

Microdrives with four hand-made tetrodes were built by twisting together four 5 µm thick tungsten wires (726/612, California Fine Wire Company). The ground electrode consisted of a stainless-steel wire with a soldered surgical screw (00-96x1/16, Bilaney Consultants GmbH). The tetrodes and the reference electrode were connected to a 16-channel electrode interface board (EIB-18, Neuralynx, MT, USA) with gold pins and surrounded by a lightweight, custom-made, 3D-printed plastic housing (Figure 4.2). Shortly before implantation, the tips of the tetrodes were cut to 3 mm length with fine scissors and gold-plated to lower the impedance to 200-250 MΩ.

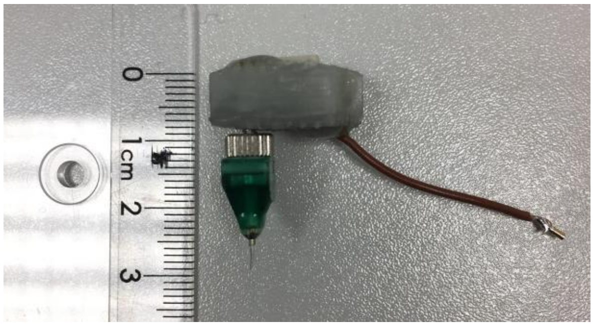

Figure 4.2: Microdrive building. The EIB board was covered by a grey plastic housing and the four connected tetrodes which were emerged at the bottom of the green housing were adjustable via the metal screw underneath the grey plastic housing. The brown wire serves as ground electrode. The bottom part of the green housing was fixed with dental cement on the skull of the mouse during implantation.

For microdrive implantation $Pcp2_{Mpin}$-Cre_{tg}:$RIM4^{fl/fl}$ mice and $Pcp2_{Mpin}$-Cre_{tg}:$RIM4^{+/+}$ mice as controls, both genders, 10-20 weeks old, were injected with Buprenorphin (0.05 mg/kg, s.c.) and anesthetized with 1-1.5% isoflurane in O_2 on a heated table (37°C). Mice were head-fixed with earbars in a stereotactic frame (David Kopf Instruments). At first, three surgical screws (00-96x1/16, stainless steel, Bilaney Consultants GmbH) were mounted on the left and right hemisphere of the skull to hold the microdrive in place. By using the coordinates anterior-posterior - 6.7 mm and medial-lateral + 0.8 mm from Bregma, the cerebellar lobules V and VI could be reached and a craniotomy was drilled at that position to implant the microdrive. The space between brain and microdrive was covered with a 1:1 mixture of $CaCl_2$ and Alginate. The screw of the reference electrode was placed in the right parietal bone. Afterwards, the lower part of the microdrive as well as the surgical screws and the reference electrode were fixed with dental cement. After the surgery, the mice could recover for one week and received on the first 3 days 0.05 mg/kg Buprenorphin and 5 mg/kg Ketoprophene.

4.7.2.2 *In vivo* single unit recordings

During the recording sessions, the mice could move freely in a Plexiglas cage (26.8 cm x 21.5 cm x 14.1 cm) equipped with a video monitoring system for simultaneous time-stamped documentation of the animal behavior. Local field potentials (LFP) and single units were recorded for a maximum of 1h per day and mouse. The implanted Microdrive was connected to a unity-gain operational preamplifier. The preamplifier output was transferred via a lightweight multiwire tether through a slip-ring commutator to the data acquisition system (Digidata Lynx SX, Neuralynx, MT, USA) with 32 digitally programmable amplifiers. Unit activity was amplified and band-pass filtered between 0.6 and 6 kHz. The LFP was recorded continuously in the 0.1-900 Hz band from all 4 wires of each tetrode. In all cases, one wire of one silent tetrode was used as reference. Spike waveforms above a trigger threshold of 30-50 µV were time stamped. The tetrodes were lowered in 30-70 µm steps into the cerebellar tissue with a maximum turning depth of 300 µm per day until a single unit signal was detected. Tetrodes were left at that position for at least 6h before single unit signals were recorded. Baseline recordings of stable single units were acquired for 10 min. Mice received during the recording period of maximum 14 days 3 times a caffeine injection (5 mg/ml in 0.9% NaCl; 25 mg/kg). After caffeine injection, single units were continuously recorded for additional 40 min. After the recording session of max. 14 days, the mice were perfused and brains were collected for histological analysis (DAPI staining, described in chapter 4.6.2) to determine tetrode positions.

4.7.2.3 Data analysis

Data analysis of *in vivo* tetrode recordings was performed in MATLAB (MathWorks®). All applied analysis scripts were written by Assistant Professor Laura A. Ewell, Institute of experimental epileptology and cognition research, University Clinic Bonn. For spike identification, single units were manually sorted using MClust (MClust 3.5, written by A. David Redish; http://redishlab.neuroscience.umn.edu/MClust/MClust.html). Accepted for analysis were only those clusters of one recording session which persisted in the same region of parameter space, showed no shape changes, were distinct from noise and stayed inside the cluster boundary.

Spike rates as well as CoV of ISIs were calculated by binning the spike times (bin = 1 sec) 10 min before and 40 min after caffeine injection. To analyze the appearance of the episodically occurring motor impairments in $\mathrm{Pcp2_{Mpin}}$-$\mathrm{Cre_{tg}}$:$\mathrm{RIM4^{fl/fl}}$ mice, time-stamped videos were taken. Start of the ataxic phase of the motor impairments was defined as the time point after caffeine injection when the mouse started lifting the hind limbs. The dystonic phase of the motor impairments was defined as the time point when the mouse showed now more movement and appeared paralyzed.

4.8 Direct stochastic optical reconstruction microscopy (dSTORM)

The need to investigate structures in nanometer resolution became more and more important in recent years. Therefore, super-resolution microscopy methods were invented. In contrast to normal light microscopy, super-resolution microscopy allows acquisition of structures with very high resolution without the restriction of the diffraction limit of light. Ernst Abbe postulated in 1873 that the diffraction limit of light is defined by the numerical aperture (N.A.) of a microscope objective and the wavelength λ: $d = {}^{\lambda}/_{2\,N.A.}$

With this formula, the calculated resolution of normal light microscopy is about 200 nm in lateral (x-y) and 600 nm in axial (z) direction. The resolution can be up to 10-fold higher using super-resolution techniques. In the following chapters the focus will be set on direct stochastic optical reconstruction microscopy (dSTORM). Apart from stochastic super-resolution techniques, deterministic super-resolution techniques, for example stimulated emission depletion (STED) microscopy were invented gaining similar increases in resolution.

The dSTORM technique relies on the stochastically switching of fluorescent molecules to their dark triplet state (‘OFF’ state) such, that only a small subset of fluorophores is fluorescent at the same time (‘ON’ state). By repeating this over many acquisition cycles, other subsets of fluorophores turn to their ‘ON’ states. The position in space of each fluorescent molecule can be determined with nanometer precision by Gaussian fitting in a series of imaging cycles. These positions are then used to reconstruct the high-resolution overall dSTORM image (Figure 4.3; (Rust et al., 2006; Thompson et al., 2002).

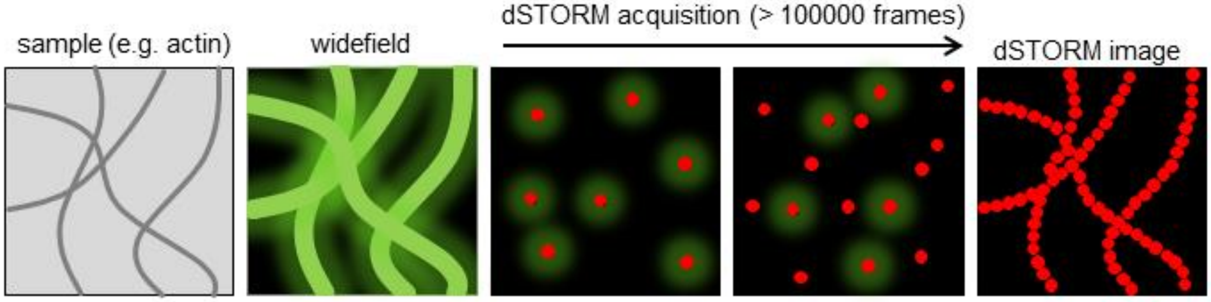

Figure 4.3: Scheme of dSTORM image acquisition. *From left to right:* Sample structures were immunocytochemically stained with primary and secondary antibodies. In widefield fluorescence imaging, these structures appeared very large. During dSTORM acquisition, only a subset of fluorophores is fluorescent at the same time over multiple imaging cycles (red dots). The positions of the fluorescent molecules are determined by Gaussian fitting and a high-resolution dSTORM image is reconstructed. Adapted from Bates et al., 2008.

Photo-switchable fluorophores used for this technique need to carry special features. Their fluorescence emission should be convertible between fluorescent and non-fluorescent states, controlled by an external light source. Importantly, the photo-switching capability of fluorescent molecules is dependent on thiol-containing components, for example β-mercaptoethanol or β-mercaptoethylamine (MEA) in the imaging buffer (Bates et al., 2005). Very suitable dyes for this application are synthetic cyanine dyes, for example Cy5 or Alexa Fluor 647 dyes (Bates et al., 2007).

4.8.1 Imaging setup and image acquisition

The dSTORM imaging setup consisted of a Leica SR GSD 3D microscope (Leica Microsystems, Germany) equipped with a 160x oil immersion objective (1.47 N.A.) and a suppressed motion (SuMo) stage to reduce stage drift. The setup contained 405 nm- (30 mW), 488 nm- (300 mW), 532 nm- (500 mW) and 642 nm-lasers (500 mW). The excitation light was reflected to the sample either via single band or quad band emission filters (Appendix Table 15). A sCMOS camera (pco.edge4.2, pco) was used to acquire the dSTORM video sequence with frame rates of 100-500 Hz.

Primary cortical neurons were seeded in 12-well culture plates on precision coverslips (170 ± 5 µm thickness, Marienfeld) and stained as described in chapter 4.6.1. Labelled cells were imaged in GLOXY-MEA dSTORM buffer, consisting of 50 mM MEA, 10% (v/v) of a 250 g/l solution of glucose, 0.5 mg/ml glucose oxidase, 40 mg/ml catalase in PBS, pH 7.6 (Nahidiazar et al., 2016). Coverslips were mounted on depression slides (Marienfeld, Germany), filled with dSTORM buffer and sealed with Twinsil silicon glue (Picodent, Germany).

With the following experiments, the Leica SR GSD 3D system was established and evaluated regarding its technical properties and imaging characteristics. Analysis of the spectral crosstalk between acquisition channels and the localization accuracy of detected blink events were performed to gain insights in the precision of the system and underlying information about how the system works. The results of these experiments were important for follow-up investigations, for example to determine the influence of the serine-arginine protein kinase 2 (SRPK2) on synaptic and extrasynaptic ELKS clusters in primary neuronal cultures (chapter 7.1).

4.8.2 Photophysical behavior of Alexa Fluor 647 – definition of individual molecule blinking events

As already stated above, the underlying mechanism for dSTORM as well as for other super-resolution imaging methods are single fluorescent molecules that can be precisely located in nanometer accuracy (Thompson et al., 2002). Among many, one prominent candidate fluorophore for these applications is Alexa Fluor 647 (AF647). By applying a laser light to the fluorophore in an imaging buffer containing thiol-components and an oxygen-scavenger system, its fluorescence emission can be switched between fluorescent 'ON' and non-fluorescent 'OFF' states. Thereby, allowing only a small subset of fluorophores to remain in the ON state at the same time. In the following experiments, the photophysical behavior of the AF647 dye was investigated using the Leica SR GSD 3D system and the GLOXY-MEA imaging buffer. Neuronal cultures were stained with a primary antibody against ELKS and a secondary antibody labelled with AF647. Single photo-switching events of the AF647 molecules could be detected using the dSTORM mode of the Leica imaging software (Figure 4.4).

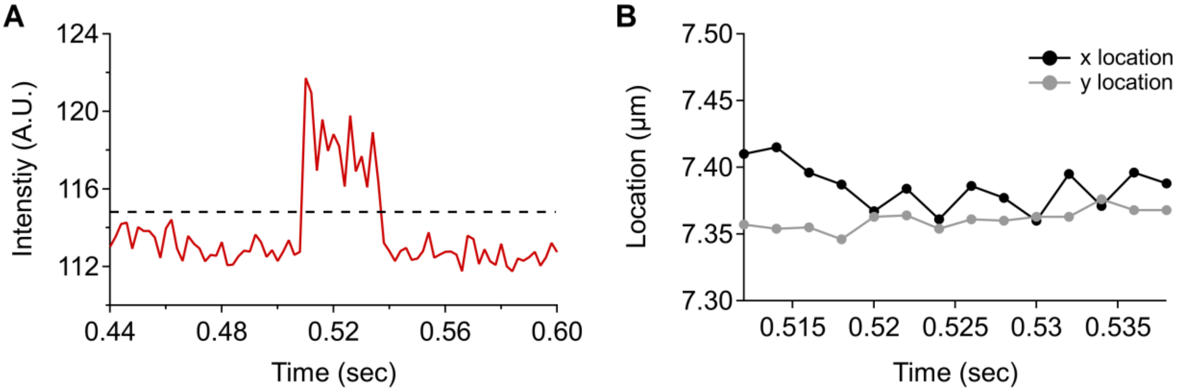

Figure 4.4: Photo-switching of AF647. (A) Example photo-switching event of AF647. The dotted line represents the detection threshold of photo-switching. The fluorescence intensity below the threshold was defined as the OFF state was not included in the dSTORM reconstruction. Fluorescence intensity above the dotted line was detected as the ON state of the fluorophore and therefore inserted in the dSTORM reconstruction. **(B)** The location in X and Y was plotted for the ON state of the AF647 molecule shown in (A).

In an ideal case, the photo-switching events of one AF647 fluorophore last always the same time and appear at the exact same position of the imaging area. However, by screening several AF647 photo-switching events in the acquired raw image sequences, it became apparent that the duration as well as the nanometer location of detected photo-switching events varied in a small range over time. Therefore, parameters for a post-acquisition filtering were needed in order to define the detection of individual molecule blinking events. The Leica imaging software allows to re-calculate the 2D dSTORM density histogram from the acquired raw image sequence and the resulting list of detected blink events by inserting values for the parameters ‘max. allowed XY shift’ and ‘max. ON time’. All events which fall into these defined values are counted as one event. At first, the value for the maximum allowed lateral (XY) shift was determined. For this reason, one acquired ELKS-AF647 raw image sequence was chosen and the number of detected photo-switching events after applying different values for the post-acquisition filter ‘max. allowed XY shift’ were plotted (Figure 4.5 A). The plateau value of detected photo-switching events was reached with a max. allowed XY shift of 70 nm. Calculation the first derivative of the curve shown in Figure 4.5 A indicated that at 15 nm max. allowed XY shift the number of events which got split was largest. In addition, the first derivative also unveiled that with a max. allowed XY shift of 70 nm almost all detected photo-switching events of the investigated AF647 fluorescent molecules were included (Figure 4.5 B).

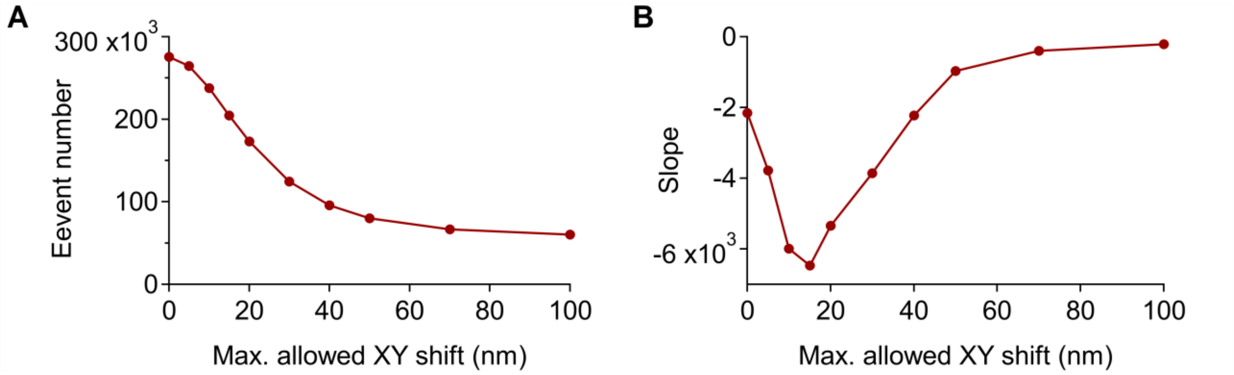

Figure 4.5: Determination of the max. lateral shift for AF647 photo-switching events. (A) The number of detected photo-switching events were plotted against different values for the max. allowed XY shift, determined on one raw image sequence in the Leica imaging software. **(B)** Calculation of the first derivative of the curve shown in (A) unveils that at 15 nm max. allowed XY shift, the largest number of events got split. At 70 nm almost all detected photo-switching events were included.

Next, the value for the max. ON time of single AF647 photo-switching events was determined. Important to note is that the analysis underlying dSTORM raw image sequences were acquired with an exposure time of 2 msec. In order to investigate how long the photo-switching events lasted, the same dSTORM raw image sequence as for the determination of the max. XY shift was used. Different values for the max. ON time in consecutive frames as well as for the max. XY shift were inserted in the post-acquisition filter menu of the Leica imaging software. The number of detected photo-switching events was noted after re-calculation of the respective dSTORM density histogram. These values were plotted in a 3D graph where the marker size represents the number of detected photo-switching events (Figure 4.6). All curves with different max. allowed XY shifts reach a plateau of similar marker sizes at 10 frames. Therefore, the max ON time of AF647 photo-switching events was set to 10 consecutive frames or 20 msec respectively. Thus, all events which were detected within 10 frames in a XY range of 70 nm were counted as one event.

In conclusion, photo-switching events of single AF647 fluorescent molecules were detected in immunocytochemical stainings with the Leica SR GSD 3D system. These events varied in a small range in their duration and nanometer localization. In turn, AF647 photo-switching events were counted as one event when they appeared with a max. allowed XY shift of 70 nm in up to 10 consecutive frames. Consequently, the total number of detected events was decreased after application of the post-acquisition filter. However, the precision of detecting only real events was higher.

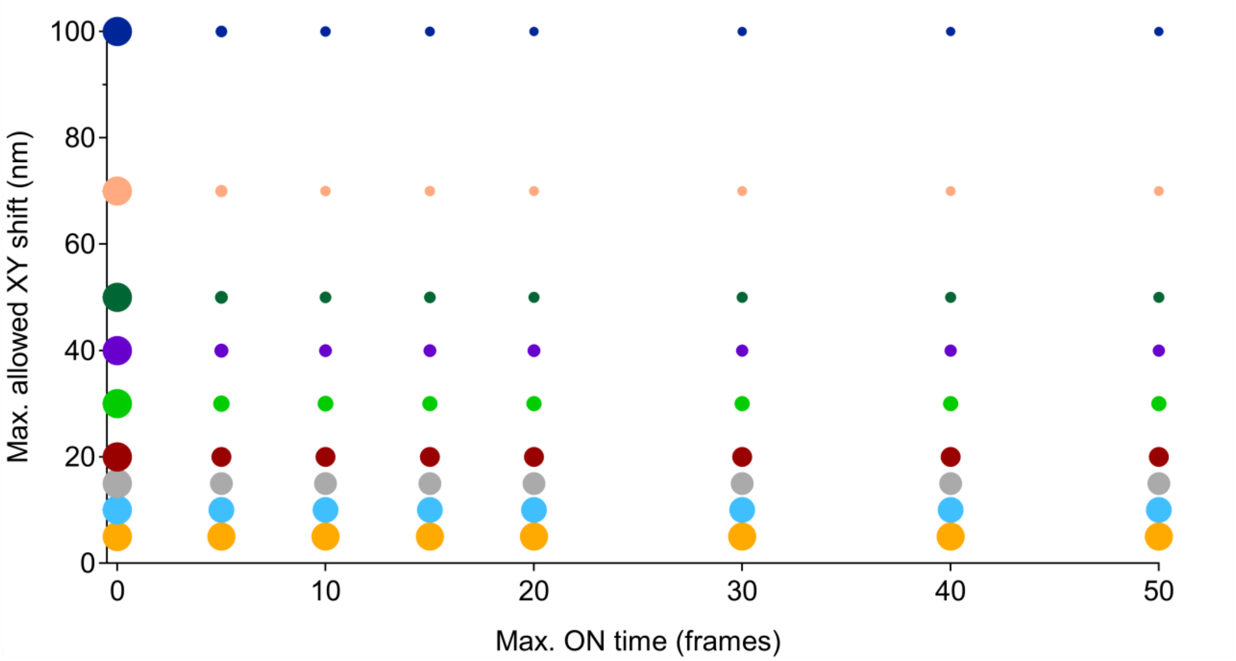

Figure 4.6: 3D plot for determination of the max. ON time of AF647 photo-switching events. The max. ON time of AF647 photo-switching events was plotted against the max. allowed XY distance. The marker size represents the number of detected photo-switching events. A plateau level of similar marker sizes was reached at 10 frames which indicated that almost all AF647 ON states lasted up to 20 msec.

4.8.3 Localization accuracy of the Leica SR GSD 3D system

The dSTORM technique, especially the reconstruction of the high-resolution dSTORM images relies on the exact localization of stochastically occurring blink events. Therefore, it is important that the imaging system is free of drift and any kind of movement during the raw data acquisition. Furthermore, the alignment of filter cubes and lasers needs to be appropriate in order to prevent inaccurate detection of blink events or unprecise reconstruction of the dSTORM images. The following experiments were performed to investigate these properties of the Leica GSD SR 3D system.

4.8.3.1 Stage drift

To determine if a potential stage drift of the Leica SR GSD 3D system in lateral location occurs during the imaging sessions, goldbeads (80 nm diameter, Abberior Instruments, Germany) mounted on glass slides were used for acquisition of 20 min time series. These beads are advantageous because of a small diameter and the capability to emit light upon excitation with the 647 nm laser without much photobleaching over longer time periods. Image frames were acquired with the 642 nm-laser (35% laser power) and the corresponding single band emission filter. Image frames were acquired in the widefield mode of the Leica image acquisition software with a time interval of 1 sec in between images. The slide carrying the goldbeads was placed in the microscope 15 min before the experiment. The exact lateral location of 3 goldbeads per acquisition was determined with the Fiji plugin TrackMate for single particle tracking (Tinevez et al., 2017). The TrackMate plugin fits spot-like objects that are segmented in multiple frames with a gaussian fit to determine X- and Y-coordinates and reconstructs the trajectory of these spots over time. From these results the difference in nm between the first and the last frame of the goldbeads in X- and Y-location was calculated and plotted as Δt. The mean Δt in x-direction was 9 nm, whereas the mean Δt in Y-direction was accounted to -57 nm and therefore noticeably larger (Figure 4.7).

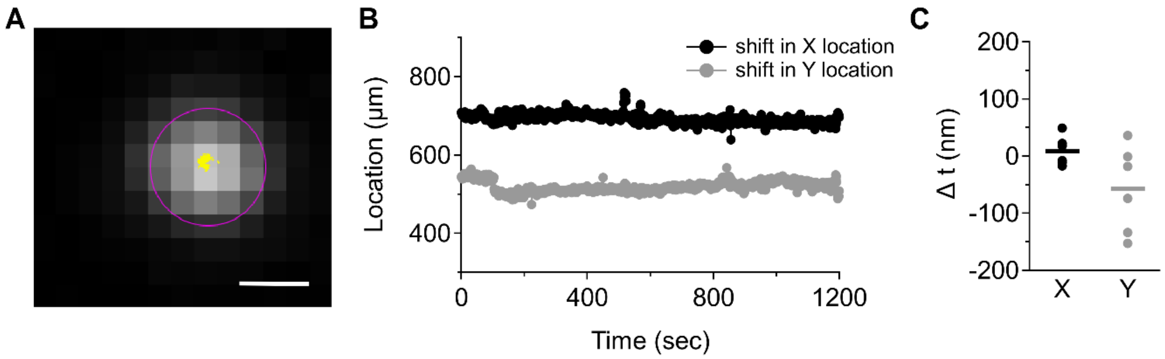

Figure 4.7: Determination of X-/Y-shift. (A) Example goldbead acquisition (20 min) encircled with a pink detection line and the yellow tracking line. Scale bar: 300 nm. **(B)** Plotted X- and Y-location of the goldbead depicted in (A) over 20 min acquisition time. **(C)** The difference between the first and the last frame of the goldbeads in X- and Y-location was calculated and plotted as Δt. Line = mean Δt, dots represent mean values for each acquisition. n = 6 acquisitions, 3 ROIs per acquisition.

4.8.3.2 Precision of 2D localization detection

In addition to the stage drift, it was important to determine the maximum resolution of the Leica SR GSD 3D system. For that reason, the GATTA-PAINT Nanoruler (GATTAquant, Germany) decorated with Atto655- and Atto565-fluorescent molecules in 40 nm distance was chosen. The underlying mechanism of the Nanoruler is the DNA-PAINT technology, consisting of a DNA docking strand, fixed on the glass slide with a specific distance of 40 nm and a complementary dye-labeled imager DNA strand. Transient binding of the imager strand to the docking strand can be detected as blinking and is very insensitive to photobleaching (Figure 4.8; Schnitzbauer et al., 2017).

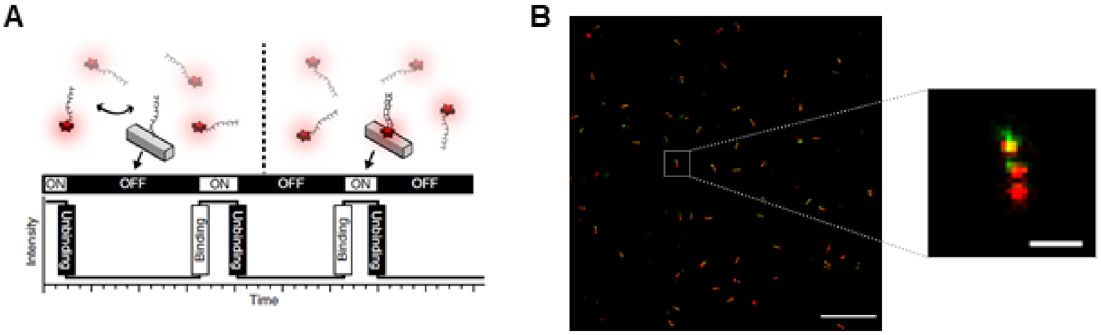

Figure 4.8: GATTA-PAINT Nanoruler use the DNA-PAINT concept. (A) Concept of DNA-PAINT. Dye-labeled DNA strands bind transiently to their complementary target sequence attached to the molecule of interest. The transient binding of dye-labeled DNA strands can be detected as blink events, here illustrated by intensity over time. Adapted from Schnitzbauer et al., 2017. **(B)** *Left:* Overview image of the GATTA-PAINT Nanoruler 40 RG. Scale bar: 1 µm. *Right:* Zoom-in to one Nanoruler with 40 nm distance between 2 fluorescent spots. Scale bar: 100 nm. Image adapted from www.gattaquant.com.

The slide carrying the GATTA-PAINT Nanoruler was placed in the microscope 1h before the imaging session to pre-warm the glass slide which was stored at 4°C. Raw image stacks with 30-50% laser power and 150000 frames at 500 Hz were acquired with the quad-band emission filter after 30 sec of pumping with 50% laser power of the 532 nm- and 642 nm-laser. The 405 nm-laser, which returns OFF state fluorescent molecules back to their ON state (back-pumping) was set to 10% laser power during acquisition to increase the number blink events. The detection threshold for stochastically occurring blink events was set in the Leica image acquisition software to 15 photons/pixel. Detected blink events were fitted with a ‘direct fit’ in the Leica acquisition software, on the assumption that the emitted light of each blink event was gaussian distributed. 2D histograms were rendered from localizations of blink events with a pixel size of 10 nm. Evaluation of X-Y distances between fluorescent spots was performed with Fiji using the ‘line’ tool and the ‘Plot profile’ function (Schindelin et al., 2012). The gray value intensities of the 532 nm- and the 642 nm-channel were plotted. Strikingly, the peak-to-peak distance for both channels could be accounted to around 40 nm (Figure 4.9). This experiment ruled out, that structures up to 40 nm could be resolved with the Leica SR GSD 3D system. Nanorulers with lower distances up to 20 nm, which would be theoretically the maximum archivable resolution with this system, were not tested.

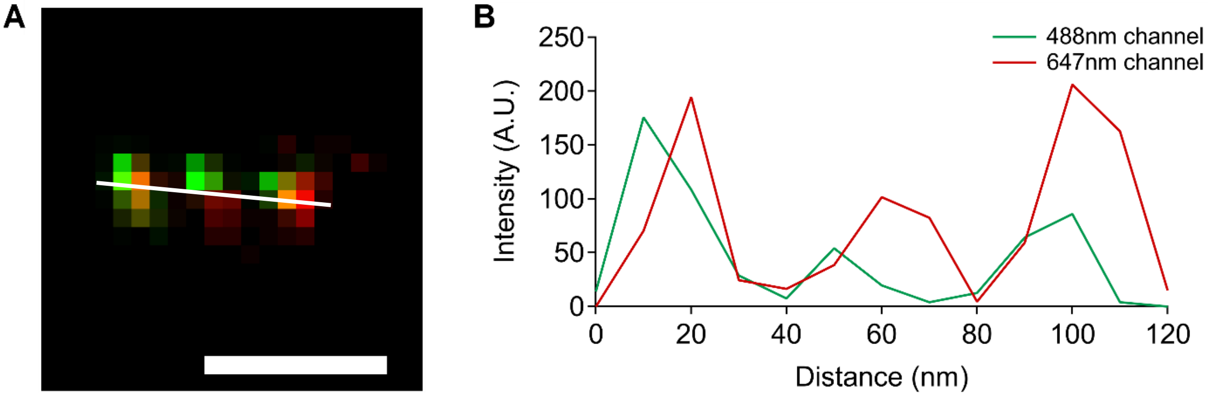

Figure 4.9: dSTORM resolution assign. (A) The GATTA-PAINT Nanoruler 40RG was used to evaluate the resolution. The fluorescent molecules Atto655 and Atto565 had a predefined distance of 40 nm. Scale bar: 100 nm. **(B)** Gray value intensities along the white line in (A) were plotted against the distance in nm. In both imaging channels the peak-to-peak distance could be accounted to about 40 nm.

4.8.3.3 Channel offset

Multicolor dSTORM imaging was performed by sequentially acquiring raw image frames with the different lasers and filtercubes of the Leica GSD SR 3D system and the overlay of the calculated 2D dSTORM histograms should represent the true biological structure. In these kinds of experiments, the channel offset defines the shift of multifluorescent spots in the different acquisition channels. In an ideal case, this shift should be within the accuracy of a single pixel.

Multifluorescent beads (Fluoresbrite® Multifluorescent Microspheres, 0.2 µm, Polysciences Inc., PA, USA) were used to determine the shift between acquisition channels (488 nm-, 532 nm- and 642 nm-channels). Thus, each of these beads is labeled with three different fluorescent molecules and can be imaged with the 3 available lasers of the Leica GSD SR 3D system. After dilution in PBS (1:1000) the beads were imaged in a glass-bottom petri dish (diameter 27 mm, Thermo Fisher Scientific, CA, USA) on 5 subsequent days. Imaging was performed in the widefield mode of the Leica image acquisition software with a time interval of 0.1 sec and 20 frames in each of the imaging channels. For 488 nm fluorescence 10% laser power, for 532 nm 5% laser power and for 642 nm 50% laser power was used for image acquisition. Image stacks were merged and analyzed with the Fiji plugin GaussFit_OnSpot (developed by Peter Haub and Dr. Tobias Meckel, University Darmstadt, Germany). Therefore, 5 ROIs per image were manually selected in all 4 corners and the middle of the image. These regions were chosen to cover the whole field of view. In each of these ROIs 5 manually selected multifluorescent beads were analyzed with a Gaussian fit and the NelderMead fit method in Fiji (Figure 4.10 A-C). The mean X- and Y-locations of 20 frames were calculated for each channel and the X- and Y-location differences between 488 nm- and 642 nm-channel and 532 nm- and 642 nm-channel were determined (Figure 4.10 D,E). Lowest deviations between channels could be observed in the middle of the field of view. Whereas, in the four investigated corners the Δ of the Gaussian fits ranged between +31.0 nm/-18.8 nm in X-location and between +16.8 nm/-17.8 nm in Y-location comparing the 488 nm and the 642 nm channel. Less deviation could be observed comparing the 532 nm and the 642 nm channel where the Δ of the Gaussian fits ranged between +16.3 nm/-13.3 nm in X-location and +16.1 nm/-7.4 nm in Y-location.

In conclusion, the localization accuracy of the Leica SR GSD 3D system was evaluated in different perspectives. The overall lateral shift, mainly evoked by stage drift due to thermal fluctuations, was smaller in X- than in Y-location. The resolution of the system was determined to 40 nm but could probably be accounted to 20 nm when tested. The offset between channels is low for the middle area of the field of view. In addition, the overall mean Δ Gaussian fit indicated that the offset of the channels in all investigated regions of the widefield image was lower than the size of one pixel of the reconstructed dSTORM image. These results suggest that channel offset should not influence multicolor dSTORM imaging to a massive extend. Small deviations of the imaging channels could be manually aligned in the Leica imaging software. Furthermore, since this analysis was carried out in the widefield mode of the Leica imaging software, the middle area (18 µm x 18 µm) of the field of view is mainly important because here the dSTORM acquisitions take place.

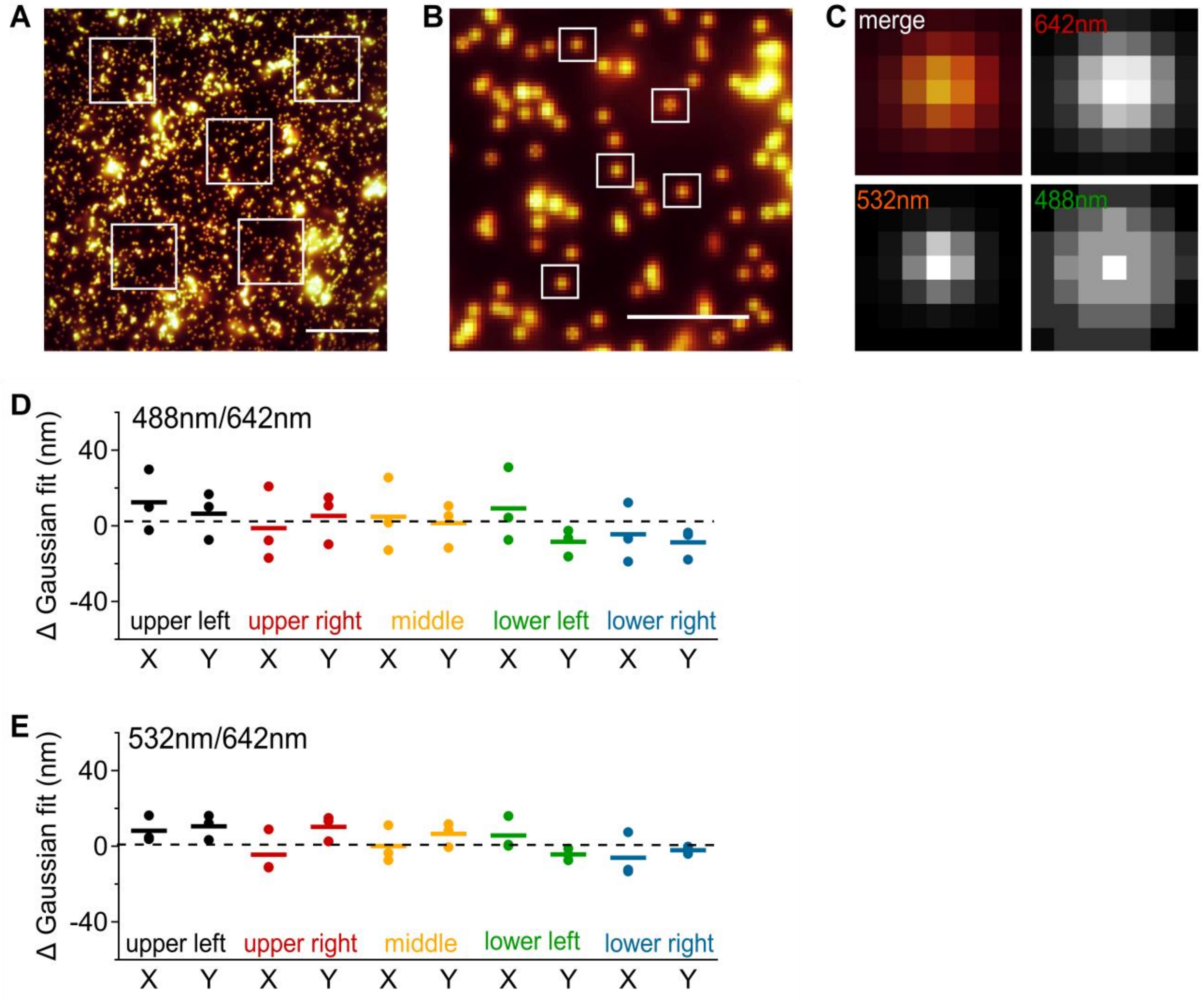

Figure 4.10: Multicolor bead analysis for channel offset. (A) Multicolor fluorescent beads were imaged in widefield mode with the 3 available lasers. Image stacks were merged, and 5 ROIs were manually selected to cover all areas of the field of view. Scale bar: 10 µm. **(B)** Zoom into one of the selected ROIs in (A). 5 multifluorescent beads were selected per ROI. Scale bar: 3 µm. **(C)** Zoom-in to one multifluorescent bead, marked in (B). Depicted as merged and single channel images. 1 px = 100 nm. **(D)** Quantification of the deviation of X- and Y-location of multifluorescent beads, comparing the 488 nm and the 642 nm channel. Horizontal bars represent the overall mean ∆ Gaussian fit; dots represent the mean values of 5 multifluorescent beads, imaged on 3 different days. **(E)** Quantification of the deviation of X- and Y-location of multifluorescent beads, comparing the 532 nm and the 642 nm channel. Horizontal bars represent

the overall mean ∆ Gaussian fit; dots represent the mean values of 5 multifluorescent beads, imaged on 3 different days.

4.8.4 Spectral crosstalk analysis

For fluorescence microscopy, mainly for multicolor imaging it is important to be able to exclude spectral crosstalk between imaging channels. Spectral crosstalk occurs either by excitation of multiple fluorophores by a single excitation wavelength (cross-excitation) or by detection of unwanted fluorescent signals in overlapping emission spectra (‘bleed-through’). Spectral crosstalk applies for super-resolution microscopy as well. In order to identify potential spectral crosstalk in the Leica SR GSD 3D system, primary cortical cultures were stained with an antibody against the presynaptic protein bassoon. For secondary antibody labelling Alexa Fluor dyes conjugated to 488 nm- (AF488) 532 nm- (AF532) or 647 nm-fluorescent molecules (AF647; Invitrogen; Table 12) were used to analyze the crosstalk between acquisition channels (488 nm, 532 nm and 642 nm). The emission bands of the single as well as the quad band filter cubes together with the excitation and emission spectra of the dyes already pointed towards a potential ‘bleed-through’ and cross-excitation between channels (Figure 4.11).

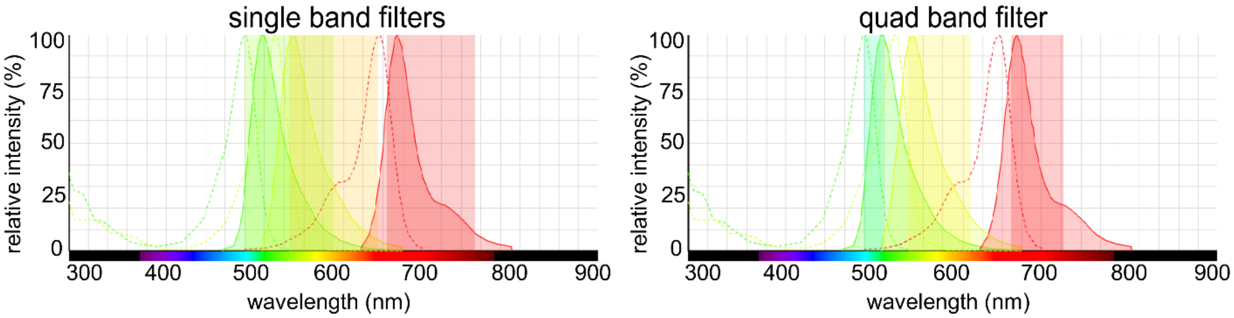

Figure 4.11: Spectral profiles of fluorescent dyes and emission bands of filters. Dotted lines represent the excitation, solid lines the emission spectra of the fluorescent dyes. Green = AF488, yellow = AF532 and red = AF647. *Left:* Bars represent the emission bands of the single band filter cubes mounted in the Leica SR GSD 3D system. *Right:* Bars represent the emission bands of the quad band filter cube of the Leica SR GSD 3D system. Generated by: www.thermofisher.com/order/spectra-viewer.

Theoretical calculation of the spectral crosstalk unveiled in the single band filters a potential cross-excitation of AF532 in the green single filter (84.7%; emission band 550/100). Furthermore, a ‘bleed-through’ of AF488 fluorescence could be calculated for the orange single filter (23.6%; emission band 600/100). All other values for the calculated spectral crosstalk were below 1% and therefore negligible (Figure 4.12 A). The calculated spectral crosstalk was lower for the quad band filter. Here, only a ‘bleed-through’ of the AF488 dye could be detected in the orange emission band of the filter (22.4%; emission band 585/70). Whereas the calculated spectral crosstalk was below 1% for all other conditions (Figure 4.12 B).

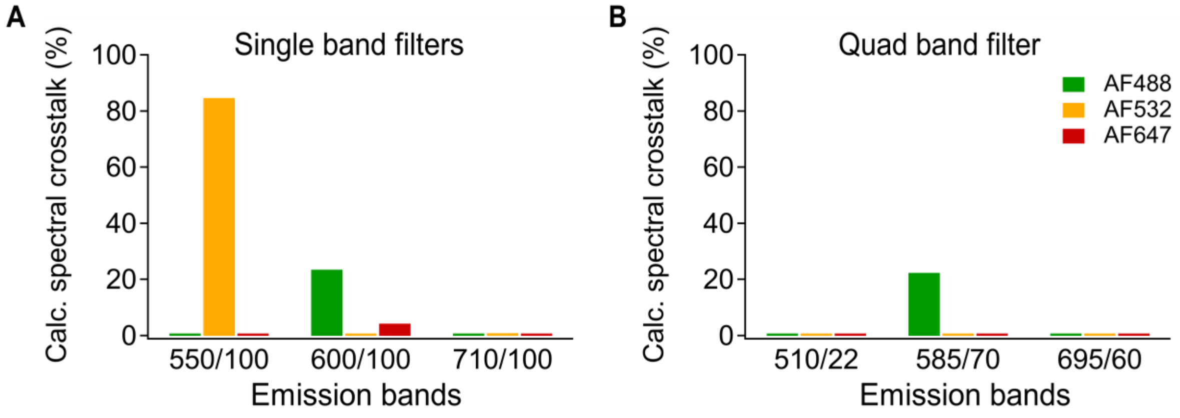

Figure 4.12: Theoretical cross-excitation and 'bleed-through' of the single and quad band filters. (A) Calculated spectral crosstalk of single band filters and the associated emission band. **(B)** Calculated spectral crosstalk of quad band filter. Calculation of the spectral crosstalk was performed by www.thermofisher.com/order/spectra-viewer.

To further investigate the spectral crosstalk occurring during multicolor acquisitions with the Leica SR GSD 3D system, widefield images were acquired with the single filters and the corresponding laser (100 ms exposure time; 10% laser power). Subsequently, the dSTORM raw image sequences of bassoon stainings were acquired with single and quad band filter cubes. Single band emission filters were inserted in the Leica SR GSD 3D system and could only be used with the corresponding laser, for example, the 488 nm filter cube could only be used with the 488 nm laser. Whereas the quad band filter cube could be used with all 3 lasers of the system. The dSTORM raw image sequences were acquired by pumping all fluorescent molecules to the dark state for 30 sec with 50% laser power, followed by the recording of 150000 frames at 500 Hz and 30% laser power. The detection threshold for stochastically occurring blink events was set in the Leica acquisition software to 15 photons/pixel for AF532 and AF642 dyes and 10 photons/pixel for the AF488 dye. Detected blink events were fitted with a 'direct fit' in the Leica acquisition software, on the assumption that the emitted light of each blink event was gaussian distributed. 2D histograms were rendered from localizations of blink events with a pixel size of 20 nm. Spectral crosstalk analysis of 2D histograms was performed in Fiji (Schindelin et al., 2012). 5 ROIs per acquisition were manually chosen and the background-corrected mean fluorescence intensity per pixel was determined (Figure 4.13 A,B). The mean fluorescence intensities per pixel ratio of dSTORM images were calculated and used to determine the ratio of crosstalk in between channels. For the single band emission filters, the highest cross-excitation of AF532 could be detected in the green filter (70.9%; emission band 550/100) Furthermore, a high 'bleed-through' of the AF488 dye into the orange filter could be detected (42.1%; emission band 600/100). All other conditions using the single band emission filters showed a spectral crosstalk ratio < 10% (Figure 4.13 C). Using the quad band emission filter, the highest ‘bleed-through’ of the AF488 dye could be detected in the orange filter, similarly to the results obtained for the single filters (72.7%; emission band 585/70). In addition, a high cross-excitation of the AF532 dye was noticed in the green filter (58.4%; emission band 510/22). Even a small ‘bleed-through’ of the AF532 dye into the red channel could be detected (14.4%; emission band 695/60). All other conditions using the quad band emission filter cube showed crosstalk ratios < 10% (Figure 4.13 D).

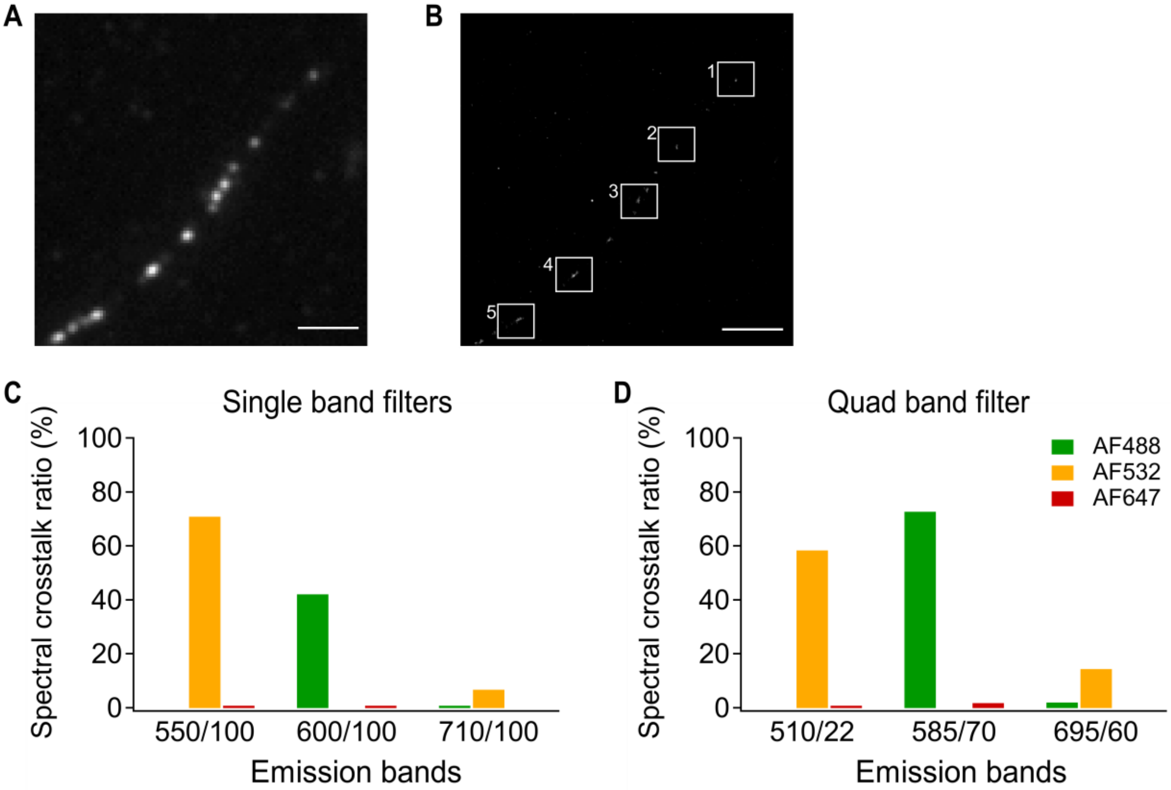

Figure 4.13: Determination of spectral crosstalk ratios of single and quad band emission filters. (A) Widefield fluorescence image of a bassoon-AF488 staining in the orange single filter (600/100 emission band). Detection of the AF488 signal points to a high ‘bleed-through’. Scale bar: 10 µm. **(B)** dSTORM 2D density histogram of the structure shown in (A). 5 ROIs were manually selected for spectral crosstalk analysis. Scale bar: 10 µm. **(C)** Quantification of spectral crosstalk ratios for the single band emission filters of the Leica SR GSD 3D system. **(D)** Quantification of the spectral crosstalk ratios for the quad band emission filter cube of the Leica SR GSD 3D system.

In conclusion, the highest measured spectral crosstalk was observed in the 488 nm and the 532 nm channels for the single band emission filters as well as for the quad band emission filter. In contrast, the calculated values for these dyes and filter emission bands were remarkably lower. These results point towards a possibility for adjustment of imaging settings, for instance imaging laserpower or dye concentration to reduce the potential spectral crosstalk. Nevertheless, for future investigations it would be preferable to use, if possible, AF488/647 or AF532/647 labeling for multicolor imaging to prevent high spectral crosstalk and increase the signal quality.

4.8.5 Establishment of 3D dSTORM imaging of synapses

After successful evaluation of the properties of the Leica SR GSD 3D system in 2D, the next step was to establish a 3D imaging paradigm. By insertion of an astigmatism lens into the optical pathway of the microscope, it was possible to perform 3D dSTORM imaging under the same conditions as described before. With the astigmatism lens is was possible to determine not only the exact lateral position of fluorophores, but also their axial location (Huang et al., 2008). For a first test run, a pre- and postsynaptic immunocytochemical staining of primary neuronal cultures was used, as already shown in previous studies (Dani et al., 2010). Primary cortical neurons cultured on coverslips in 12-well plates were stained with the protocol described in chapter 4.6.1 at DIV15. Antibodies against bassoon, a presynaptic protein of the active zone and homer1, a postsynaptic scaffolding protein, mainly located at the postsynaptic density were used (Appendix Table 13). For fluorescent labeling of the primary antibodies, AF488 and AF647 were applied. Overview widefield images were always acquired with the quad band emission filters and the 488 nm- as well as the 642 nm-laser (100 ms exposure time; 10% laser power). 3D dSTORM imaging was performed in the ‘GSD 3D mode’ of the Leica acquisition software, which allowed to insert the astigmatism lens into the optical pathway of the microscope to determine the axial position of fluorophores. Sequential dSTORM raw image acquisition was performed with the quad band emission filter and the 642 nm- and 488 nm-laser. After pumping all AF647 molecules to the dark state with 50% laser power of the 642 nm-laser for 5 sec, 150000 frames were acquired at 500 Hz with 30% laser power of the 642 nm-laser. Directly afterwards without interruption, all AF488 molecules were pumped to the dark state with 70% laser power of the 488 nm-laser for 60 sec. Followed by the acquisition of 30000 raw image frames with 33 Hz and 50% laser power of the 488 nm-laser. The detection threshold for stochastically occurring blink events were set in the Leica acquisition software to 15 photons/pixel for the 642 nm channel and 60 photons/pixel for the 488 nm channel. The detected blink events were fit with a ‘direct fit’ in the Leica acquisition software, on the assumption that the emitted light of each blink event was gaussian distributed. 2D and 3D histograms were rendered from localizations of blink events with a pixel size of 20 nm in lateral and 50 nm in axial direction (Figure 4.14).

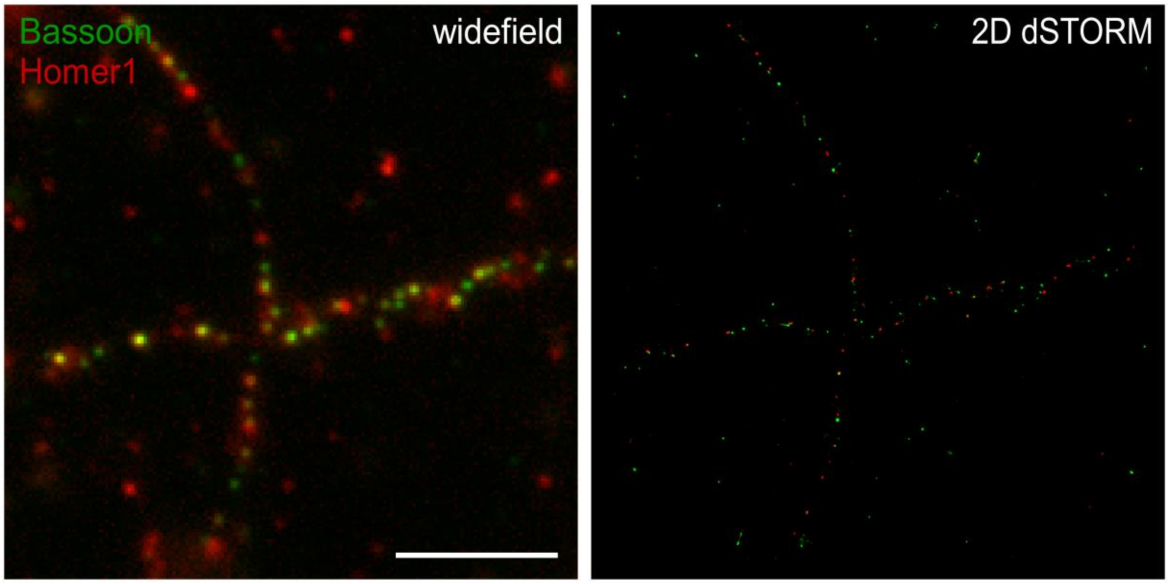

Figure 4.14: 2D dSTORM imaging of synapses. *Left:* Widefield fluorescence image of bassoon and homer1 staining in dendrites of primary neuronal cultures unveiled a partially overlapping punctate staining pattern. For labeling AF488 and AF647 fluorescent dyes were used. *Right:* 2D dSTORM density histogram of the same region shows more distinct staining of synaptic structures. Scale bar: 5 µm.

3D reconstruction of pre- and postsynapses was performed in the 'Analysis Mode' of the Leica acquisition software. Zoom-in to one synapse unveiled already in 2D dSTORM density histograms that bassoon and homer1 fluorescent spots were not completely overlapping, as previously described for confocal or normal fluorescence microscopy. In 3D dSTORM density histograms the synaptic pre- and postsynaptic structures became better visible and appeared, depending on the viewing angle as elliptical discs separated by the synaptic cleft (Figure 4.15).

In conclusion, it was possible to perform dual-color 3D dSTORM imaging with the Leica SR GSD 3D system by using the fluorescent dyes AF488 and AF647. The synaptic structures were clearly resolvable, and their dimensions matched previously published data.

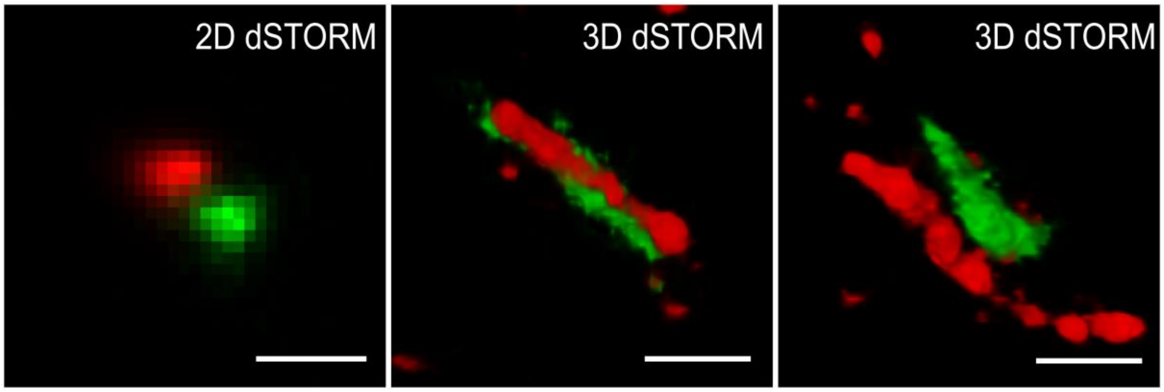

Figure 4.15: 3D dSTORM imaging of synapses. *Left:* Zoom-in to one synapse acquired with 2D dSTORM imaging. Pre- and postsynaptic parts were clearly visible and separated. *Middle, right:* Two examples of synapses with bassoon and homer1 stainings acquired in 3D dSTORM mode. Depending on the viewing angle, the pre- and postsynaptic parts appeared as elliptical discs, separated by the synaptic cleft. Scale bar: 100 nm.

4.8.6 dSTORM cluster analysis

The dSTORM technique allows to acquire images of biological structures with a high spatial resolution. These biological structures contain proteins which can be scattered, clustered or randomly distributed. In particular, clusters are defined as spatial regions with a high density of a specific protein of interest. These high-density regions are separated by areas with lower densities (Pageon et al., 2016). In order to further quantify the distribution of the CAZ protein ELKS in primary neuronal cultures from dSTORM acquisitions, a cluster analysis workflow based on the rendered 2D histograms was established.

4.8.6.1 ELKS dSTORM acquisition settings

Primary cortical neurons were seeded on precision coverslips in 12-well culture plates and the immunocytochemical staining was performed as described in chapter 4.6.1 (Appendix Table 14). Coverslips were mounted on depression slides filled with dSTORM buffer and sealed with Twinseal for dSTORM imaging. Overview widefield images were acquired with single band emission filters in laser widefield mode with 10% laser power for 488 nm- and 532 nm-lasers and 5% laser power for 642 nm-laser with 500 msec exposure time for each channel. dSTORM raw image sequences were acquired for the 642 nm-channel after pumping all fluorescent molecules to the dark state with 50% laser power (642 nm laser) for 30 sec. 150000 frames were acquired at 500 Hz with 30% laser power. The detection threshold for stochastically occurring blink events was set to 10 photons/pixel in the Leica acquisition software. Detected blink events in the dSTORM image sequence were fitted with a Gaussian fit. Blink events with a lateral localization less than 70 nm from the first detected event and a maximum appearance of 10 frames were merged and analyzed as one molecule localization. Molecule localization coordinates and localization precisions were used to render 2D histograms with a pixel size of 20 nm.

4.8.6.2 ELKS dSTORM cluster analysis

ELKS cluster analysis of 2D histograms was performed in Fiji (Schindelin et al., 2012). The synapsin widefield images were used to determine synaptic areas. These images were segmented by gray scale pixel values with a lower threshold of 20% of the maximum intensity of each individual image after background subtraction. The maximum intensity which determines the higher threshold of a synapse was determined in Fiji by application of the ‘Measure’ function. In previous confocal experiments it was shown that the lower threshold of 20% represents the sizes of the synaptic areas most appropriately (Julia Betzin, Ph.D. Thesis). The ‘analyze particle’ command in Fiji was used to determine synaptic areas (Figure 4.16).

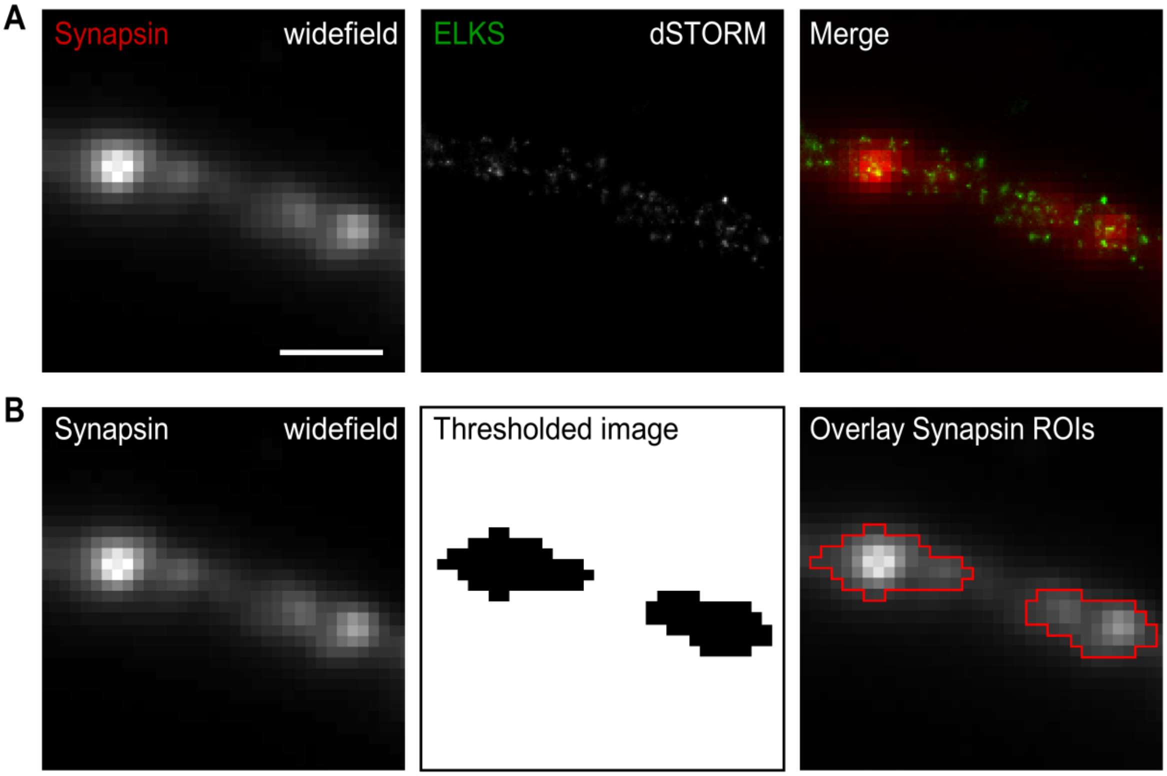

Figure 4.16: Synapse definition for dSTORM cluster analysis. (A) Primary neuronal cultures were stained with antibodies against synapsin and ELKS. Widefield images of the synapsin staining and 2D dSTORM density histograms of ELKS stainings were acquired. Scale bar: 1 µm. **(B)** The synapsin staining was used to determine synaptic areas using Fiji. A lower threshold of 20% of the maximum gray value was applied to the synapsin widefield images to determine synapsin ROIs. Synapsin ROIs (red) were superimposed on the synapsin staining.

For identification of ELKS clusters, the 2D dSTORM density histograms were imported to Fiji and all non-clustered ELKS localizations with a gray value lower than 25 were removed. The gray value threshold was determined by visual inspection of several ELKS 2D histograms after application of a range of gray scale values (data not shown). Afterwards, the 'analyze particles' command was used to determine ELKS clusters larger than 800 nm^2, which were included in the analysis (Figure 4.17).

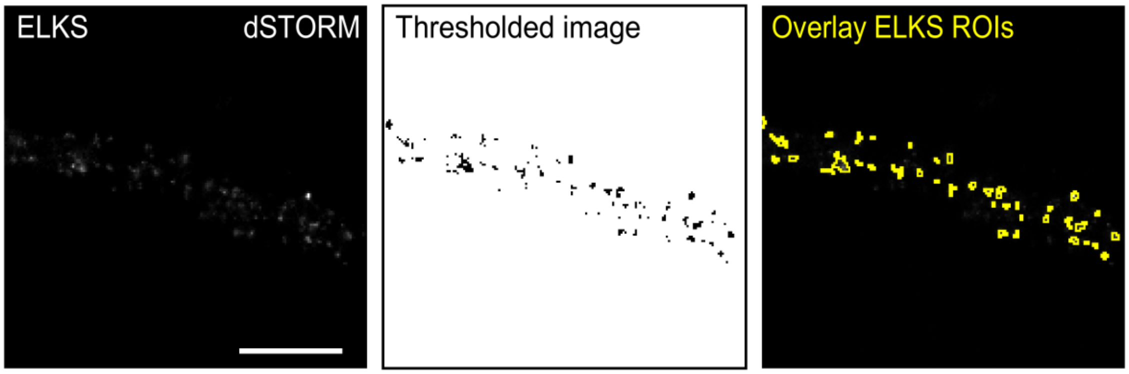

Figure 4.17: Identification of ELKS clusters in dSTORM 2D density histograms. ELKS density histograms were thresholded and clusters larger than 800 nm^2 were included in the analysis. Overlay of ELKS clusters (yellow) with the density histogram revealed the number of clusters in regard to all detected ELKS localizations.

In addition, synaptic and extrasynaptic ELKS clusters were determined by superimposing the synapsin ROIs onto the ELKS density histograms. Synaptic ELKS clusters were only those clusters which were completely contained within synapsin ROIs whereas extrasynaptic ELKS clusters had to be completely non-overlapping with the synapsin ROIs (Figure 4.18). Subsequently, the sum of gray values of the defined ELKS clusters were measured. These values correspond to the number of molecule localizations inside the clusters.

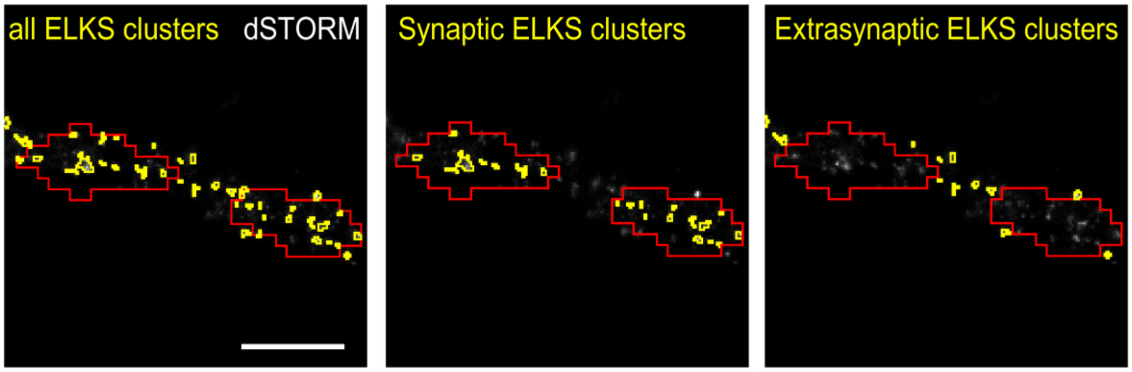

Figure 4.18: Definition of synaptic and extrasynaptic ELKS clusters. *Left:* Overlay of ELKS density histogram with defined ELKS clusters (yellow) and synaptic areas (red). *Middle:* Only ELKS clusters which were located inside the synaptic area were defined as synaptic clusters. *Right:* Extrasynaptic ELKS clusters were defined as being located completely outside the synaptic areas. Scale bar: 1 µm.

5 Results: Part A – Function of RIM4 in cerebellar circuits

The large multidomain proteins (RIM1α, RIM1β, RIM2α, RIM2β) of the RIM protein family are key components of the presynaptic active zone where they are mainly involved in the regulation of presynaptic neurotransmitter release. In contrast, the function of the small isoform RIM4 is still not well understood. Previous *in vitro* studies unveiled that RIM4 is mainly located in dendrites and axons and is not enriched at presynaptic active zones. Moreover, RIM4 seems to be involved in dendritic and axonal growth as well as synapse development and the regulation of intracellular vesicle trafficking (Alvarez-Baron et al., 2013). Interestingly, constitutive RIM4 KO 1st mice develop episodically occurring motor impairments with rapid uncontrolled movements of the hind limbs alternating with phases of complete immobility (Katrin Michel, Ph.D. Thesis).

5.1 Non-uniform distribution of RIM4 expression in murine brain tissue

Previous *in situ* hybridization studies focused mainly on the cellular distribution and functional expression of RIM4 *in vivo* in wildtype Wistar rats (Alvarez-Baron et al., 2013). To further elucidate potential functions of RIM4 *in vivo*, constitutive RIM4 KO 1st mice were generated. These mice carry a LacZ reporter gene cassette with a splice acceptor side inserted between exon 1 and 2 of the *Rims4* gene under the control of the endogenous promotor (Katrin Michel, Ph.D. Thesis, Figure 4.1 A). Previous experiments already confirmed the successful insertion of the LacZ reporter gene cassette and the splice acceptor site leading to a constitutive RIM4 KO in these mice (Katrin Michel, Ph.D. Thesis). The splice acceptor side captures the RNA transcript and a polyadenylation signal truncates the transcript so that the gene is not transcribed into mRNA downstream of the cassette site, thereby leading to the knock-out of the protein (Testa et al., 2004). The insertion of the LacZ reporter gene cassette in turn, serves as a reporter for endogenous promotor activity. Therefore, these experiments should confirm the previously published cellular expression pattern of RIM4 in the newly generated knockout-first mouse line. The β-galactosidase expression caused by the insertion of the LacZ reporter gene cassette was analyzed by X-gal staining. Hence, β-galactosidase expression should correspond to the expression of RIM4. Sagittal brain slices of constitutive RIM4 KO 1st and wildtype mice as negative controls were used. X-gal staining led to a blue precipitate in cells with β-galactosidase indicating RIM4 promotor activity. Strong X-gal staining was visible in the hippocampus, the cortex, the cerebellum and the inferior olive, a small nucleus in the lower part of the brain stem as well as in the olfactory bulb in constitutive RIM4 KO 1st mice (n = 5 mice per group; Figure 5.1 A). In the hippocampus, intense X-gal staining was detected in the pyramidal cell layer of the CA1 region. Interestingly, a diffuse labelling could be observed in the stratum radiatum, pointing towards a potential expression of RIM4 in Schaffer collateral synapses. Furthermore, a less intense staining was visible in the pyramidal cell layer of the CA3 region. In the dentate gyrus (DG) only some sparse labelling of neurons was detected (Figure 5.1 B). In the cortex the X-gal staining was detected in neurons of all layers. Especially layer VI showed an enrichment of X-gal staining and therefore RIM4 expression. Interestingly, this layer is known for its interconnection with the thalamus and the reticular thalamic nucleus (Lam and Sherman, 2010). The accompanying olfactory bulb of constitutive RIM4 KO 1st mice showed weak X-gal staining in the glomerular layer. In the cerebellum, X-gal staining was mostly accounted to Purkinje cells, the main inhibitory output cells of this brain region. In addition, also a subset of inferior olive neurons in the brain stem showed β-galactosidase expression. Previous studies showed that neurons in this brain region send their axons, namely climbing fibers, to dendrites of cerebellar Purkinje cells and are one source of input for these cells (Figure 5.1 C; De Zeeuw et al., 1998; Saab and Willis, 2003).

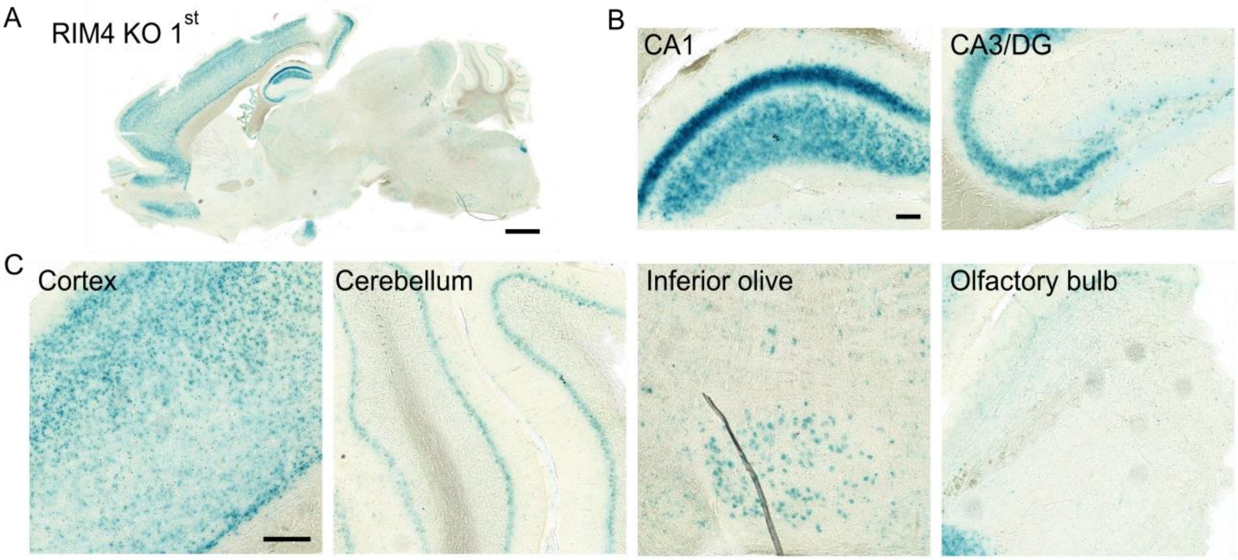

Figure 5.1: LacZ expression in constitutive RIM4 KO 1st mice reveals a non-uniform distribution of RIM4. (A) Sagittal section of a constitutive RIM4 KO 1st brain displays β-galactosidase expression in cortex, hippocampus, cerebellum and inferior olive. Some areas of the section were damaged due to the resectioning process. Scale bar: 1000 µm. **(B)** Zoom-in to the hippocampal CA1 and CA3/DG regions with high β-galactosidase expression. Scale bar: 50 µm. **(C)** Zoom-in to regions with high β-galactosidase expression in the cortex, cerebellum, inferior olive and olfactory bulb. Scale bar: 100 µm. n = 5 mice per group. In wildtype mice no X-gal staining was detected (data not shown).

In sum, regions with the highest β-galactosidase and therefore, RIM4 promotor activity were the cortex, mainly the cortical layer VI, the CA1 region of the hippocampus, the Purkinje cell layer of the cerebellum and the inferior olive in the brain stem. These results suggest a cell-type specific function of RIM4 in brain regions with the highest expression levels. Furthermore, these results are an indirect readout for the successful insertion of the splice-acceptor cassette in the *Rims4* gene, confirming previously published results (Katrin Michel, Ph.D. Thesis, Alvarez-Baron et al., 2013).

5.1.1 Cre recombinase-dependent decrease of *Rims4* gene expression in constitutive RIM4 KO mice

In a second set of mice breedings, constitutive RIM4 KO mice were generated by breeding RIM4^{floxed} mice with transgenic mice ubiquitously expressing Cre recombinase in all cells of the body. Thereby the exon 2 of the *Rims4* gene was deleted, leading in turn to an ablation of RIM4 protein expression (RIM4const KO). In contrast to the previously generated constitutive RIM4 KO 1st mice, Cre recombinase expression lead to an ablation of the *Rims4* gene in all cells expressing the enzyme, independently of the endogenous RIM4 promotor activity (chapter 4.2; Figure 4.1). The RNAscope technique was used to further analyze if the Cre recombinase-mediated excision of the 2nd exon successfully ablated the transcription of the *Rims4* gene in RIM4const KO mice. This technique is based on *in situ* hybridization (ISH) and allows to decorate probe-specific RNA transcripts with fluorescent molecules. Every single fluorescent spot corresponds to one mRNA transcript. The RNAscope labelling protocol as well as the image acquisition was carried out by Erick Martinez, AG Blaess, University Clinic Bonn. RIM4const KO mice and wildtype controls were used for this data set. In constitutive RIM4 WT mice fluorescent signals could be detected in many brain regions. However, the focus was set to brain regions which already showed high RIM4 expression in the lacZ expression experiments (chapter 5.1). Therefore, the RIM4 transcript signal was analyzed in the cortex (CX), the hippocampus (HC) and the cerebellum (CB) in constitutive RIM4 WT mice (Figure 5.2; CB: 24.97 ± 0.82 fluorescent puncta/cell, CX: 14.18 ± 0.56 fluorescent puncta/cell, HC: 6.58 ± 0.54 fluorescent puncta/cell). In contrast, RIM4 transcript signals were significantly decreased in RIM4const KO mice in the investigated brain regions (CB: 2.43 ± 0.19 signals/cell, CX: 2.80 ± 0.19 signals/cell, HC: 2.05 ± 0.20 signals/cell; n = 3 mice per group; Figure 5.2).

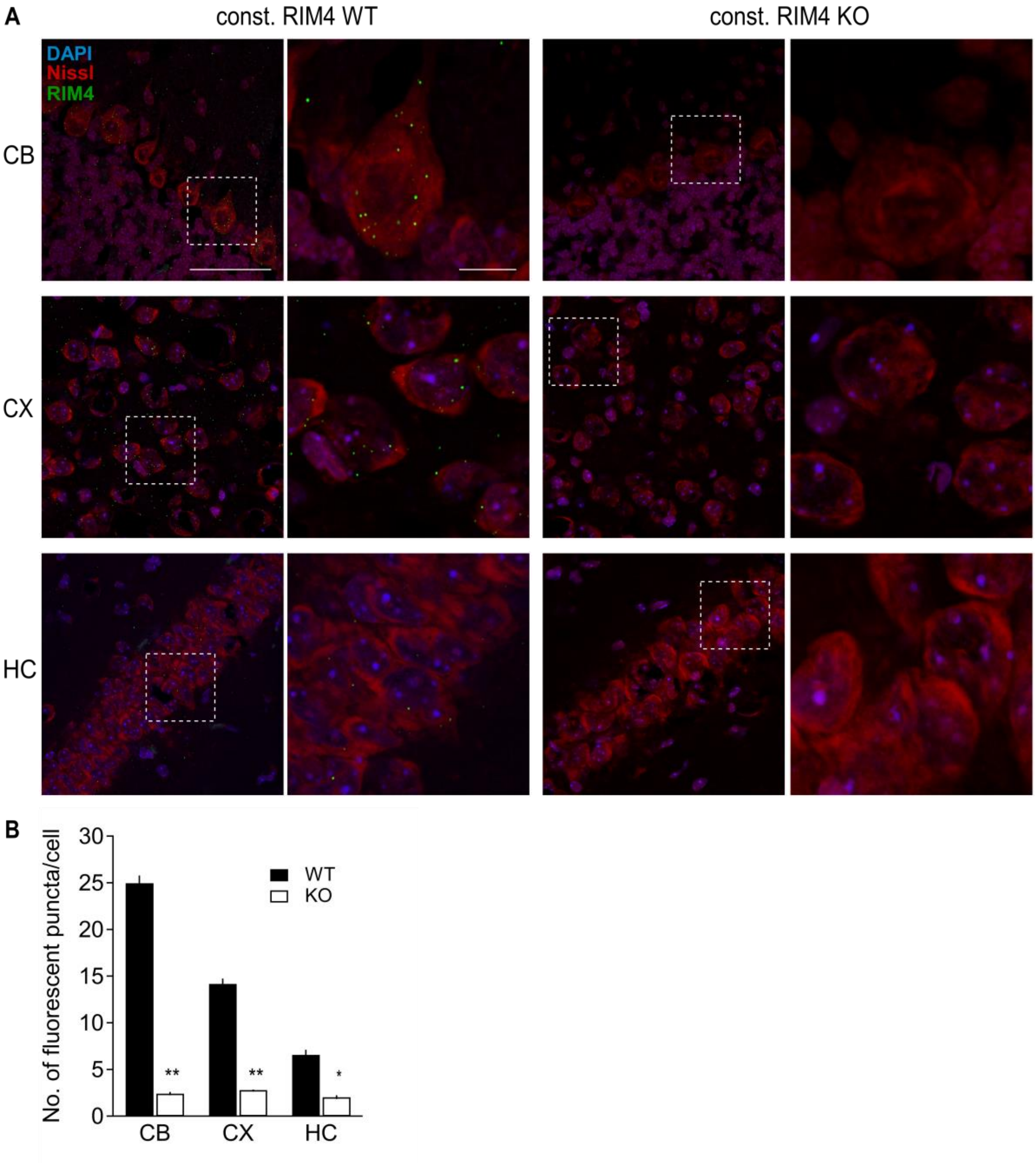

Figure 5.2: RNAscope reveals decreased *Rims4* gene expression in constitutive RIM4 KO mice. (A) RNAscope *in situ* hybridization was used to illustrate RIM4 gene expression in constitutive RIM4 WT and KO mice. *Left:* RIM4 fluorescent probes could be detected especially in cells of the hippocampus (HC), cortex (CX) and cerebellum (CB) of constitutive RIM4 WT mice. *Right:* Almost no RIM4 transcript expression could be detected in cells of the hippocampus, cortex and cerebellum of RIM4const KO mice. DAPI (blue) and Nissl (red) staining was used to visualize cells. RIM4 fluorescent probes are depicted in green (n = 3 mice per group). Scale bar: 50 µm in overview images, 10 µm in zoom-in. **(B)** Quantification of fluorescent puncta per cell in cerebellum (CB), cortex (CX) and hippocampus (HC) of WT and RIM4const KO mice. n = 3 mice per group, 150 cells per mouse and brain region were counted. Statistics: Two-way ANOVA with Holm-Sidak's post-test, * $p < 0.05$, ** $p < 0.0001$.

In sum, these results indicate that the Cre recombinase expression successfully ablated the *Rims4* transcript in RIM4const KO mice. Specifically, in brain regions with high RIM4 expression the *Rims4* transcripts were significantly reduced. Important to note is that the detected reduction in RIM4 expression in RIM4const KO mice led in turn to the occurrence of similar episodically occurring motor impairments as observed in constitutive RIM4 KO 1^{st} mice. These results further raise the question which functions RIM4 fulfills on a cellular level, specifically in brain regions with high RIM4 expression levels, for example in the cortex or the cerebellum.

5.2 RIM4 expression levels are regulated by neuronal activity

Previous studies showed that proteins of the presynaptic release apparatus respond to changes in global network activity with homeostatic adaptation. Expression levels of presynaptic proteins were mainly downregulated upon synaptic silencing (Lazarevic et al., 2011; Schanzenbächer et al., 2016). To investigate if RIM4 is expressed in the brain on constant levels or if its expression might be regulated by neuronal activity, primary cortical neurons from WT mice were incubated with tetrodotoxin (TTX; 1 µM) or gabazine (10 µM). Cells were harvested at different timepoints after the application of TTX or gabazine and quantitative real-time RT-PCR was performed to determine relative *Rims4* mRNA expression levels (Figure 5.3). *Rims1*α was chosen as a control of synaptic scaling effects. Lazarevic et al., 2011 described a downregulation of RIM1/2 expression levels by prolonged neuronal silencing. Blocking excitatory neuronal activity by application of TTX resulted in a decrease of *Rims1*α gene expression whereas *Rims4* mRNA levels were increased and peaked significantly 24h after application of TTX (24h TTX: 228.99 ± 121.19%). In contrast, blocking inhibitory neuronal activity using gabazine did not affect *Rims1*α expression levels. However, *Rims4* expression tended to increase 48h after addition of gabazine without statistical significance (48h gabazine: 139.09 ± 12.14%). In conclusion, *Rims1*α and *Rims4* transcripts were differently regulated upon changes in excitatory and inhibitory network activity. These results point towards diverging roles in global network activity of RIM4 compared to large RIM isoforms, for instance RIM1α.

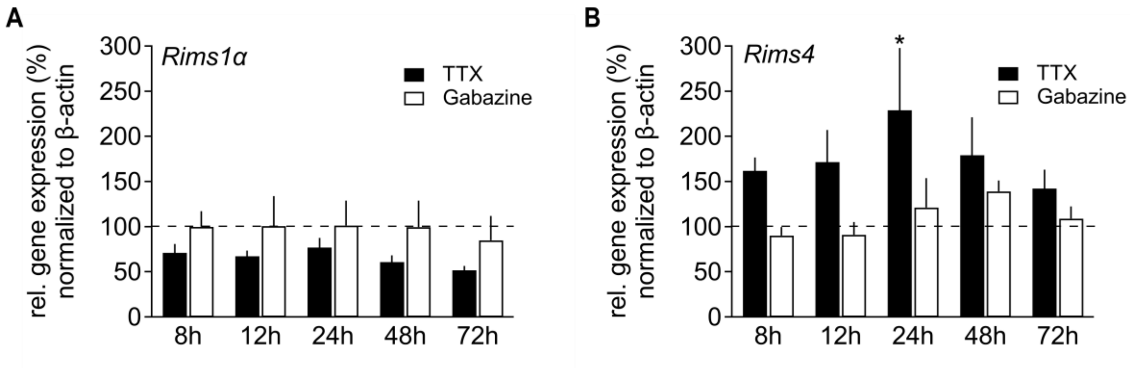

Figure 5.3: Neuronal *Rims4* gene expression levels increase after 24h incubation with TTX. Gene expression levels of *Rims1α* **(A)** and *Rims4* **(B)** 8h, 12h, 24h, 48h and 72h after application of TTX (1 µM) or gabazine (10 µM) in primary cortical neurons. Data represented as mean ± SEM. n = 3 independent cultures per group. Significance: Two-way ANOVA with Tukey's post-test, * $p < 0.05$.

5.3 No major changes in the transcriptome and proteome in the cerebellum and cortex of constitutive RIM4 knock-out mice

Since the large RIM isoforms, RIM1 and RIM2, are key proteins of the presynaptic CAZ, a similar function of RIM4 could be conceivable. To investigate if the ablation of RIM4 has an influence on the expression levels of other isoforms of the RIM protein family or of other proteins of the pre- and postsynapse, transcript and protein levels in cortical and cerebellar tissue of constitutive RIM4 KO 1st mice and WT controls were analyzed. The analysis of RIM isoform mRNA transcripts was performed with quantitative real-time RT-PCR. As anticipated, only the relative expression levels of *Rims*4 mRNA transcripts were significantly reduced in cerebellum and cortex of constitutive RIM4 KO 1st mice compared to WT levels (cortex: 25.94 ± 3.41 %; cerebellum: 10.69 ± 0.5 %; n = 5 mice per group). No significant changes in relative gene expression levels of other RIM isoforms could be detected (Figure 5.4).

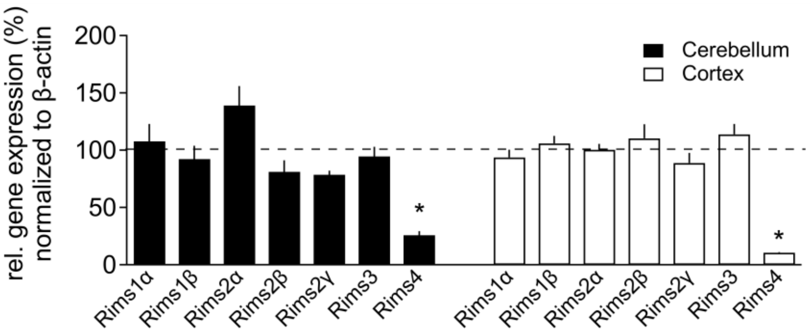

Figure 5.4: *Rims4* gene expression is decreased in constitutive RIM4 KO 1st mice. Quantitative real-time RT-PCR of constitutive RIM4 KO 1st mice normalized to WT levels unveiled a decreased *Rims4* transcript expression in cerebellum (filled bars) and cortex tissue (open bars). In contrast, the gene transcript levels of all other isoforms of the RIM family were similar to WT levels (n = 4 mice per group). Data shown as mean ± SEM. Significance: Two-way ANOVA with Holm-Sidak's post-test, * $p < 0.001$.

Synaptic protein levels were evaluated with quantitative immunoblot analysis of homogenates from cerebellar tissue of constitutive RIM4 KO 1st mice and WT controls. Also in this case, only the relative protein expression of RIM4 was reduced in constitutive RIM4 KO 1st mice whereas the expression of the other investigated proteins remained unchanged (RIM4: 9.27 ± 3.41 %; n = 5 mice per group; Figure 5.5).

In conclusion, the deletion of RIM4 in cortical and cerebellar tissue of constitutive RIM4 KO 1st mice does neither influence the transcriptional levels of other RIM isoforms nor the expression of other synaptic proteins.

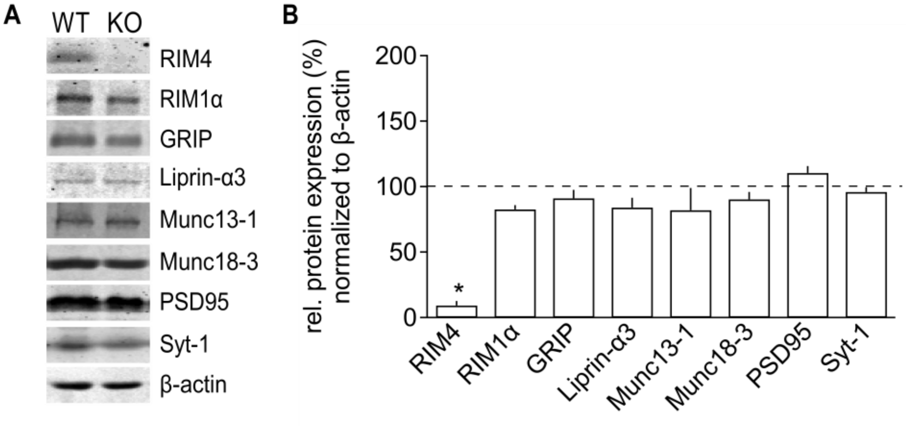

Figure 5.5: RIM4 protein expression was decreased in cerebellar tissue of constitutive RIM4 KO 1st mice. (A) Exemplary immunoblots of cerebellar tissue showed a reduction in RIM4 protein expression in constitutive RIM4 KO 1st mice. **(B)** Quantification of immunoblots normalized to WT levels (n = 5 mice per group). Data shown as mean ± SEM. Significance: Two-way ANOVA with Holm-Sidak's post test, * $p < 0.0001$.

In a next step transcriptomic and proteomic analyses of cortical and cerebellar tissue by RNAseq and mass spectrometry were performed to further identify potential genes or pathways that are influenced by RIM4 or are involved in its function. All omics approaches were carried out by the AG Schultze, LIMES Institute, University Bonn, the Next Generation Sequencing Core Facility, University Bonn, the Mass Spectrometry Core Facility, University Bonn and the Bioinformatic Core Facility, University Bonn.

Cortical and cerebellar tissue from constitutive RIM4 KO mice and WT controls were used for the analyses since previously performed experiments suggested a high RIM4 expression in these two brain regions (see Methods section for details; chapter 5.1, Katrin Michel, Ph.D. thesis). In a first step, principal component analysis (PCA) was used to display the variation between samples of the different data sets. In general, PCA transforms the high-dimensional omics data sets into low-dimensional projections which contain a smaller number of variables called principal components (PC). The PCs can be then plotted to represent the grouping of the samples in the different data sets. The first principal component (PC1) defines the highest possible variance in the data and the second principal component (PC2) the second highest possible variance (Gerst and Hölzer, 2018). Here, the PCA plots were used to visualize the quality of the biological replicates regarding similar gene and protein expression patterns (Figure 5.6.). The four investigated data sets of tissue from constitutive RIM4 WT and KO mice showed remarkably similar gene and protein expression among biological replicates. The gene and protein expression profiles of the constitutive RIM4 KO and WT samples in the cerebellar transcriptomics and proteomics data sets appeared more widespread compared to cortical samples of WT and KO mice, indicating more gene expression variability in the cerebellar data sets (Figure 5.6 A, B). Interestingly, both transcriptomics data sets contained one outlier in the constitutive RIM4 KO samples (Figure 5.6 A, C). Whereas, the transcriptomic and proteomic data sets of cortical tissue showed a more homogenous protein expression (Figure 5.6 C, D).

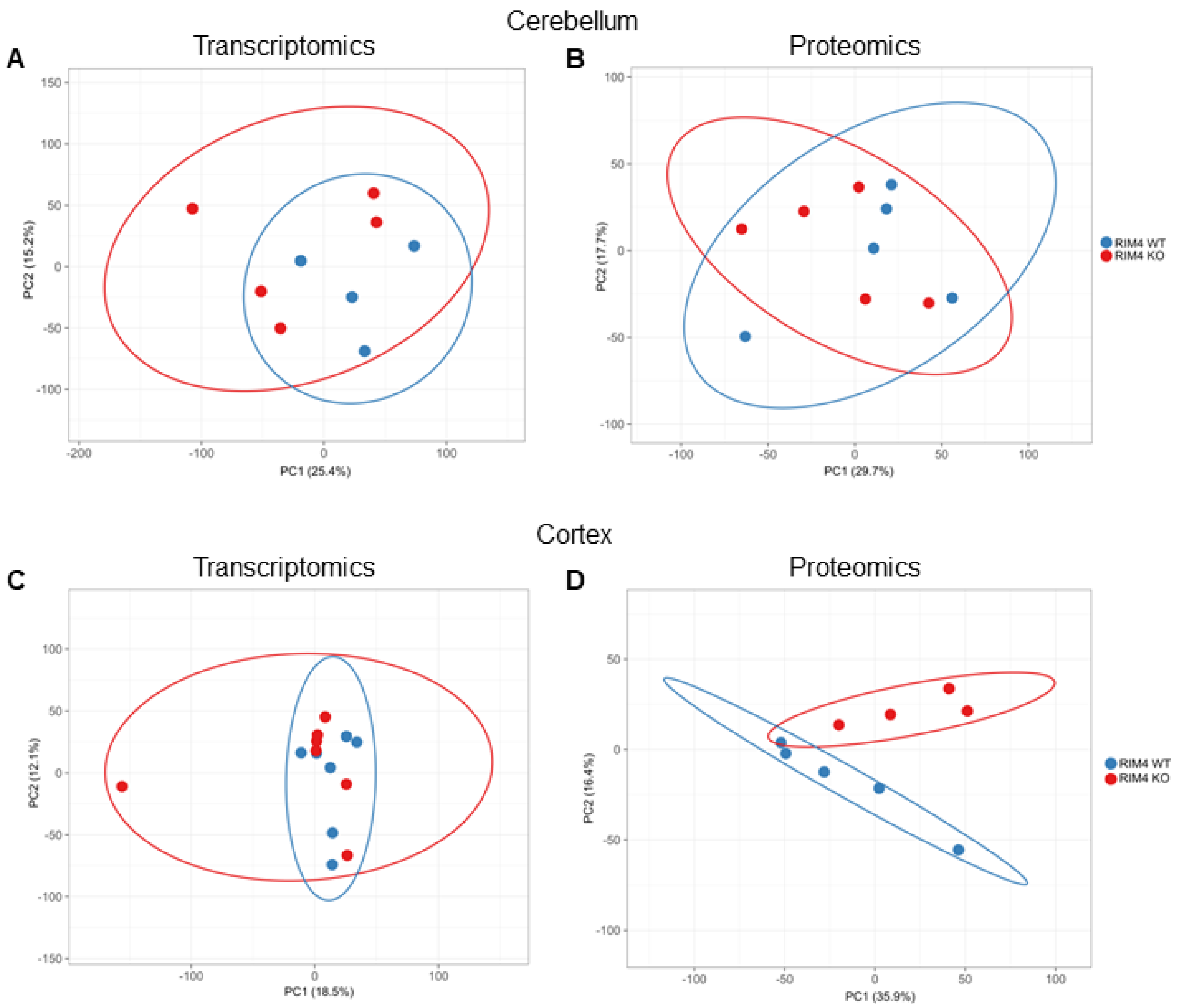

Figure 5.6: Principal component analysis unveils variability in cerebellar and cortical gene expression profiles. Principal component analysis was performed to visualize potential variability among biological replicates in the four different data sets. **(A)** PCA of cerebellar transcriptomics data. **(B)** PCA of cerebellar proteomics data. **(C)** PCA of cortical transcriptomics data. **(D)** PCA of cortical proteomics data. Blue dots and circles indicate RIM4 WT samples, red dots and circles indicate RIM4 KO samples. Two constitutive RIM4 outlier samples, shown in **(A)** and **(C)** respectively were removed for all further analyses.

The expression levels of genes and proteins in constitutive RIM4 KO samples were compared to the respective WT level. Genes and proteins were defined as significantly regulated by showing a $\log_2$ fold change (FC) > 1 as well as a -log10 (p-value) > 1.3. Surprisingly, the transcriptomics data set of cerebellar tissue did not show any significantly regulated genes with except of *Rims4*. In the cortical transcriptomics data, two other genes apart from *Rims4* were differentially regulated. In the proteomics data sets the downregulation of the RIM4 protein could not be detected. All other proteins were not significantly regulated suggesting no major changes in gene and protein composition in cortical and cerebellar tissue of constitutive RIM4 KO mice. The distribution of the differentially regulated genes and proteins of cerebellar and cortical tissue was displayed by Volcano plots (Figure 5.7).

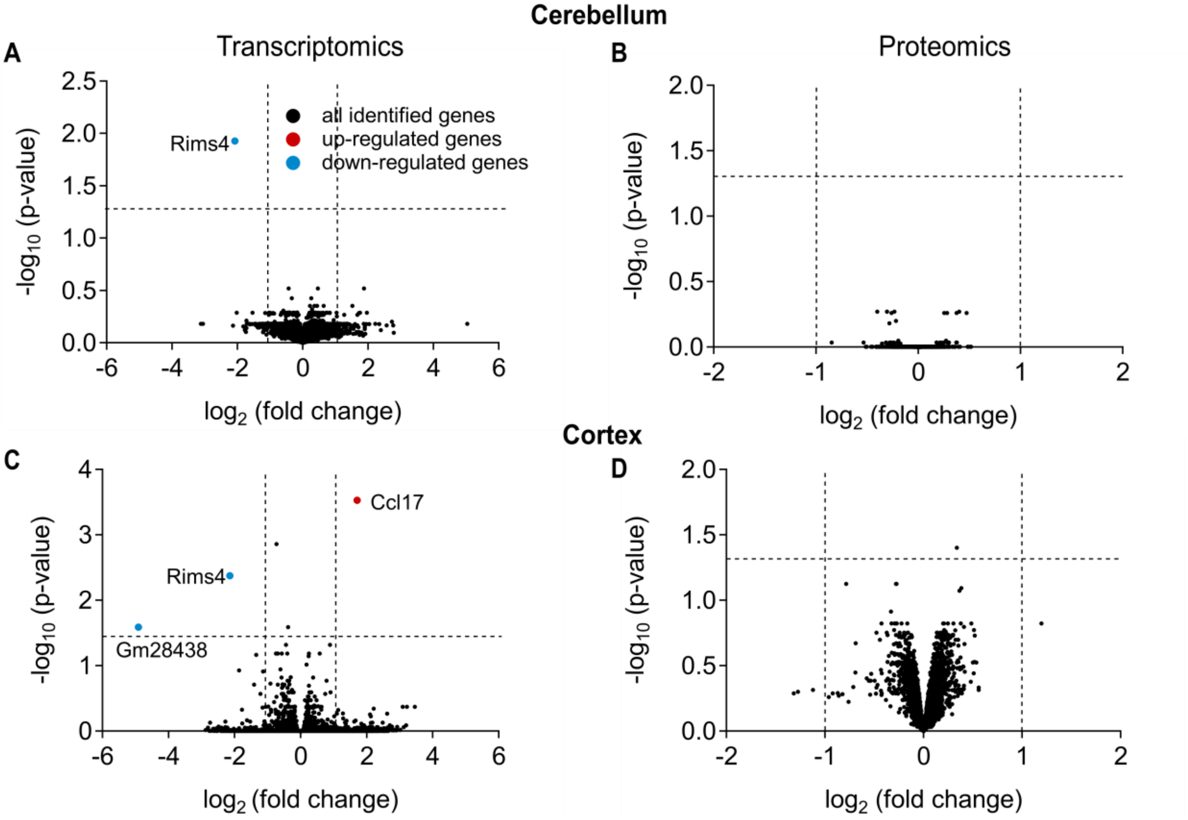

Figure 5.7: Volcano plots of differentially regulated genes and proteins in cerebellar and cortical tissue upon ablation of RIM4. (A) Identified genes of transcriptomics analysis of cerebellar tissue. **(B)** Proteomics analysis of cerebellar tissue. **(C)** Identified genes in transcriptomic analysis of cortical tissue. **(D)** Proteomics analysis of cortical tissue. The gray dots represent all identified genes and proteins, upregulated genes and proteins are depicted in red and blue dots represent downregulated genes and proteins. Dotted lines represent the thresholds for fold change of 2 ($\log_2$ (FC) = 1) on the x-axis and and the p-value of 0.05 (-log10 (p-value) = 1.3) on the y-axis. Genes and proteins were defined as differentially regulated with a $\log_2$ (fold change) > 1 and a -log10 (p-value) > 1.3.

In the transcriptomic analysis of cerebellar tissue 12962 genes were identified. However, only the *Rims4* gene itself was identified as being significantly downregulated after genetic ablation of RIM4 in constitutive RIM4 KO mice. Furthermore, in the proteomic analysis 5595 different proteins could be detected in cerebellar tissue. None of them was significantly up- or downregulated in constitutive RIM4 KO mice. Similar results were obtained for the cortical tissue. The transcriptomic analysis revealed in total 25444 genes out of which *Ccl17* was upregulated and *Gm28438* as well as *Rims4* were downregulated. On the protein level, 4481 different proteins were identified without any differentially regulation (Table 3, Table 4).

Table 3: Overview of identified genes and proteins in 4 different omics-approaches.

		All identified genes/ proteins	**Upregulated genes/proteins**	**Downregulated genes/proteins**
Cerebellum	Transcriptomics	12962	0	1
	Proteomics	5595	0	0
Cortex	Transcriptomics	25444	1	2
	Proteomics	4481	0	0

Table 4: Differentially regulated genes in constitutive RIM4 KO mice.

		Differentially regulated genes	**$\log_2$ FC**	**$-\log_{10}$ p-value**
Cerebellum	Transcriptomics	*Rims4*	-2.083	1.929
	Proteomics	-	-	-
Cortex	Transcriptomics	*Ccl17*	1.710	3.527
		Gm28438	-4.915	1.590
		Rims4	-2.143	2.376
	Proteomics	-	-	-

Interestingly, database research revealed that the gene *Ccl17* codes for the C-C motif chemokine ligand 17 which is produced in the thymus and is involved in the immune response. The second differentially regulated gene Gm28438 is an unprocessed pseudogene, located on chromosome 1 and is expressed in several different tissues. Among others in the nervous, the cardiovascular and the musculoskeletal system (source: Mouse Genome Informatics (MGI); Table 5).

Table 5: Functions of differentially regulated genes apart from *Rims4*.

Differentially regulated gene	**Protein name**	**Protein function**
Ccl17	C-C motif chemokine ligand 17	Chemokine produced in thymus, induces together with CCL22 chemotaxis of T-helper cells (Scheu et al., 2017)
Gm28438	Unprocessed pseudogene	-

In conclusion, the analysis of the cerebellar and cortical transcriptomics data sets showed no major changes of gene regulation after ablation of RIM4. Downregulation of *Rims4* gene expression could be verified in both transcriptomics data sets. In cerebellar and cortical proteomics data sets, neither the downregulation of RIM4 nor any other differentially regulated protein could be identified. Furthermore, the constitutive RIM4 KO samples showed higher variations among biological replicates in gene and protein expression patterns compared to WT samples pointing towards a potential influence of RIM4 itself or the presence of the motor impairments in constitutive RIM4 KO mice in the detected expression patterns.

5.4 RIM4 ablation does not influence mGluR1- and KCND3-abundance in cerebellar Purkinje cells

Several studies describe mice with ataxic symptoms comparable to the observed motor impairments of RIM4const KO mice as a result of alterations in ion channels or receptors (reviewed in Hoxha et al., 2018). Interestingly, the previously mentioned omics data did not point to any channel- or receptor-related changes after ablation of RIM4. However, it could still be possible that not the expression level itself, but the cellular localization of ion channels or receptors is changed in these mice. To further identify potential localization-related changes, a closer look was taken on the cerebellar Purkinje cell layer, a brain region with high RIM4 expression levels where largest localization-related changes in ion channels or receptors would be expected. Previously published studies identified metabotropic glutamate receptors (mGluR1) being highly expressed in cerebellar Purkinje cells with a crucial function in long-term depression (LTD; reviewed in Kano and Watanabe, 2017). Furthermore mice lacking mGluR1 expression show ataxic gait and climbing fiber synapse elimination (reviewed in Hoxha et al., 2018; Kano et al., 1997).

Immunohistochemical stainings were performed with an antibody against mGluR1 in sagittal cerebellar vermis slices of constitutive RIM4 WT and KO mice (RIM4const KO/WT; n = 3 mice per group; Appendix Table 10; Figure 5.8 A). DAPI staining was used to identify cerebellar layers. Since mGluR1 receptors are mainly located at postsynaptic sites, confocal images were acquired from the molecular layer of cerebellar slices where the postsynapses of Purkinje cells are located. Mean grey values of fluorescence intensities were quantified from these regions in RIM4const KO and WT mice. No significant differences between mean grey values of fluorescence intensities of both groups could be detected (Figure 5.8 B).

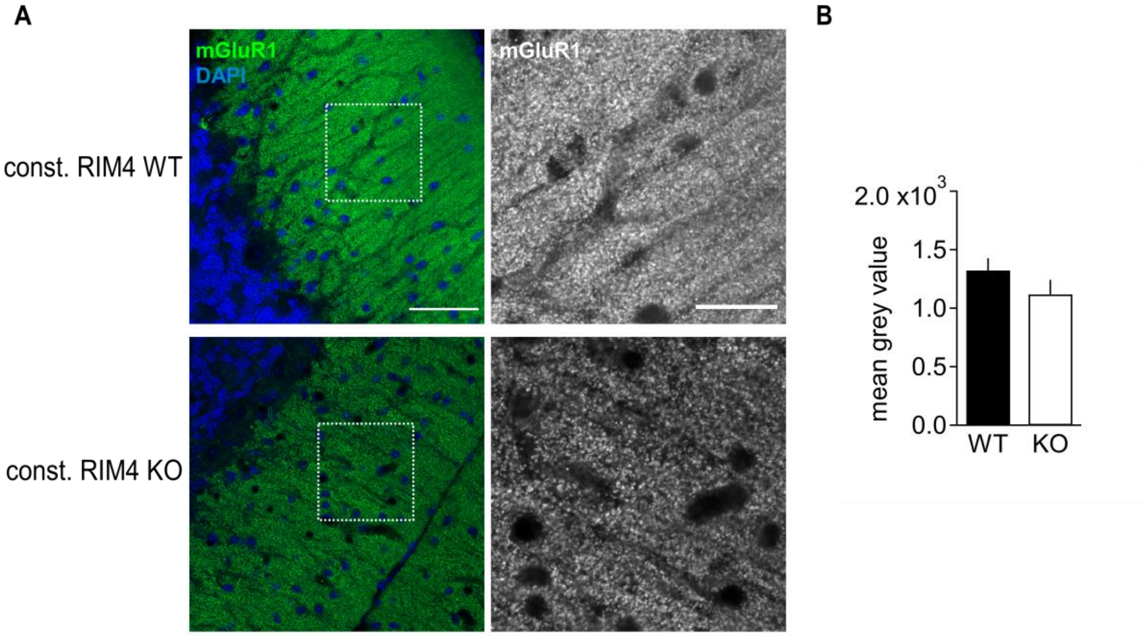

Figure 5.8: No significant changes in mGluR1 expression in dendrites of cerebellar Purkinje cells of constitutive RIM4 KO mice. (A) Example images of mGluR1 staining in sagittal cerebellar vermis slices of constitutive RIM4 WT and KO mice (*left:* overview with quantified ROI; *right:* mGluR1 fluorescence intensity in the quantified ROIs). DAPI staining was used to identify cerebellar layers (blue). Scale bar left: 50 µm, scale bar right: 10 µm. **(B)** Quantification of mGluR1 mean grey values of fluorescence intensities in the molecular layer of the cerebellar vermis in constitutive RIM4 WT and KO mice. Fluorescence intensities were background corrected. n = 3 mice per group. Data presented as mean ± SEM. Significance: Unpaired Student's t-test, p = 0.260.

Earlier studies suggested that mutations in the voltage-gated potassium channel KCND3 ($K_v4.3$) are involved in the generation of spinocerebellar ataxia in humans (Lee et al., 2012; Smets et al., 2015). Therefore, we hypothesized that the localization of this channel could be influenced by RIM4.

In order to investigate potential alterations of KCND3 expression in RIM4const KO and WT mice (n = 3 mice per group), sagittal cerebellar vermis slices were stained against the voltage-gated potassium channel as well as the cellular protein calbindin to identify cerebellar Purkinje cells (Appendix Table 10; Figure 5.9 A). DAPI was used to stain cellular nuclei. KCND3 has been shown to be mainly expressed at the dendrites of Purkinje cells (reviewed in Hoxha et al., 2018). Therefore, dendritic areas were used for quantification of mean gray values of fluorescence intensities. Interestingly, an increase in mean gray value fluorescence intensity could be detected in cerebellar slices of RIM4const KO mice without reaching statistical significance (Figure 5.9 B).

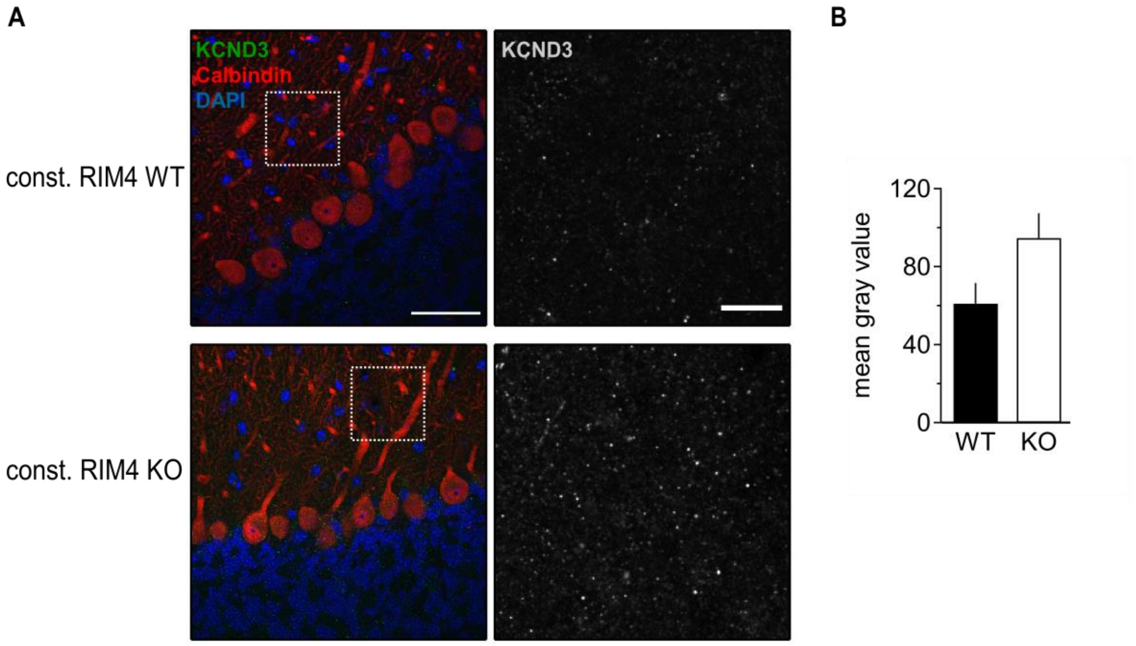

Figure 5.9: No significant changes in KCND3 expression in dendrites of cerebellar Purkinje cells of constitutive RIM4 KO mice. (A) Example images of KCND3 immunohistochemical stainings in sagittal cerebellar vermis slices of constitutive RIM4 WT and KO mice (*left:* overview with quantified ROI; *right:* KCND3 fluorescence intensity in the quantified ROIs). Merged images include calbindin staining (red) for Purkinje cell identification and DAPI (blue) for cellular nuclei staining (KCND3 staining in green). **(B)** Quantification of KCND3 mean grey values of fluorescence intensities in the molecular layer of the cerebellar vermis in constitutive RIM4 WT and KO mice. Fluorescence intensities were background corrected. n = 3 mice per group. Data presented as mean ± SEM. Significance: Unpaired Student's t-test, $p = 0.245$. Scale bar merged images: 50 µm, quantified ROIs: 20 µm.

In conclusion, the deletion of RIM4 did not influence the expression and localization of mGluR1 and KCND3 channels in cerebellar Purkinje cells. However, a trend towards a reduced mGluR1 and an increased KCND3 expression was visible, not reaching statistical significance. Together with the previously shown results of the omics data sets, these results do not confirm the hypothesis that RIM4 could play a role correct localization or trafficking of mGluR1 and KCND3 channels in cerebellar Purkinje cells.

5.5 Selective RIM4 knock-out in cerebellar Purkinje cells

Previous studies pointed towards a high RIM4 expression in cerebellar Purkinje cells and constitutive RIM4 KO mice develop episodically occurring motor impairments that point towards an important role of RIM4 in the cerebellum. In addition, many mouse models with similar motor-related phenotypes have been published that show alterations in cerebellar Purkinje cells and cerebellar morphology (Hoxha et al., 2018; Tara et al., 2018). To specifically investigate the potential cerebellar cell type-specific function of RIM4, Purkinje cell-specific RIM4 KO mice (Pcp2$_{M}$-Cre$_{tg}$:RIM4$^{fl/fl}$) were generated.

5.5.1 Generation of Purkinje cell-specific RIM4 knock-out mice

Purkinje cell-specific RIM4 KO mice were generated by crossing RIM4$^{fl/fl}$ mice with mice expressing Cre recombinase under the Purkinje cell protein 2 (Pcp2)-promotor that is restricted to cerebellar Purkinje cells (Figure 5.10 A; chapter 4.2). According to Luo et al., 2020 the conditional Cre-driver mouse line B6.129-Tg(Pcp2-cre)2Mpin/J, also known as L7Cre-2 line (Barski et al., 2000), obtains a 14-84% probability of germline recombination, depending on the exact targeting gene locus if the male mouse carries the Cre recombinase. In order to prevent germline recombination in the newly generated Pcp2$_{Mpin}$-Cre$_{tg}$:RIM4$^{fl/fl}$ mice, male RIM4$^{fl/fl}$ mice without Cre recombinase expression were mated with heterozygous Pcp2$_{Mpin}$-Cre$_{tg}$:RIM4$^{fl/+}$ mice. In turn, 50% of the offspring of these breedings would express the Cre recombinase under the Pcp2-promotor. Thereby leading to a Purkinje cell-specific RIM4 KO in these mice. Homozygous offspring of breedings from male RIM4$^{fl/fl}$ and female Pcp2$_{Mpin}$-Cre$_{tg}$:RIM4$^{fl/+}$ were used for all experiments mentioned below (Pcp2$_{M}$-Cre$_{tg}$:RIM4$^{fl/fl}$). In order to prove the restricted Cre recombinase expression in Purkinje cells, the Pcp2$_{M}$-Cre$_{tg}$:RIM4$^{fl/+}$ and Pcp2$_{M}$-Cre$_{tg}$:RIM4$^{+/+}$ mice were crossed with tdTomato-reporter mice (Figure 5.10 B). This allowed the visualization of specific Cre recombinase expression in cerebellar Purkinje cells by the red-fluorescent reporter protein tdTomato.

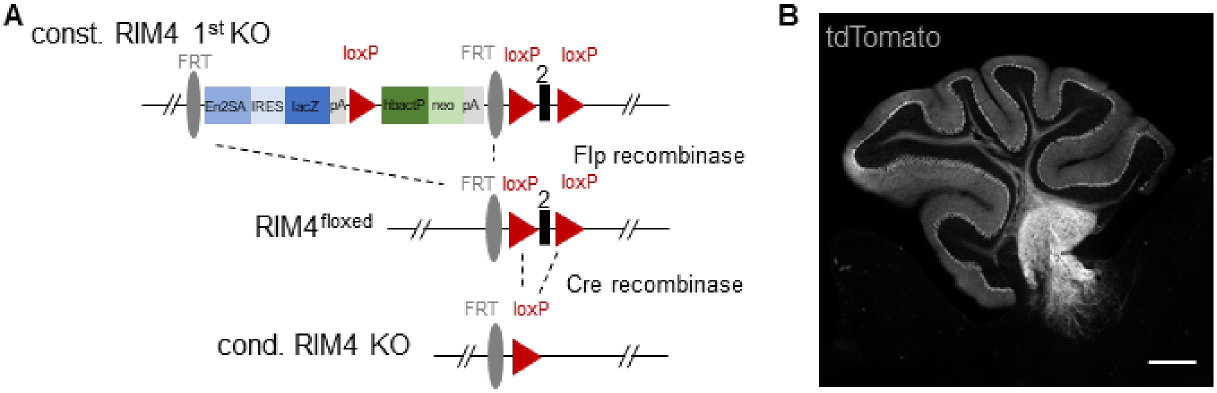

Figure 5.10: Generation of Purkinje cell-specific RIM4 KO mice. (A) Flp-mediated recombination leads to the excision of the splice acceptor cassette and normal RIM4 protein expression (RIM4$^{fl/fl}$). Pcp2-Cre recombinase-mediated recombination results in the excision of exon 2 and disruption of RIM4 protein expression (Pcp2$_{M}$-Cre$_{tg}$:RIM4$^{fl/fl}$) specifically in cerebellar Purkinje cells. **(B)** Pcp2-Cre expressing mice were bred with tdTomato reporter mice to verify specific Cre recombinase expression in cerebellar Purkinje cells. Scale bar: 100µm.

5.5.2 Purkinje cell-specific RIM4 knock-out mice phenocopy the episodically occurring motor impairments of constitutive RIM4 knock-out mice

The most interesting question to answer with this newly generated mouse line was if the Purkinje cell-specific ablation of RIM4 would be sufficient to induce similar episodically occurring motor impairments as observed in the constitutive RIM4 KO 1st mice (Katrin Michel, Ph.D. Thesis). In the first 3 weeks after birth, the Pcp2$_{Mpin}$-Cre$_{tg}$:RIM4$^{fl/fl}$ mice gained weight in the same range as their WT and heterozygous littermates. From the 3rd week after birth onwards, the KO mice gained less weight and throughout their life they stayed smaller compared to their WT and heterozygous littermates (Figure 5.11). The weight loss and the lower increase in weight over time was similarly described for the constitutive RIM4 KO 1st mice (Katrin Michel, Ph.D. Thesis).

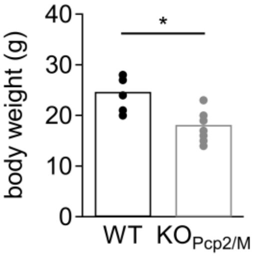

Figure 5.11: Reduced body weight of adult Pcp2$_{Mpin}$-Cre$_{tg}$:RIM4$^{fl/fl}$ mice. Body weights of adult Pcp2$_{Mpin}$-Cre$_{tg}$:RIM4$^{fl/fl}$ (KO$_{Pcp2/M}$) were reduced compared to Pcp2$_{Mpin}$-Cre$_{tg}$:RIM4$^{+/+}$ (WT) littermates. Each dot represents the body weight of one mouse 10-20 weeks old. N = 6 WT and 7 KO mice. Unpaired Student's t-test, p = 0.0033.

At the same time when the Pcp2$_{\text{Mpin}}$-Cre$_{\text{tg}}$:RIM4$^{\text{fl/fl}}$ mice stopped gaining weight, they developed episodically occurring motor impairments, similar to constitutive RIM4 KO mice. In the early stage of the motor impairments, the mice showed rapid, uncontrolled movements of the hindlimbs sometimes also the forelimbs were affected. The mice were not able to walk straight and fell over. These symptoms appeared together with intensive movements of the tail. This early ataxia-related stage of the motor impairments lasted up to 30 min. In the later stage of the episodic motor impairments the general movement of the mice was reduced, and the animals appeared paralyzed and completely immobile. The hind limbs were completely outstretched during this period. The mice stayed up to 6h in this dystonia-related stage until they behaved normal again (Figure 5.12). In conclusion, Pcp2$_{\text{Mpin}}$-Cre$_{\text{tg}}$:RIM4$^{\text{fl/fl}}$ mice phenocopy the episodically occurring motor impairments of constitutive RIM4 KO 1st mice which already points towards a specific function of RIM4 in cerebellar Purkinje cells.

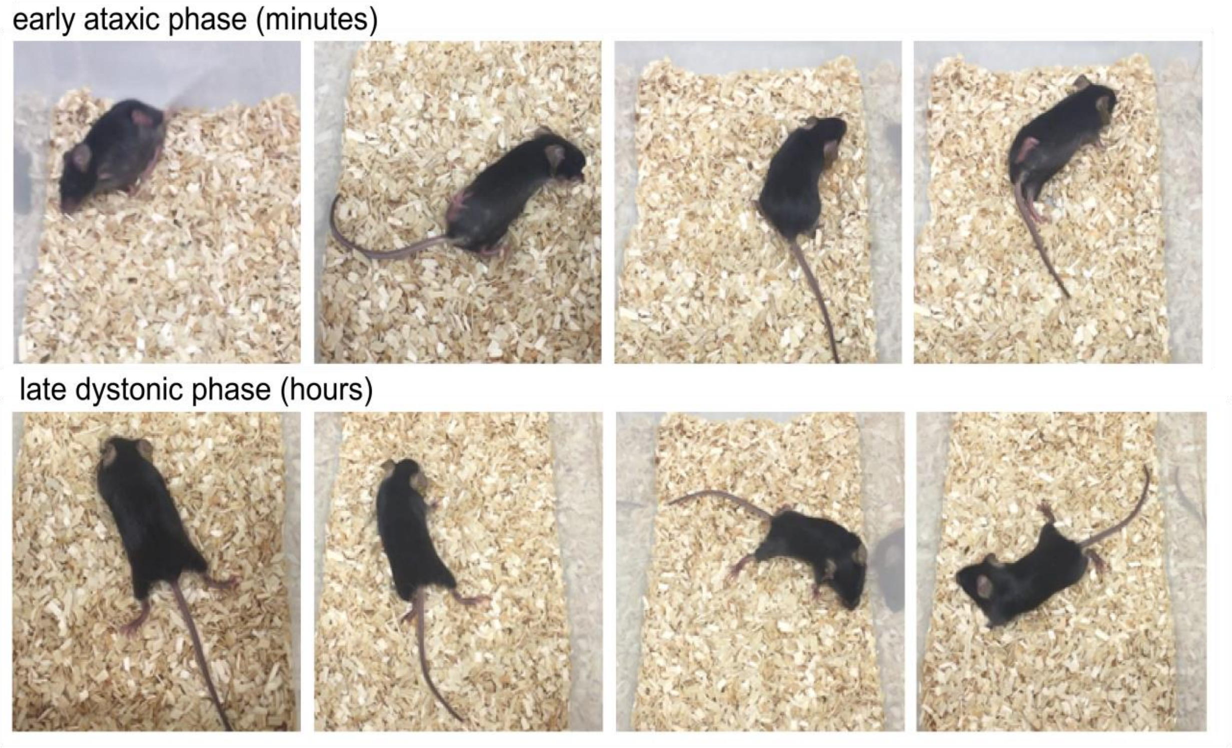

Figure 5.12: Pcp2$_{\text{Mpin}}$-Cre$_{\text{tg}}$:RIM4$^{\text{fl/fl}}$ mice phenocopy the episodically occurring motor impairments of constitutive RIM4 KO mice. *Upper row:* Early ataxic phase of the episodically occurring motor impairments in a Pcp2$_{\text{Mpin}}$-Cre$_{\text{tg}}$:RIM4$^{\text{fl/fl}}$ which lasted up to 30 min. The animal showed rapid uncontrolled movements of the hindlimbs and was not able to walk straight. *Lower row:* Late dystonic stage of the motor impairments lasting several hours in the same Pcp2$_{\text{Mpin}}$-Cre$_{\text{tg}}$:RIM4$^{\text{fl/fl}}$ as shown in the upper row. The animal showed in general a reduced movement, appeared paralyzed and completely immobile.

5.5.3 Purkinje cell-specific RIM4 knock-out leads to an altered cerebellar network activity *in vivo*

By generation of Purkinje cell-specific RIM4 KO mice that phenocopy the constitutive RIM4 KO mice, a predominant role of RIM4 in generation of episodically occurring motor impairments could be ascribed to cerebellar Purkinje cells. Nevertheless, how exactly RIM4 is involved in cellular mechanisms and which specific alterations lead to the occurrence of these episodic motor impairments still needs further investigations. For this reason, single-unit recordings were performed in the cerebellar vermis of awake, freely moving Pcp2$_{\text{Mpin}}$-Cre$_{\text{tg}}$:RIM4$^{\text{fl/fl}}$ mice and Pcp2$_{\text{Mpin}}$-Cre$_{\text{tg}}$:RIM4$^{+/+}$ mice as WT controls. Microdrives with four movable tetrodes were implanted and recordings were started one week after the surgery. During the recording sessions, tetrodes were moved in 30-50 µm steps into the tissue until a signal appeared. Subsequently, tetrodes were left at that position for around 24h prior recording to establish a stable single unit firing (Figure 5.13). The recording depths were noted to identify recording positions after perfusion and histology of the mice.

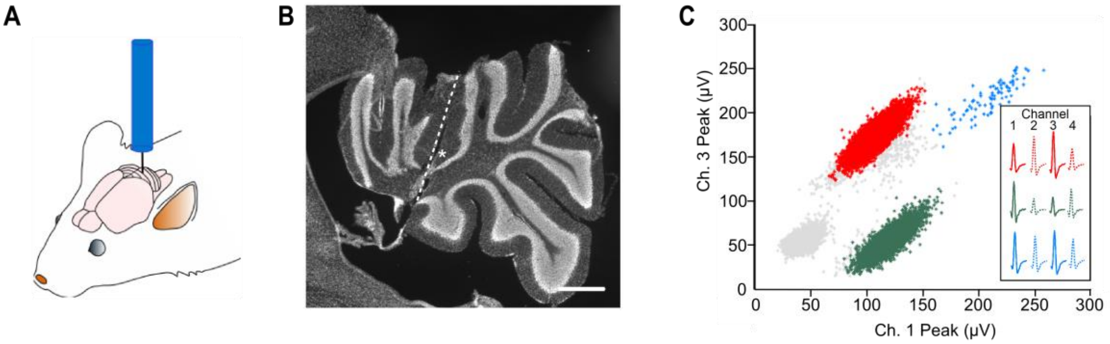

Figure 5.13: Cerebellar single-unit recordings in Pcp2$_{\text{Mpin}}$-Cre$_{\text{tg}}$:RIM4$^{\text{fl/fl}}$ mice. (A) Single unit tetrode recordings were performed in the cerebellar vermis in awake, freely moving mice (Adapted from Arancillo et al., 2015). **(B)** Sagittal section of the cerebellar vermis area with a tetrode tract in Purkinje- and granule cell layers (dashed line). The tetrode positions for the single unit recording shown in (C) is indicated by an asterisk. Drive extraction after the perfusion of the mouse resulted in gross tissue damage in the upper cerebellar layers. Scale bar: 500 µm. **(C)** Scatterplot of single unit spike amplitudes on two of the four recording channels (ch.1 and ch.3). Spikes from the same cell are color-coded. Insets show the average waveforms of three manually isolated cells on all four channels. Channels shown in the scatterplot are depicted in solid lines, others in dashed lines. Noise spikes are shown in grey.

Only recordings acquired in the molecular, Purkinje cell or granule cell layer of the cerebellum were used for analysis. However, the identification and separation of Purkinje cell waveforms from other cerebellar cell types by appearance of complex spikes was not successful (data not shown). Baseline single unit recordings were acquired for 10 min. The mean firing frequency of single units was not significantly changed in Pcp2$_{\mathrm{Mpin}}$-Cre$_{\mathrm{tg}}$:RIM4$^{\mathrm{fl/fl}}$ mice. However, a larger scatter of datapoints could be detected (WT: 28.51 ± 4.56 Hz; KO$_{\mathrm{Pcp2/M}}$: 41.55 ± 4.48 Hz; Figure 5.14 A,B), Furthermore, the coefficient of variation (CoV) of interspike intervals (ISIs) was not altered between WT and Pcp2$_{\mathrm{Mpin}}$-Cre$_{\mathrm{tg}}$:RIM4$^{\mathrm{fl/fl}}$ mice (mean WT: 1.112, mean KO$_{\mathrm{Pcp2/M}}$: 1.454; Figure 5.14 C), pointing towards a similar variability of ISIs during baseline recordings.

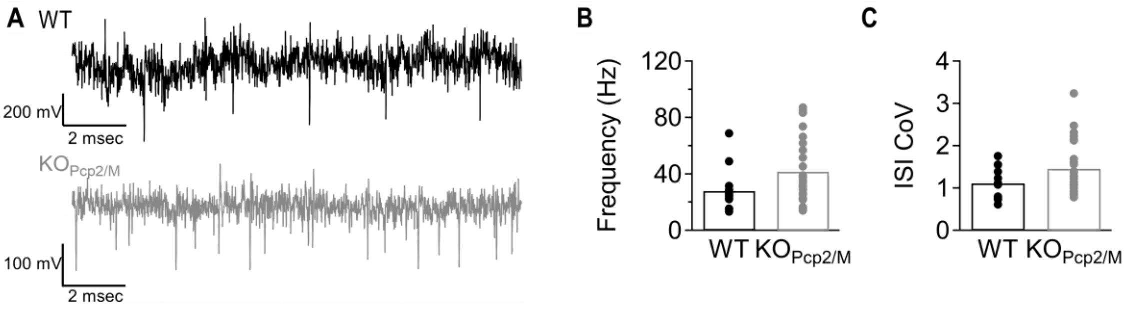

Figure 5.14: Purkinje cell-specific RIM4 deficiency does not alter basal cerebellar network activity. (A) *Left:* Individual LFP traces of Pcp2$_{\mathrm{Mpin}}$-Cre$_{\mathrm{tg}}$:RIM4$^{+/+}$ (WT) and Pcp2$_{\mathrm{Mpin}}$-Cre$_{\mathrm{tg}}$:RIM4$^{\mathrm{fl/fl}}$ (KO$_{\mathrm{Pcp2/M}}$) recordings under baseline conditions. *Right:* Isolated LFP waveforms of action potentials from Pcp2$_{\mathrm{Mpin}}$-Cre$_{\mathrm{tg}}$:RIM4$^{+/+}$ (WT) and Pcp2$_{\mathrm{Mpin}}$-Cre$_{\mathrm{tg}}$:RIM4$^{\mathrm{fl/fl}}$ (KO$_{\mathrm{Pcp2/M}}$) recordings under baseline conditions. LFP are inverted. **(B)** Quantification of single unit mean firing frequency during 10 min baseline recordings in Pcp2$_{\mathrm{Mpin}}$-Cre$_{\mathrm{tg}}$:RIM4$^{+/+}$ (WT) and Pcp2$_{\mathrm{Mpin}}$-Cre$_{\mathrm{tg}}$:RIM4$^{\mathrm{fl/fl}}$ (KO$_{\mathrm{Pcp2/M}}$) mice. Significance: Unpaired Student's t-test, $p = 0.0785$. **C:** Coefficient of variation of ISIs from 10 min baseline recordings in Pcp2$_{\mathrm{Mpin}}$-Cre$_{\mathrm{tg}}$:RIM4$^{+/+}$ (WT) and Pcp2$_{\mathrm{Mpin}}$-Cre$_{\mathrm{tg}}$:RIM4$^{\mathrm{fl/fl}}$ (KO$_{\mathrm{Pcp2/M}}$) mice. ISIs were binned per 1 sec recording time. Significance: Unpaired Student's t-test, $p = 0.086$. For B and C each point corresponds to a neuron. $n = 4$ WT and $n = 5$ KO$_{\mathrm{Pcp2/M}}$ mice per group.

As already described in chapter 5.5.2, a single injection of caffeine induced the episodic motor impairments in constitutive RIM4 KO as well as Pcp2$_{\mathrm{Mpin}}$-Cre$_{\mathrm{tg}}$:RIM4$^{\mathrm{fl/fl}}$ mice. Hence, potential alterations in cerebellar network activity could be monitored during the period of the motor impairments in Purkinje cell-specific RIM4 KO mice by the *in vivo* tetrode recordings. Every mouse was injected on a maximum of three different days once with caffeine during the recording period of up to 14 days. Following the intra peritoneal injection, the single unit recording was continued for additional 40 min. In WT mice single unit firing frequency did not change after injection of caffeine (Figure 5.15 A). However, in Pcp2$_{\mathrm{Mpin}}$-Cre$_{\mathrm{tg}}$:RIM4$^{\mathrm{fl/fl}}$ mice the single unit firing frequency was reduced after caffeine injection, in different manifestations. At similar timepoints of single unit firing frequency reduction, the Pcp2$_{\mathrm{Mpin}}$-Cre$_{\mathrm{tg}}$:RIM4$^{\mathrm{fl/fl}}$ mice developed the episodic motor impairments. As described in chapter 5.5.2, these episodes started with signs of ataxia mainly in the hindlimbs of the mice which developed after minutes to a dystonic phase during which the animals were mostly immobile. By timestamped video monitoring the behavior of the mice could be precisely aligned to the single unit recordings. Therefore, it was possible to compare the behavioral phases of the caffeine-induced episodic motor impairments in $Pcp2_{Mpin}$-Cre_{tg}:$RIM4^{fl/fl}$ mice to the respective single unit firing frequency traces (Figure 5.15 C). Since WT controls never showed signs of the episodic motor impairments, the onsets of the putative 'ataxia' and 'dystonia' phases were calculated as the mean onset and length of the two phases in $Pcp2_{Mpin}$-Cre_{tg}:$RIM4^{fl/fl}$ mice. The single unit firing frequencies were normalized to baseline and changes during the ataxic and dystonic phase were quantified. In WT mice the mean relative frequency was not changed during the putative ataxic ('atx') and dystonic ('dys') phases compared to baseline levels ('atx': 94.70 ± 5.35%; 'dys': 83.86 ± 7.06%; Figure 5.15 B). In contrast, during the ataxic phase of the episodic motor impairments in $Pcp2_{Mpin}$-Cre_{tg}:$RIM4^{fl/fl}$ mice the mean firing frequency decreased compared to baseline conditions with high variability in between neurons. A significant decrease in relative single unit mean firing frequency was detected during the dystonic phase of the episodic motor impairments in $Pcp2_{Mpin}$-Cre_{tg}:$RIM4^{fl/fl}$ mice (atx: 101.76 ± 10.13%; dys: 66.51 ± 13.10%; Figure 5.15 D). The mean onset times of the ataxic and dystonic period of the episodic motor impairments in $Pcp2_{Mpin}$-Cre_{tg}:$RIM4^{fl/fl}$ mice were calculated (mean atx: 495.81 ± 110.89 sec; mean dys: 1056.01 ± 276.91 sec; Figure 5.15 E). Important to note is that the episodic motor impairments always started with ataxic signs and later developed into the dystonic phase.

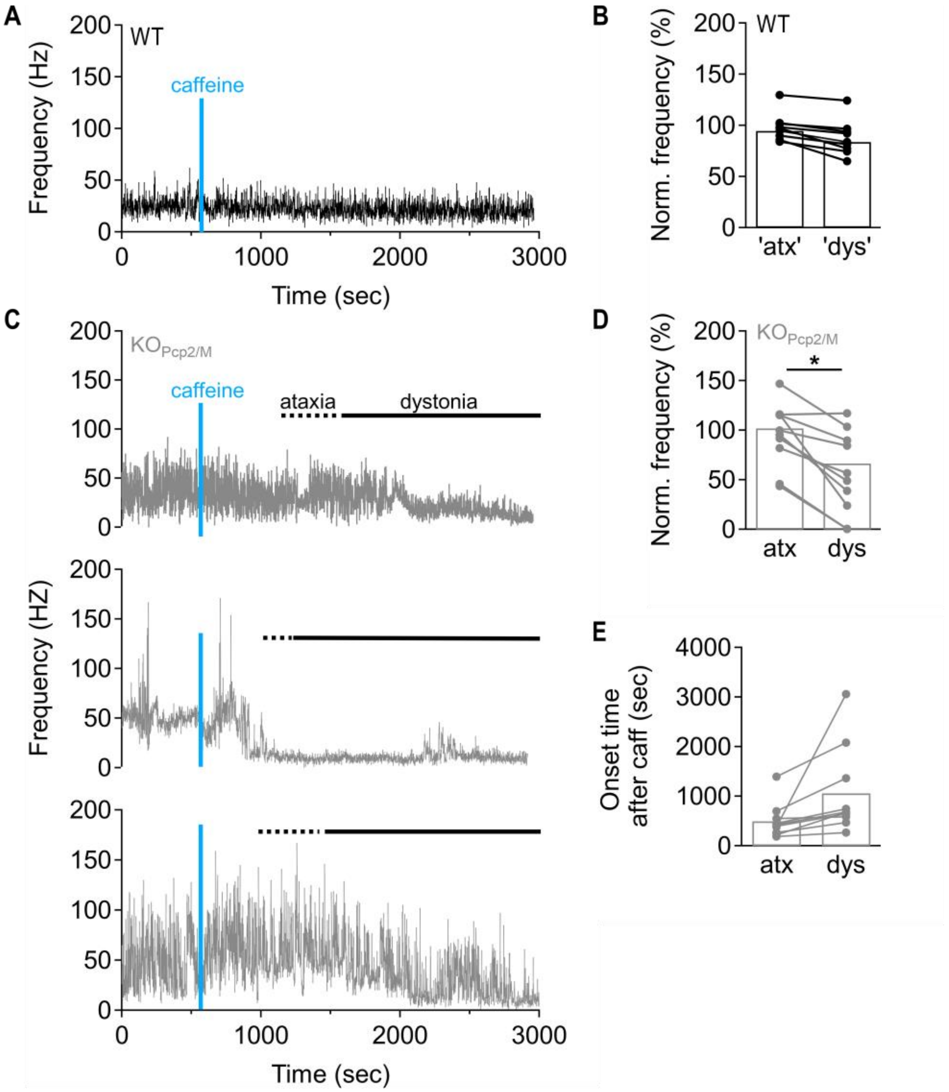

Figure 5.15: Altered firing frequencies of the cerebellar network during the caffeine-induced motor impairments in Pcp2$_{Mpin}$-Cre$_{tg}$:RIM4$^{fl/fl}$ mice. (A) Example single unit firing frequency before and after caffeine injection, recorded in a Pcp2$_{Mpin}$-Cre$_{tg}$:RIM4$^{+/+}$ (WT) mouse. **(B)** Baseline-normalized firing frequencies of single unit recordings in WT mice during the putative ataxic ('atx') and dystonic ('dys') phase of the motor impairments. **(C)** Three example single unit firing frequencies before and after caffeine injection, recorded in Pcp2$_{Mpin}$-Cre$_{tg}$:RIM4$^{fl/fl}$ (KO$_{Pcp2/M}$) mice. The single caffeine injection induced the episodic motor impairments in all Pcp2$_{Mpin}$-Cre$_{tg}$:RIM4$^{fl/fl}$ mice and single unit firing frequencies changed during the two different phases (ataxia and dystonia) of the motor impairments. **(D)** Baseline-normalized firing frequencies of single unit recordings during the caffeine induced ataxic (atx) and dystonic phase (dys) of the motor impairments in KO$_{Pcp2/M}$ mice. **(E)** Onset times with respect to caffeine injection of the induced ataxic (atx) and dystonic (dys) phase of the episodic motor impairments in Pcp2$_{Mpin}$-Cre$_{tg}$:RIM4$^{fl/fl}$ mice. n = 4 Pcp2$_{Mpin}$-Cre$_{tg}$:RIM4$^{+/+}$ and 5 Pcp2$_{Mpin}$-Cre$_{tg}$:RIM4$^{fl/fl}$ mice. For B and D each point corresponds to a neuron. For E each point corresponds to a caffeine injection. Significance: One-way ANOVA with Holm-Sidak's post-test, * $p < 0.01$.

To further characterize the firing pattern of Pcp2$_{\mathrm{Mpin}}$-Cre$_{\mathrm{tg}}$:RIM4$^{\mathrm{fl/fl}}$ mice, the distribution of interspike intervals (ISIs) was investigated. Interestingly, ISI distribution histograms from individual single units during baseline and dystonic conditions of Pcp2$_{\mathrm{Mpin}}$-Cre$_{\mathrm{tg}}$:RIM4$^{\mathrm{fl/fl}}$ mice showed a high frequency of ISIs > 200 ms compared to WT ISI distributions. (Figure 5.16 A, B). Furthermore, the coefficient of variation (CoV) of ISIs over time was calculated, binned to 1-sec intervals. Individual examples of ISI CoV over time were plotted and unveiled a stable progression over time in WT mice without changes after the single injection of caffeine. In Pcp2$_{\mathrm{Mpin}}$-Cre$_{\mathrm{tg}}$:RIM4$^{\mathrm{fl/fl}}$ mice, the ISI CoV was very variable under baseline conditions and during caffeine application, before the episodic motor impairments emerged. The ISI CoV decreased during the dystonic phase of the motor impairments. (Figure 5.16 C,D). Quantification of the CoV ISI unveiled a significant decrease during the dystonic phase in Pcp2$_{\mathrm{Mpin}}$-Cre$_{\mathrm{tg}}$:RIM4$^{\mathrm{fl/fl}}$ mice (WT: mean bl: 1.171, mean 'dys': 1.197; KO$_{\mathrm{Pcp2/M}}$: mean bl: 1.665, mean dys: 1.325; Figure 5.16 E, F).

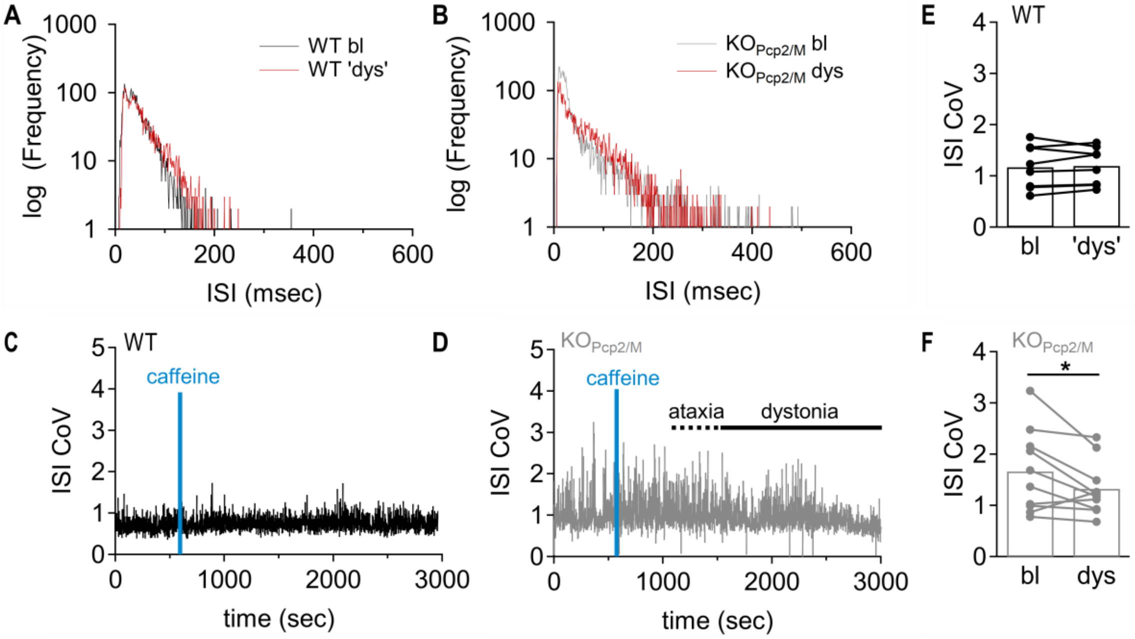

Figure 5.16: Further characterization of cerebellar network activity during the caffeine-induced motor impairments in Pcp2$_{\mathrm{Mpin}}$-Cre$_{\mathrm{tg}}$:RIM4$^{\mathrm{fl/fl}}$ mice. (A), (B) ISI distribution histograms of single units during baseline (bl; black/grey) and the caffeine induced dystonic phase (dys; red) of the motor impairments. For Pcp2$_{\mathrm{Mpin}}$-Cre$_{\mathrm{tg}}$:RIM4$^{+/+}$ (WT) recordings the putative dystonic phase ('dys'; red) was defined as the last 10 min of the recording period. **(C), (D)** Examples of coefficient of variation of ISIs before and after caffeine injection in WT (C) and KO$_{\mathrm{Pcp2/M}}$ (D). **(E), (F)** Coefficient of variation of ISIs from baseline (bl) and the caffeine induced dystonic phase (dys) of the motor impairments. For Pcp2$_{\mathrm{Mpin}}$-Cre$_{\mathrm{tg}}$:RIM4$^{+/+}$ (WT) recordings the putative dystonic phase ('dys') was defined. ISIs were binned per 1 sec recording time. n = 5 Pcp2$_{\mathrm{Mpin}}$-Cre$_{\mathrm{tg}}$:RIM4$^{+/+}$ and 4 Pcp2$_{\mathrm{Mpin}}$-Cre$_{\mathrm{tg}}$:RIM4$^{\mathrm{fl/fl}}$ mice. Significance: paired Student's t-test, p = 0.0428.

In conclusion, deletion of RIM4 in cerebellar Purkinje cells led to alterations of neuronal firing in the cerebellar network. During the caffeine-induced episodic motor impairments, the network activity of $Pcp2_{Mpin}$-Cre_{tg}:$RIM4^{fl/fl}$ mice changed significantly pointing towards a potential cellular role of RIM4 in cerebellar signal generation and transduction.

6 Results: Part B – *In vivo* RIM3 expression patterns

Similar to RIM4, RIM3 is a short isoform of the Rab3A-interacting molecule (RIM) protein family. As RIM4, this protein consists only of a small isoform specific N-terminus and a C2B domain. The cellular function of the protein is still unresolved. Previous *in vitro* studies identified RIM3 expression not only in the presynaptic active zone, as shown for the large isoforms RIM1 and RIM2, but also in the postsynaptic cytomatrix, as well as in the soma and dendrites of neurons. Additionally, reduced levels of RIM3 in neurons lead to a decreased arbor complexity, axon length, and number of spines on functional synapses (Alvarez-Baron et al., 2013). Interestingly, RIM3 mRNA was preferentially detected in excitatory as well as inhibitory cells in the cortex, hippocampus and thalamus by single cell RNAseq experiments (Mouse Brain Atlas; Linnarsson Lab; www.mousebrain.org). Constitutive RIM3 KO mice are viable and fertile and show no obvious motor impairments, in contrast to constitutive and conditional RIM4 KO mice (Katrin Michel, Ph.D. Thesis). The following experiments should give further insights on the RIM3 expression pattern in mouse brain tissue and how the ablation of RIM3 influences other RIM isoforms and the presynaptic protein composition.

6.1 Region-specific RIM3 expression in murine brain tissue

Constitutive RIM3 KO 1st mice carry a LacZ reporter gene cassette inserted with a splice acceptor side between exon 3 and 4 of the *Rims3* gene under the control of the endogenous promotor (Katrin Michel, Ph.D. Thesis, Figure 4.1). Previously published results of *in situ* hybridization studies highlighted non-uniform expression pattern of RIM3 in brain slices of Wistar rats (Alvarez-Baron et al., 2013). The subsequent experiments should unveil if a similar expression pattern could be observed in the newly generated RIM3 KO 1st mouse line, and thereby confirm the successful insertion of the LacZ reporter gene cassette and the splice acceptor site as already shown before in a different set of experiments (Katrin Michel, Ph.D. Thesis). The insertion of the LacZ reporter gene serves as a reporter for endogenous promotor activity, therefore β-galactosidase expression should correspond indirectly to RIM3 expression. β-galactosidase expression was analyzed by X-gal staining in sagittal brain slices of constitutive RIM3 KO 1st and WT littermates as negative controls. This led to a blue precipitate in cells with β-galactosidase indicating RIM3 expression.

The X-gal staining was visible in all cortical layers, especially in layers II/III, in the thalamus and in some cells of the hippocampus, as well as to a minor extend in the granule cell layer of the cerebellum in constitutive RIM3 KO 1st mice (n = 5 mice per group; Figure 6.1). In wildtype mice no X-gal staining was detected (data not shown).

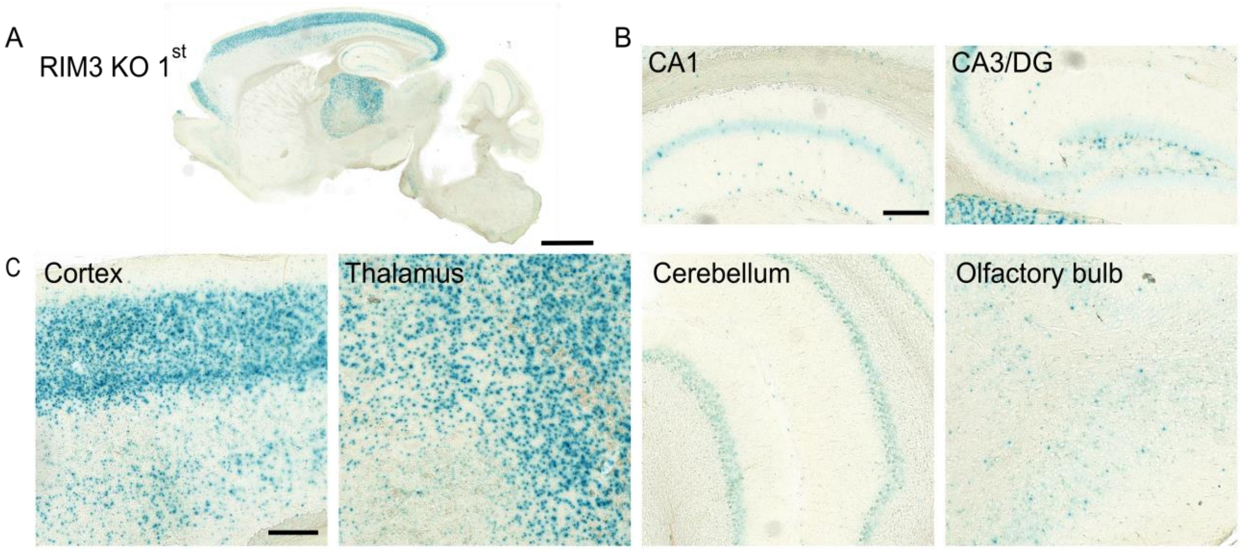

Figure 6.1: Region-specific LacZ expression in RIM3 KO 1st mice. (A) Sagittal slice of a RIM3 KO 1st mouse displays β-galactosidase expression in cortex, hippocampus, thalamus and cerebellum. Some areas of the slice were damaged due to the resectioning process. Scale bar: 500 µm. **(B)** Zoom-in to regions with high β-galactosidase expression. Images labelled with CA1 and CA3/dentate gyrus (DG) show hippocampal regions. **(C)** Zoom-in to other brain regions with high β-galactosidase expression apart from the hippocampus. n = 5 mice per group. Scale bar: 100 µm.

Further immunohistochemical stainings of sagittal slices from constitutive RIM3 KO 1st and WT littermates with a newly generated antibody against RIM3 unveiled a similar staining pattern in WT mice as it was observed in the β-galactosidase stainings. The strongest RIM3 expression could be detected in the cortical layers II/III and the thalamus of WT mice (Figure 6.2; n = 5 per group). In the hippocampus, a subpopulation of neurons, mainly located in the pyramidal layer showed a RIM3-positive staining. In addition, RIM3 immunofluorescence could be also detected in the cerebellar granule cell layer. As expected, the RIM3 signal was reduced in all brain regions in tissue of constitutive RIM3 KO 1st mice. In conclusion, the detection of LacZ expression by X-gal staining in constitutive RIM3 KO 1st mice as well as the immunohistochemical stainings unveiled a non-uniform RIM3 expression pattern in the murine brain. These results suggest a cell-type specific function of RIM3 in brain regions with the highest expression levels. Furthermore, these results confirm the successful insertion of the splice-acceptor cassette in the *Rims3* gene, supporting the hypothesis of a whole brain RIM3 KO in constitutive RIM3 KO 1st mice.

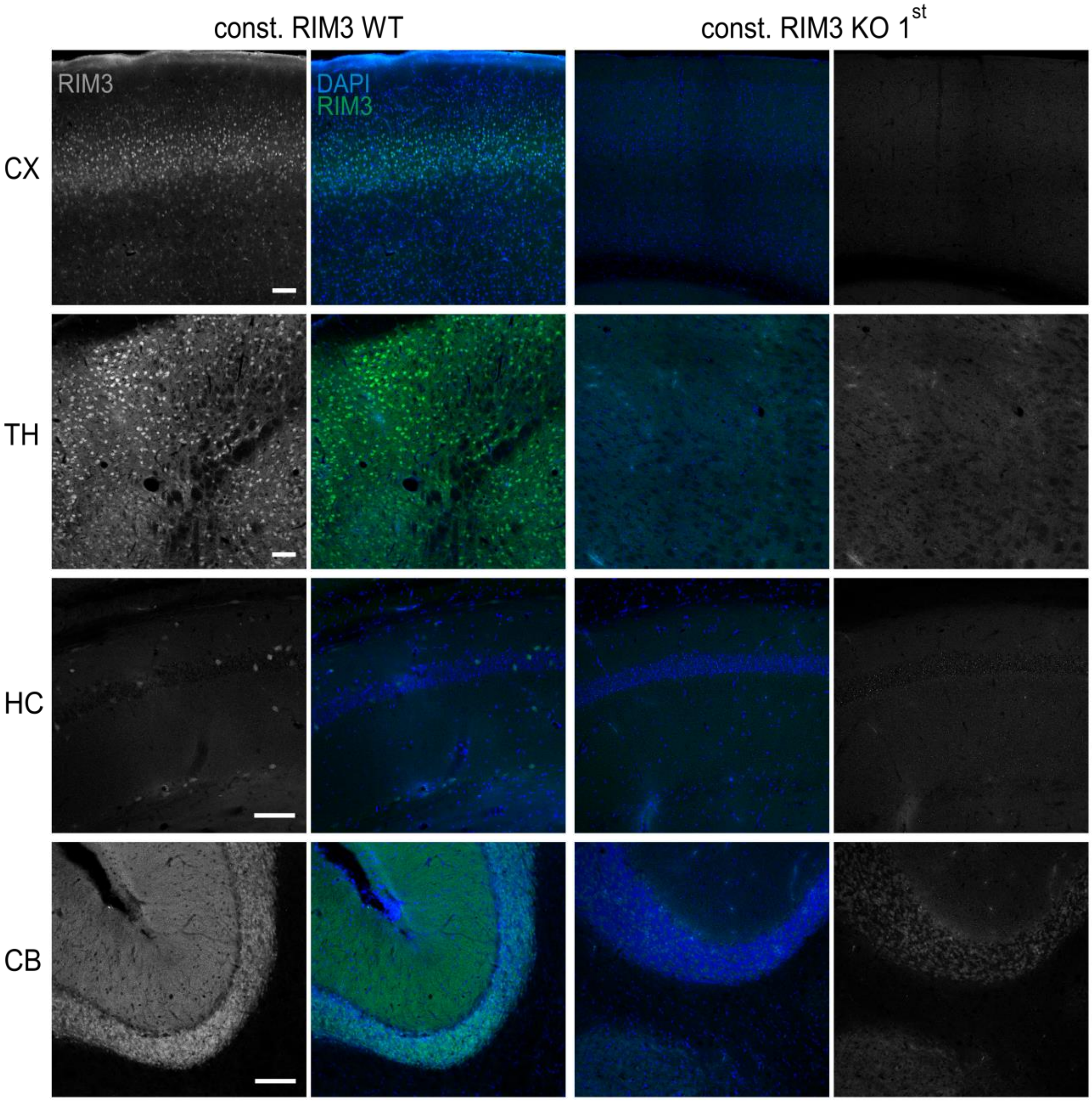

Figure 6.2: RIM3 protein expression is ablated in constitutive RIM3 KO 1st mice. The RIM3 immunofluorescence signal was detected in cortical layers II/III (CX), the thalamus (TH), neuronal subpopulations of the hippocampus (HC) and in the cerebellum (CB) of constitutive RIM3 WT mice. In contrast, the RIM3-specific signal was ablated in constitutive RIM3 KO 1st mice. n = 5 mice per group. Scale bar: 100 µm.

6.2 Altered RIM2β gene expression after RIM3 ablation

In order to unveil potential functional relevance of RIM3, it was hypothesized that its deletion could influence the expression of other RIM isoforms or other pre- and postsynaptic proteins. To this end, transcript and protein levels were characterized in cortex and thalamus tissue of constitutive RIM3 WT and KO 1st mice, two brain regions with high RIM3 expression (chapter 6.1). The mRNA expression levels of RIM isoforms were analyzed with quantitative RT-PCR. The relative expression levels of *Rims3* transcripts were significantly reduced compared to WT levels (cortex: 35.35 ± 5.43 %; thalamus: 17.34 ± 0.59 %; n = 5 mice per group; Figure 6.3). Interestingly, the mRNA of the *Rims2β* isoform was significantly increased in thalamic tissue (thalamus: 177.04 ± 12.68 %) and tended to increase in cortical tissue without reaching statistical significance (cortex: 133.47 ± 9.47%).

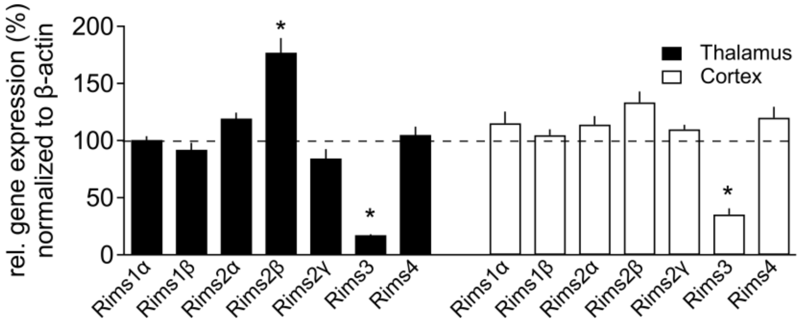

Figure 6.3: *Rims3* gene expression was decreased in constitutive RIM3 KO 1st mice. Quantitative real-time RT-PCR of constitutive RIM3 KO 1st mice normalized to WT levels unveiled a decreased *Rims3* transcript expression in thalamus (solid bars) and cortex tissue (open bars), together with an increase of *Rims2β* transcripts. The gene transcript levels of all other isoforms of the RIM family were similar to WT levels (n = 5 mice per group). Data shown as mean ± SEM. Significance: Two-way ANOVA with Holm-Sidak's post-test, * $p < 0.01$.

This result indicates that the ablation of *Rims3* transcripts could influence also other RIM isoform expression levels in the investigated brain regions, especially *Rims2β* in the thalamus. Since large RIM isoforms are mainly localized at presynaptic active zones and interact with multiple other proteins, we investigated if expression levels of pre- and postsynaptic proteins were altered upon RIM3 deletion. Protein levels were evaluated with quantitative immunoblot analysis of homogenates from thalamus tissue of constitutive RIM3 WT and KO 1st mice. As expected, the relative protein expression of RIM3 was significantly reduced in constitutive RIM3 KO 1st mice. In addition, Munc13 as well as RIM4 protein expression showed a trend towards reduction in thalamus tissue of RIM3 KO 1st mice, not reaching statistical significance (RIM3: 15.15 ± 4.7 %; RIM4: 76.44 ± 8.91 %; Munc13: 64.95 ± 10.24 %; n = 5 mice per group; Figure 6.4). In conclusion, ablation of RIM3 in constitutive RIM3 KO 1st mice results in an increase of *Rims2β* gene expression in thalamic tissue. Additionally, it was proven that the deletion of RIM3 in constitutive RIM3 KO 1st mice led to reduced *Rims3* mRNA levels in cortical and thalamic tissue of these mice. On the protein level, the ablation of RIM3 did not influence the expression levels of other synaptic proteins.

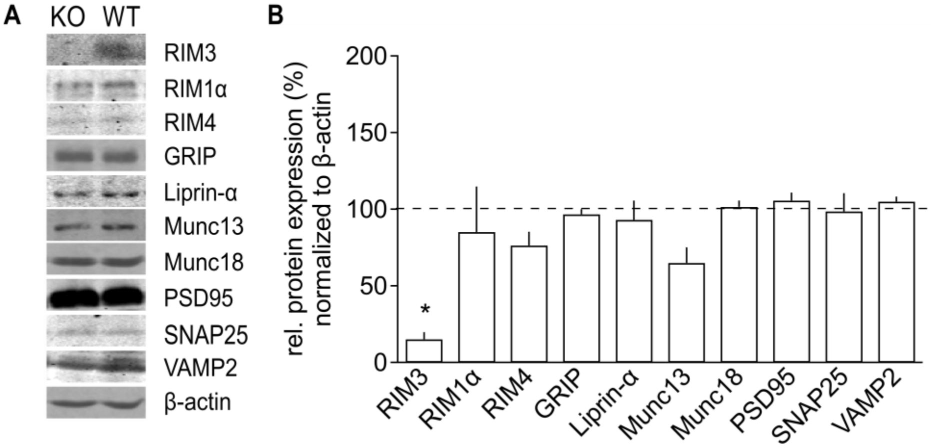

Figure 6.4: RIM3 protein expression was decreased in constitutive RIM3 KO 1st mice. (A) Example immunoblots of thalamus tissue showed a reduction in RIM3 protein expression in constitutive RIM3 KO 1st mice. (**B)** Quantification of immunoblots normalized to WT levels (n = 5 mice per group). Data shown as mean ± SEM. Significance: Two-way ANOVA with Holm-Sidak's post-test, * $p < 0.0001$.

7 Results: Part C – Super-resolution microscopy

7.1 Impact of SRPK2 on synaptic and extrasynaptic ELKS clusters

Drosophila mutant studies on presynaptic proteins identified a kinase specifically associated with active zones, SRPK79D. Further, mutations of this kinase lead to accumulations of Bruchpilot in larval and adult nerves, pointing towards a function in synaptic transmission (Johnson et al. 2009; Nieratschker et al., 2009). The mammalian homologue of SRPK79D, serine/arginine-rich protein-specific kinase 2 (SRPK2) is widely expressed in mouse embryonic tissue and modulates protein-protein or protein-RNA interactions via phosphorylation (Nieratschker et al., 2009). A recent study identified SRPK2 to be involved in the regulation of neurotransmitter release via the phosphorylation of RIM1 in mammalian cells. Interestingly, co-immunoprecipitation experiments could show that ELKS1/2, the homolog of Bruchpilot in *Drosophila*, binds to SRPK2, pointing towards a phosphorylation of this presynaptic proteins, possibly to a lesser extent than it was shown for RIM1 (Müller, Betzin et al., 2022). In order to further elucidate if presynaptic ELKS cluster localization could be by SRPK2, super-resolution imaging was performed.

Primary cortical neurons were transfected at DIV 4-6 with 0.1-0.5µg of U6-GFP, shSRPK2 or SRPK2-OE expressing plasmids using Lipofectamine2000 (Life Technologies, CA, USA) according to the manufacturer's instructions (chapter 4.4.1). The sparse GFP-labeling of the neurons after transfection had the advantage that individual axons could be identified. After immunocytochemical staining with synapsin and ELKS widefield and dSTORM raw image sequences were acquired and a cluster analysis was performed (Figure 7.1 A; chapter 4.8.6).

Synaptic ELKS localizations were slightly but significantly decreased compared to control when SRPK2 was knocked-down (shSRPK2: 0.72 ± 0.16 ELKS localizations normalized to control), whereas the presence of SRPK2 did not influence the number of synaptic ELKS clusters (SRPK2: 1.4 ± 0.33 ELKS localizations normalized to control; Figure 7.1 B). Moreover, the ELKS cluster count per synapse (Control: 3.57 ± 0.4, shSRPK2: 2.92 ± 0.4, SRPK2: 4.23 ± 0.86 cluster count per synapse) and the ELKS cluster area (Control: 3844.09 ± 558.76 nm^2, shSRPK2: 3342.98 ± 292.4 nm^2, SRPK2: 4291.31 ± 619.46 nm^2) showed no significant differences between the conditions. However, a trend towards a reduction in cluster number and area was visible in the SRPK2 knock-down condition, whereas in presence of SRPK2 these parameters tended to increase (Figure 7.1 C,D). The synaptic ELKS cluster density remained unchanged in all conditions (Control: 41.53 ± 1.5 events/pixel, shSRPK2: 39.8 ± 0.56 events/pixel, SRPK2: 38.4 ± 0.8 events/pixel; Figure 7.1 E).

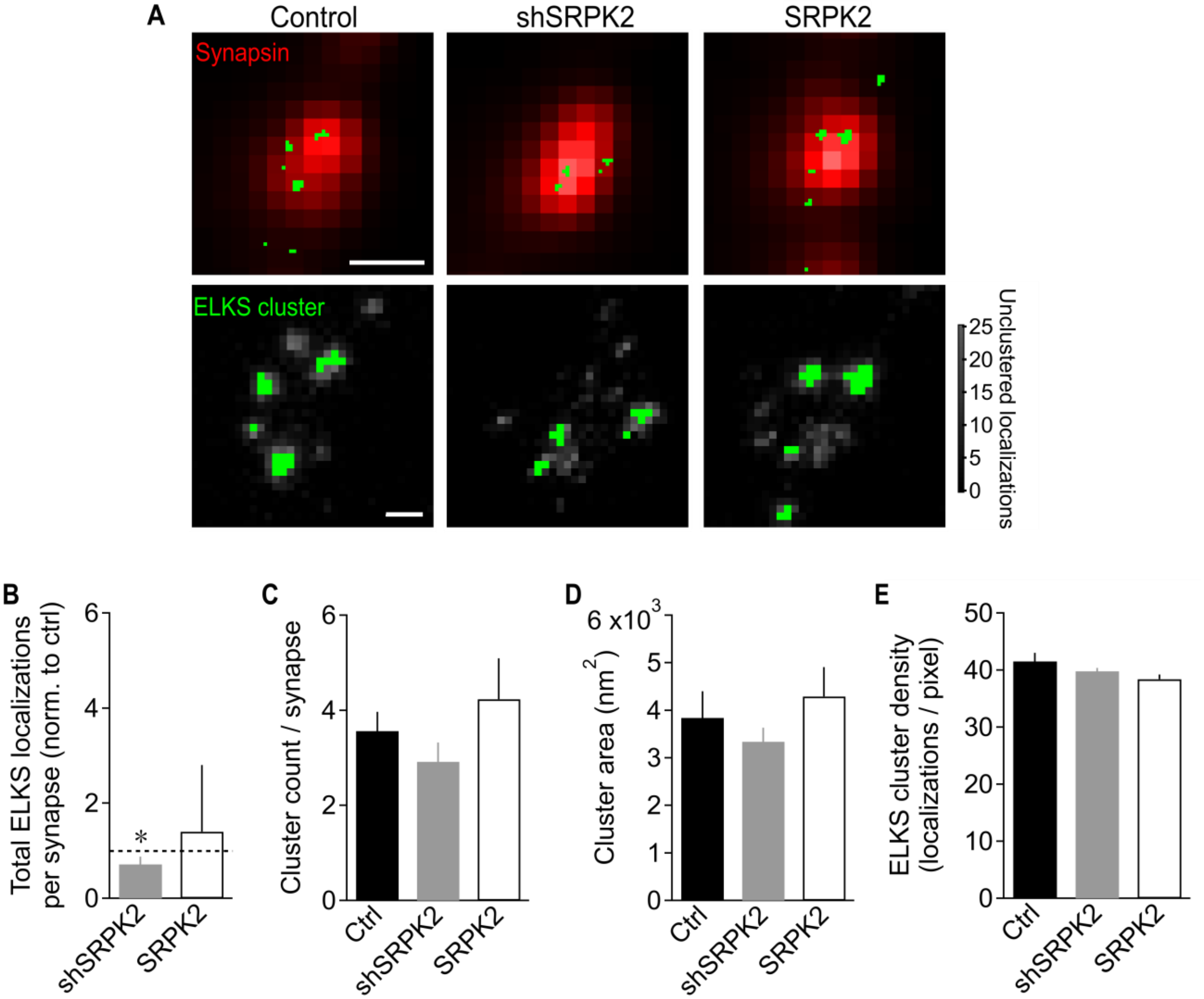

Figure 7.1: Synaptic ELKS localizations were decreased in the absence of SRPK2 whereas ELKS clusters remained unchanged. (A) *Upper row:* single synapse (red) with superimposed ELKS staining (green) for all 3 conditions. Scale bar: 500 nm. *Lower row:* Zoom-in to the same synapse depicted in the upper row with reconstructed ELKS clusters only. Clustered ELKS localizations were depicted in green, unclustered localizations in gray. **(B)** Quantification of total ELKS localizations per synapse normalized to control. **(C)** Quantification of ELKS cluster number per synapse. **(D)** Quantification of cluster area of synaptic ELKS clusters. **(E)** Quantification of synaptic ELKS cluster density. Data represented as mean ± SEM. n = 9; * $p < 0.05$, One-Way ANOVA, Holm-Sidak correction for multiple comparisons.

Previous studies showed that knock-down of the *Drosophila* homolog SRPK79D leads to accumulation of Bruchpilot, the homolog of ELKS in axons (Johnson et al., 2009; Nieratschker et al., 2009). Hence, a potential influence of SRPK2 on extrasynaptic ELKS clusters was investigated for the first time in mammalian neurons. The number of total ELKS localizations per acquisition (shSRPK2: 1.1 ± 0.24, SRPK2: 1.15 ± 0.21 total ELKS localizations normalized to control; Figure 7.2 A) as well as the extrasynaptic ELKS cluster count (Control: 48.19 ± 7.94 clusters, shSRPK2: 33.71 ± 3.46 clusters, SRPK2: 43.82 ± 3.09 clusters; Figure 7.2 B) were not changed across SRPK2 expression levels compared to control conditions. In addition, no change was observed for the extrasynaptic ELKS cluster area in presence or absence of SRPK2 (Control: 2430.61 ± 129.23 nm^2, shSRPK2: 2840.45 ± 168.87 nm^2, SRPK2: 2683.74 ± 154.28 nm^2; Figure 7.2 C). Interestingly, a significant decrease of extrasynaptic ELKS cluster density was detected in presence of SRPK2, compared to control conditions. Whereas, the knock-down of SRPK2 did not influence the cluster density (Control: 44.46 ± 0.59 events/pixel, shSRPK2: 44.7 ± 0.76 events/pixel, SRPK2: 42.2 ± 0.51 events/pixel; Figure 7.2 D).

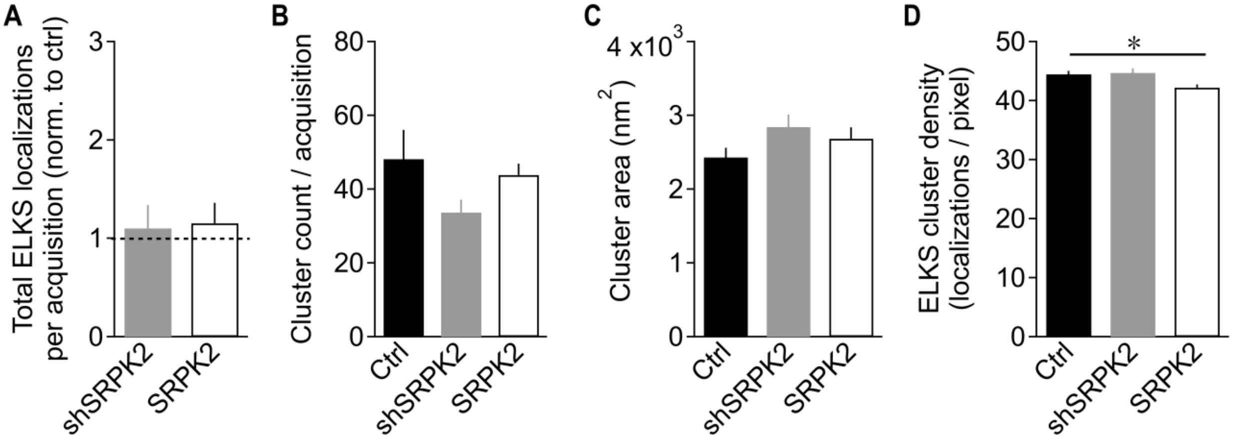

Figure 7.2: Extrasynaptic ELKS cluster density was reduced in the presence of SRPK2. Quantification of **(A)** total extrasynaptic ELKS localizations per acquisition normalized to control, **(B)** extrasynaptic ELKS cluster count per acquisition, **(C)** extrasynaptic ELKS cluster area and **(D)** extrasynaptic ELKS cluster density. Data represented as mean ± SEM. n = 9; * $p < 0.05$, One-Way ANOVA, Holm-Sidak correction for multiple comparisons.

As a next step, the distribution of cluster sizes was analyzed. Since the synaptic and extrasynaptic ELKS cluster area was not changed, it was important to investigate if maybe the presence or absence of SRPK2 influenced the arrangement of ELKS clusters towards smaller or larger ones. Therefore, the cumulative frequency of ELKS cluster areas was calculated (Figure 7.3). Nevertheless, no significant difference of synaptic and extrasynaptic ELKS cluster areas could be detected in presence or absence of SRPK2 compared to control conditions.

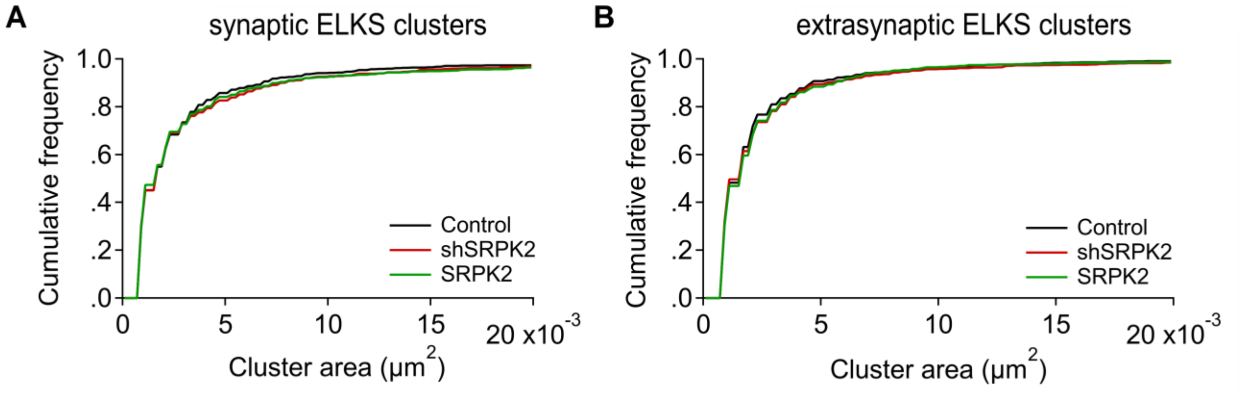

Figure 7.3: ELKS cluster distribution was not changed by SRPK2. (A) Cumulative histogram of synaptic ELKS cluster areas in control (black), shSRPK2 (red) and SRPK2 (green) conditions. **(B)** Cumulative histogram of extrasynaptic ELKS cluster areas in control (black), shSRPK2 (red) and SRPK2 (green) conditions. Kolmogorov-Smirnov (K/S) test, $p > 0.05$.

In conclusion, the absence of SRPK2 reduced the number of synaptic ELKS localizations and presence of SRPK2 increased the extrasynaptic ELKS cluster densities in primary neuronal cultures. Interestingly, SRPK2 presence or absence did not influence synaptic or extrasynaptic ELKS clusters on a nanoscale level in their number and area. In addition, SRPK2 expression did not influence the number extrasynaptic ELKS localizations as well as the ELKS cluster distribution. Therefore, SRPK2 seems to have a smaller impact on ELKS localization in mammalian neurons compared to the results in *Drosophila* (Johnson et al., 2009; Nieratschker et al., 2009). In addition, the SRPK2-induced changes on ELKS were smaller compared to the changes on RIM1 in mammalian neurons (Müller, Betzin et al., 2022).

8 Discussion

RIM proteins have been implicated in cellular functions related to the presynaptic site of neurons. RIM1 and RIM2 are mainly involved in presynaptic transmitter release and presynaptic plasticity. In contrast, the small RIM isoforms RIM3 and RIM4, have been suggested to be involved in broader cellular processes than presynaptic functions. First *in vitro* experiments suggested a potential function of RIM3 and RIM4 primarily in controlling the establishment of axonal and dendritic outgrowth and less involvement of these proteins in synaptic vesicle exocytosis (Alvarez-Baron et al., 2013; Michel et al., 2015). However, the functional role of these RIM isoforms in particular *in vivo* has remained poorly understood. In this study we could identify RIM4 as a novel candidate involved in cerebellar signal generation and transduction. Using Purkinje cell-specific RIM4 KO mice we showed that the cerebellar network activity is changed during the ataxia-like episodic motor impairments occurring in these mice. Furthermore, cell culture experiments unveiled that *Rims4* gene expression is regulated in an activity-dependent manner. Whereas, the transcriptome and proteome of murine cerebellar and cortical tissue was not altered upon RIM4 deletion. Independent of RIM4 function, we could show that the presynaptic kinase SRPK2 interacts with ELKS to a lesser extend as it has been shown for RIM1, thereby modulating the synaptic ultrastructure.

8.1 RIM3 and RIM4 expression pattern in mouse brain tissue

The previously generated constitutive RIM3 and RIM4 KO 1st mice, which carry a LacZ reporter gene cassette, were used to indirectly identify and confirm RIM3 and RIM4 expression patterns via detection β-galactosidase expression in the newly generated mouse lines. Similar to the published *in situ* hybridization results in Wistar rats, β-galactosidase expression could be detected in constitutive RIM3 KO 1st mice in cortical layers II/III, in the thalamus and in some cells of the hippocampus (Alvarez-Baron et al., 2013; Figure 6.1). Additional immunohistochemical stainings of brain slices from constitutive RIM3 WT and KO 1st mice with an isoform-specific RIM3 antibody confirmed these results (Figure 6.2). Furthermore, strong β-galactosidase expression in constitutive RIM4 KO 1st mice was visible in almost all cortical layers, in the hippocampus, the Purkinje cell layer of the cerebellum as already detected with the *in situ* hybridization experiments in Wistar rats (Alvarez-Baron et al., 2013). Interestingly, a strong β-galactosidase expression was additionally visible in a subset of neurons in the inferior olive in the brain stem, a region known for its connection to cerebellar Purkinje cells (Figure 5.1). However, a confirmation of these results by immunohistochemical stainings was not successful due to unspecific binding of the available RIM4 antibodies (data not shown). In comparison, RIM1 and RIM2 seem to be present throughout the brain, with highest levels in the cortex, cerebellum, hippocampus and thalamus (Schoch et al., 2006).

Interestingly, the strong RIM4 expression in the inferior olive, which was not pointed out in previous *in situ* experiments could be confirmed by a published single cell transcriptomic dataset from Sten Linnarson's lab. Here, *Rims3* and *Rims4* genes were identified in neuronal clusters of the previously mentioned brain regions. RIM4 was suggested to be highly expressed in glutamatergic neurons among others in the cerebellum and the inferior olive of the brain stem whereas RIM3 seems to be predominantly expressed in GABAergic interneurons, but could be also detected in excitatory subsets of neurons (unpublished data Stefano Pupe, AG Remy, DZNE Bonn; Zeisel et al., 2018; mousebrain.org). The inferior olive has been shown to be involved in learning and timing of motor behaviors. It sends its projections via climbing fibers to cerebellar Purkinje cells which in turn innervate cerebellar nuclei as the sole source of output signals from the cerebellar cortex (De Zeeuw et al., 1998). The high RIM4 expression levels in the Purkinje cell layer of the cerebellum and in the inferior olive already point to a potential involvement of RIM4 in processes correlated to motor behaviors. In contrast, RIM3 expression appears to be more broadly distributed with the highest expression in GABAergic interneurons (unpublished data Stefano Pupe, AG Remy, DZNE Bonn; Zeisel et al., 2018; mousebrain.org). GABAergic interneurons are capable of synchronizing network rhythms and thereby influence information processing throughout the brain. Importantly, several studies indicate that defects in GABAergic interneurons, which result in the loss of inhibitory regulation and thus an imbalance in the brain's excitation/inhibition system, may underlie symptoms of cognitive disorders, autism and schizophrenia (Molgaard et al., 2014; Nakazawa et al., 2012; Torres et al., 2017). Hence, RIM3 could be potentially involved in some of these processes ensuring normal interneuron information processing and thereby prevent malfunctioning of neuronal networks (Takada et al., 2015; Weidenhofer et al., 2009).

On a cellular level, it was already shown that in contrast to the large isoforms, RIM3 and RIM4 are expressed throughout the cell and are not exclusively localized at presynaptic active zones (Alvarez-Baron et al., 2013; Katrin Michel, Ph.D. Thesis). In the present study, immunoblots of several synaptic proteins unveiled that RIM3 or RIM4 do not influence the expression levels of the investigated synaptic proteins. Removal of RIM3 resulted in no significant decrease of the investigated synaptic proteins in thalamic tissue (Figure 6.4), similar results could be obtained in cerebellar tissue after the removal of RIM4 (Figure 5.5). However, since also other RIM isoforms are expressed in the brain regions where RIM3 or RIM4 were detected, these could be redundant to the two proteins and potentially take over their function when the respective protein is absent. In conclusion, RIM3 and RIM4 have been shown to be expressed in different cellular subtypes in murine brain tissue. In contrast to the large RIM isoforms, RIM3 and RIM4 appear to have a more regionally specialized function which could still involve presynaptic neurotransmitter release.

The potential redundancy of RIM3 and RIM4 was further evaluated by analyzing the transcript levels of all RIM isoforms in cortical, thalamic or cerebellar tissue of constitutive KO 1st mice. If other RIM isoforms would take over the function of the ablated one, these could potentially exhibit a higher transcript level compared to normal gene expression. The ablation of RIM3 resulted in a significant increase of *Rims2β* transcripts in thalamic tissue (Figure 6.3). Interestingly, previous *in situ* hybridization studies showed that RIM2β is in general lower expressed in the brain compared to the large α-isoforms but was specifically highly detected in thalamic tissue, similar to RIM3 (Schoch et al., 2006). However, it seems relatively unlikely that RIM2β takes over RIM3 functions since this isoform is mainly expressed at presynaptic active zones and has been shown to regulate the number of voltage-gated calcium channels (Jung et al., 2015). Nevertheless, RIM3 could eventually be important for the stabilization of RIM2β at the active zone, for instance, via heterodimerization of the C2B domain (Guan et al., 2007). Thereby, RIM3 could lead to an increased RIM2β concentration in the presynapse and in turn could indirectly facilitate synaptic release. In addition, this experiment showed that *Rims3* transcript expression itself is decreased in constitutive RIM3 KO 1st mice, which verified previously obtained data (Katrin Michel, Ph.D. Thesis). Similar analyses were performed with cortical and cerebellar tissue of constitutive RIM4 KO 1st mice. Also in this experiment, no significant changes in RIM isoform transcript levels could be obtained except of *Rims4* itself (Figure 5.4). As for constitutive RIM3 KO 1st mice, this result indicates no influence of RIM4 on the expression levels of other, mainly presynaptically located RIM isoforms in constitutive RIM4 KO 1st mice.

Fluorescent *in situ* hybridization of *Rims4* mRNA in constitutive RIM4 WT and KO brain slices proved previously published RIM4 expression results and unveiled a reduction in *Rims4* mRNA transcript number on a subcellular level in cortical, hippocampal regions as well as in Purkinje cells of the cerebellum (Figure 5.2). In addition, this experiments confirmed the correct knock-out of the newly generated constitutive RIM4 KO mouse line.

In conclusion, the RIM3 and RIM4 expression studies indicated that both proteins show a non-uniform expression pattern in brain tissue of the newly generated constitutive KO 1st mice. Interestingly, in addition to previously identified brain regions with high RIM4 expression, the protein could be detected in the inferior olive of the brain stem. This result, together with the high

RIM4 expression in cerebellar Purkinje cells and the knowledge that constitutive RIM4 KO 1st mice generate episodic motor impairments point towards an involvement of RIM4 in movement-related neuronal communication. In contrast, RIM3 expression appeared high in cortical and thalamic tissue together with a restricted expression in some hippocampal neurons, pointing towards a role in GABAergic interneuron information processing.

8.2 Neuronal activity regulates *Rims4* gene expression levels

Neurons react to changes in activity with an alteration of their molecular composition and structure of specific subcellular compartments, such as synapses, thereby ensuring functionality under changed conditions. This so-called synaptic plasticity occurs in several physiological but also pathophysiological conditions in the brain (Marder and Prinz, 2002; Turrigiano and Nelson, 2004). Additionally, it is well known that chronic silencing of neuronal networks leads to an increased synaptic neurotransmitter release probability, thereby stabilizing neuronal function and prevent that synaptic strength drives out of physiological ranges (Lazarevic et al., 2011; Murthy et al., 2001).

In the present study, primary neuronal cultures were incubated either with TTX, thereby blocking sodium channels and decreasing neuronal activity or gabazine, a GABA$_A$-receptor antagonist, which blocks major inhibitory currents. *Rims4* gene expression increased and peaked significantly 24h after blocking all excitatory neuronal activity by TTX (Figure 5.3). This result could indicate an activity dependent functional mechanism of RIM4 in excitatory neurons. Previous studies indicated that gene expression upon TTX application can be roughly divided into two groups based in their induction kinetics: early genes with increasing transcription rates within minutes and slowly induced genes showing increased scaling after 4 – 24 hours (Ibata et al., 2008; Schaukovitch et al., 2017). In turn, *Rims4* gene expression belongs to the group of genes with slow induction kinetics, ruling out a potential role as an immediate early gene such as *c-fos*.

In addition, the upregulation of *Rims4* transcripts indicates an inverse transcriptional regulation compared to RIM1 and RIM2. It has been previously shown that RIM1 and RIM2 as well as other proteins of the presynaptic active zone are significantly downregulated upon prolonged depletion of activity, corresponding to the here presented data of *Rims1*α gene expression (Figure 5.3; Lazarevic et al., 2011; Müller et al., 2012). Several studies suggest that RIM1 and RIM2 play a major role in homeostatic presynaptic strengthening in silenced neuronal networks (Lazarevic et al., 2011; Müller et al., 2022). In homeostatic plasticity conditions, P/Q-type calcium channels, that are tethered to the presynaptic active zone by RIM1 and RIM2 PDZ-domains, are required for the modulation of Ca^{2+} influx and point mutations in the $Ca_V2.1$ subunit have been shown to impair homeostatic potentiation of presynaptic release (Frank et al., 2006; Müller and Davis, 2012). Since RIM4 is lacking a PDZ-domain, a similar mechanism in tethering calcium channels can be excluded. In addition, previous live-cell TIRF imaging studies of dense-core vesicles in transfected PC12 cells suggested an antagonistic function of α- and γ-RIMs in terms of vesicle anchoring to voltage-gated calcium channels (Uriu et al., 2010). The results of the present study support these hypotheses. Upregulation of RIM4 could lead maybe to a stabilization of the presynaptic release apparatus, by interacting with the β_4-subunits of voltage-gated calcium channels, thereby suppressing the anchoring of neurotransmitter-containing vesicles to these channels *in vitro*. In homeostatic presynaptic scaling conditions this could lead to potentiated responses of calcium sensors, such as synaptotagmins, following regulation of depolarization-dependent neurotransmitter release (Uriu et al., 2010).

Furthermore, earlier studies in mice subjected to status epilepticus-inducing kainic acid or pilocarpine described an upregulation of *Rims4* transcripts 8-12 hours after status induction (Hermey et al., 2013; Katrin Michel, Ph.D. Thesis). In contrast to the here presented data, neuronal activity is dramatically synchronized during the status epilepticus. The previously published data as well as the here presented experiment could point towards a potential regulatory role of RIM4 in malfunctioning neuronal networks. However, it cannot be entirely excluded that the increase in *Rims4* gene transcript expression is a pathological effect without any regulatory function.

Apart from the presynaptic and somatic expression, RIM4 is additionally abundant in postsynaptic compartments of neurons (Alvarez-Baron et al., 2013). Several studies investigated in detail somatic and postsynaptic alterations during activity-dependent changes. Blockade of excitatory input by TTX has been shown to increase the amplitude of miniature EPSCs whereas blocking $GABA_A$-mediated input reduced miniature EPSCs in primary neuronal cultures. Turrigiano et al. suggested that these results could be in part due to postsynaptic alterations in response to glutamate and thereby via postsynaptic accumulation of AMPA-receptors (Turrigiano et al., 1998). Several gene products have been shown to function in signaling cascades involved in the mediation of synaptic scaling (Ibata et al., 2008; Schaukovitch et al., 2017). Concluding from these findings, RIM4 could act as a mediator of postsynaptic changes related to synaptic scaling. Knock-down of RIM4 *in vitro* resulted in a condensation of the Golgi apparatus in the soma and to a reduction of the Golgi size which could indicate a potential function of RIM4 in trafficking mechanisms (Katrin Michel, Ph.D. Thesis). In the present study, the increased gene expression levels of *Rims4* after decreasing neuronal activity by incubation with TTX could point towards a potential function of RIM4 in postsynaptic trafficking mechanisms for homeostatic synaptic scaling.

Taken together, the upregulation of *Rims4* after decreasing neuronal activity could be indicative for a potential function in homeostatic synaptic scaling mechanisms. In addition, the rather uniform subcellular distribution of RIM4 supports the hypothesis of a not solely presynaptic but rather somatic or postsynaptic involvement in scaling mechanisms.

8.3 Absence of RIM4 expression does not influence the abundance of other cortical and cerebellar genes and proteins

The occurrence of the episodic motor impairments of constitutive RIM4 KO mice led to the hypothesis that the deletion of *Rims4* mRNA or the RIM4 protein respectively could influence the expression of other genes and proteins in cortical and cerebellar tissue. An altered expression would in turn point towards a functional relation of RIM4 and the identified genes and/or proteins. Interestingly, a previously performed mass spectrometry approach identified several interaction partners of RIM4 in whole brain lysates and synaptosomal preparations (Katrin Michel, Ph.D. Thesis). To this end, a transcriptomics and a proteomics approach should unveil potential changes in gene and protein expression in constitutive RIM4 KO mice.

In the here presented principal component analysis, the gene and protein expression profiles of cerebellar tissue appeared more widespread compared to the data sets of cortical tissue (Figure 5.6). These results indicate that the transcriptomic and proteomic expression profiles are more variable in cerebellar compared to cortical tissue in both, constitutive RIM4 WT and KO mice. Previous studies showed that apart from the master clock located in the suprachiasmatic nucleus, the cerebellum itself is known as a secondary-oscillator and therefore, obtains a circadian rhythmicity of specific protein expression. Expression peaks were observed around midnight, midday and for some proteins in the late afternoon (Plumel et al., 2019). To reduce an influence of circadian gene and protein expression in constitutive RIM4 WT and KO mice, the tissue preparation in the present study was performed around the same time during the day. However, a variability in gene and protein expression was still present. This could be due to the fact that there is a high variability in gene expression among cell types and cerebellar lobules in naïve cerebellar tissue (Kozareva et al., 2021; Wizeman et al., 2019). The cerebellar and cortical tissue used in the here presented study was not microdissected, but rather used in its entirety which could explain the results of the principal component analysis. In addition, constitutive RIM4 KO mice develop episodic motor impairments which occur not regularly but at different time points and with different durations. These episodes of altered motor movements could be another explanation for a more diverse and widespread gene and protein expression profile in constitutive RIM4 KO mice. However, it would not explain the PCA results in constitutive RIM4 WT mice.

In a next step, the data was analyzed regarding potential differentially regulated candidate genes and proteins that showed an altered expression upon RIM4 deletion. Surprisingly, no alterations of protein expression in cerebellar and cortical tissue could be detected. Even the deletion of RIM4 itself, which was already confirmed previously in these mice (chapter 5.1, chapter 5.3, Katrin Michel, Ph.D. Thesis) could not be verified in the proteomics data sets. In the transcriptomic data of cerebellar tissue only the *Rims4* gene was significantly downregulated, whereas the cortical transcriptomics data set comprised two other differentially regulated genes apart from the downregulated *Rims4* gene. *Ccl17* could be identified as significantly upregulated after ablation of RIM4. The *Ccl17* gene codes for the C-C motif chemokine ligand 17 and is a chemotactic factor for T-lymphocytes. Additionally, it may play a role in T-cell development in the thymus and in the trafficking and activation of mature T-cells (Imai et al., 1996). According to the Allen Brain Atlas, *Ccl17* is expressed only at very low levels in the isocortex as well as in all other brain regions (isocortex raw expression value: 0.43, $\log_2$: -1.22; mouse.brain-map.org). Since this chemokine is secreted into the blood, its upregulation in the cortical data set could be explained by a potential contamination with peripheral blood during the tissue preparation. The other significantly downregulated gene which was detected in the cortical transcriptomics data set was the pseudogene *Gm28438*. Pseudogenes are nonfunctional DNA-segments that lack regulatory sequences or obtain a nonfunctional coding sequence due to frameshifts or premature stop codons. The detected pseudogene *Gm28438* is confirmed in the mouse genome informatics (MGI) database as a pseudogene found in C57BL/6J mice on chromosome 1 and is expressed in almost all murine tissues (ID: MGI:5579144; informatics.jax.org). Concluding from these findings, both identified significantly regulated genes *Ccl17* as well as *Gm28438* do not point towards a potential function of RIM4.

Nevertheless, it is still remarkable that no significantly altered gene or protein could be identified with these four different omics approaches. A possible explanation could be that the large number of unaltered genes and proteins throughout the cerebellar tissue mask the few altered genes, for example, if the altered genes are present only in cerebellar Purkinje cells or other subtypes of cells. For this reason, microdissection of defined cerebellar regions for instance lobules V/VI could have enhanced the detection limit of changes in gene and protein expression. In addition, it is well known that especially the cerebellar structure is widely divers and regionally specialized (Kozareva et al., 2021). Even the Purkinje cell layer itself can be divided into different zones, for instance depending on glycolytic enzyme aldolase C (zebrin II) expression (Wu et al., 2019). Following, a next step to unveil potential changes after RIM4 ablation could bea RNAseq approach with defined cerebellar regions or layer or a single-cell RNAseq approach where clusters of cells expressing a different subset of genes could be compared between constitutive RIM4 WT and KO mice. In conclusion, a more regionally specialized omics approach is needed to further identify potential changes in gene and protein expression profiles. In the present study it was not possible to identify any candidate genes or proteins altered upon RIM4 deletion except of *Rims4* itself.

8.4 Purkinje cell-specific RIM4 ablation induces episodically occurring motor impairments in mice

Since constitutive RIM4 KO mice generate episodic motor impairments, starting around 3 weeks after birth, it was hypothesized that RIM4 could be primarily involved in normal motor coordination and movement. In order to further investigate this potential function, Pcp2$_{\text{Mpin}}$-Cre$_{\text{tg}}$:RIM4$^{\text{fl/fl}}$ mice were generated. The restricted expression and localization of Cre recombinase in cerebellar Purkinje cells was verified by tdTomato-reporter breedings (Figure 5.10). Throughout their life, the Pcp2$_{\text{Mpin}}$-Cre$_{\text{tg}}$:RIM4$^{\text{fl/fl}}$ mice stayed smaller compared to WT and heterozygous littermates, as previously described for constitutive RIM4 KO 1st mice (Figure 5.11; Katrin Michel, Ph.D. Thesis). Interestingly, a weight reduction was also observed in other mouse models with mutations in genes related to cerebellar Purkinje cell function, for instance in the *Rora*, *Nr* or the *Agtpbp1* gene (Heuzé et al., 1997; Lalonde and Strazielle, 2003; Mullen et al., 1976). Together with the weight reduction, Pcp2$_{\text{Mpin}}$-Cre$_{\text{tg}}$:RIM4$^{\text{fl/fl}}$ mice developed spontaneous episodically occurring motor impairments, as already observed in constitutive RIM4 KO mice (Figure 5.12; Katrin Michel, Ph.D. Thesis). These drastic episodes of uncontrolled and very reduced movement of the mice could be one explanation of the observed weight reduction occurring at similar timepoints during postnatal development. The episodes occurred most often during their active phase and lasted up to 6h. The mice appeared mostly rigid and sometimes even paralyzed, so that a normal food and water intake could not be granted. However, the eating behavior of the mice was not quantified. Already from these observations, it could be concluded that RIM4 is essential for Purkinje cell-derived cerebellar information processing which is potentially involved in normal motor coordination. Interestingly, the first occurrence of the episodic motor impairments in Pcp2$_{\text{Mpin}}$-Cre$_{\text{tg}}$:RIM4$^{\text{fl/fl}}$ mice was observed around p21, which is the timepoint, where the RIM4 protein expression reaches a plateau level, as shown in whole rat brain lysates (Alvarez-Baron et al., 2013). Since also other synaptic proteins show an increased expression during development and reach a plateau around p21 (Song et al., 1999; Stettler et al., 1994), these findings suggest that only a reduction in fully established RIM4 protein levels leads to the observed episodic motor impairments, thereby excluding a function of RIM4 in development. On a cellular level, the first postnatal weeks have a huge influence on neuronal circuit development. In the cerebellum the two major extrinsic inputs to the cerebellar cortex mature: the inferior olive's climbing fibers to the Purkinje cells and the spinal and reticular mossy fibers to the granule cells (Goldowitz and Hamre, 1998). In mice Purkinje cell generation itself occurs at very early time points, primarily at embryonic days E11 and E12 (Leto et al., 2012; Miale and Sidman, 1961). The hypothesis that RIM4 does not influence cerebellar development could be further tested for instance by tamoxifen-induced Purkinje cell-specific RIM4 KO mice, where RIM4 could be ablated at different time points to investigate potential differences in the occurrence of the episodic motor impairments. Moreover, the fact that the spontaneous motor episodes appear almost once per day in the KO mice and seem to have a circadian distribution, together with the *in vitro* finding that RIM4 is upregulated 24h upon alterations of neuronal activity, could point towards an activity-dependent, maybe hormonal-regulated RIM4 function.

The symptoms occurring during the episodic motor impairments, most importantly abnormal movements and immobility of the mice indicate potential deficits of general motor behavior. However, during the episode-free phases, the mice appeared normal and displayed no obvious signs of motor abnormalities. The motor impairments could be visually separated in two distinct phases. In the beginning, the mice showed an ataxic phenotype with uncontrolled movements and hind limb liftings. After several minutes, the phenotype changed towards a more dystonic phase during which the movement is reduced, the mice appear paralyzed and the limbs are stretched out (Figure 5.12). Strikingly, several other mouse models, showing similar motor impairments have been described, for instance *Hotfoot*, *Nervous*, *Staggerer* or *tottering* mice (Campbell and Hess, 1996; Green and Sidman, 1962; Heuzé et al., 1997; Lalonde and Strazielle, 2003; Lalouette et al., 1998; reviewed in Cendelin, 2014; Hoxha et al., 2018). All of them have in common that mutations in different genes or the transgenic knock-out of specific genes in cerebellar Purkinje cells lead to most often permanent, but sometimes even episodic alterations in normal movement and motor coordination. Many of these mouse models have been associated to human cerebellar ataxias or dyskinesias. For instance *Hotfoot* mice contain mutations in the *Grid2* gene, coding for the ionotropic glutamate receptor delta type 2 (GluD2) and two consanguineous families with cerebellar ataxia showed similar loss-of-function mutations in this gene (Hills et al., 2013). Furthermore, Ophoff and colleagues identified loss-of-function mutations in the *Cacna1a* gene in patients with episodic ataxia type 2 (Ophoff et al., 1996) and at the same time mutations in this gene were described as leading to an ataxic phenotype in *tottering* mice (Campbell and Hess, 1996). Cerebellar ataxias are described in humans as the poor coordination of movements, balance and gait as a result of a disease in the cerebellum (Becker, 2014). The term cerebellar ataxia can be subdivided into several different classes, comprising genetic, hereditary causes, infectious and toxic causes as well as paroxysmal or traumatic causes (Manto et al., 2019; Perlman, 2000). From a neurological point of view, the motor impairments occurring in constitutive and $Pcp2_{Mpin}$-Cre_{tg}:$RIM4^{fl/fl}$ mice most probably resembles symptoms of episodic ataxia or paroxysmal dyskinesias, due to their episodic nature and occurrence of gait-affecting motor symptoms (Jen and Wan, 2018; Unterberger and Trinka, 2008). However, the episodically occurring motor impairments themself could be more related to dystonia, characterized by sustained muscle contractions which generate twisting and repetitive movements (Malone et al., 2014). Further electromyography (EMG) recordings would help to reveal potential alterations in muscles of the RIM4 KO mice (Scholle et al., 2010). In conclusion, the *Rims4* gene is a potential candidate involved in the generation of these movement disorders.

By comparing the motor-related phenotypes of mouse models described in the literature with the episodically occurring motor impairments of RIM4 KO mice, it became obvious that mainly mutations in voltage-gated calcium channels or voltage-gated potassium channels, but also metabotropic glutamate receptors could lead to comparable behavioral and physiological changes in cerebellar Purkinje cells. However, many of these mouse models show a persistent ataxia without occurrence of spontaneous attacks and very often this goes along with dramatic loss or rearrangement of cerebellar Purkinje cells (Hoxha et al., 2018; Mullen et al., 1976; Sidman et al., 1962). Such severe symptoms, regarding cerebellar morphology have not been observed in RIM4 KO mice. Most symptoms occurring during the episodic motor impairments of RIM4 KO mice have been similarly described for mice carrying mutations in voltage-gated calcium channels or their auxiliary subunits, for instance the *tottering* and *purky* mice. The *tottering* mice carry a mutation in the *Cacna1a* gene, coding for the α-subunit of P/Q-type voltage-gated calcium channels, whereas the *purky* mice do not express P/Q-type voltage-gated calcium channels in cerebellar Purkinje cells (Fletcher et al., 1996; Mark et al., 2011). The homozygous *tottering* mutation induces ataxic gait disturbances of the mice around 3 weeks after birth and a few days after episodes of dystonia are observable. The episodes in *tottering* mice last 30-60 min and occur one to two times per day, without loss of consciousness (Campbell et al., 1999), comparable to the episodic motor impairments in constitutive and conditional RIM4 KO mice. Moreover, in *tottering* mice no abnormalities in gross cerebellar morphology could be observed although the mutant mice show a significant decrease in body weight as well as in cerebellar weight, similar to results obtained from RIM4 KO mice (Noebels and Sidman, 1979; Katrin Michel, Ph.D. Thesis). In *purky* mice the citrine-tagged α-subunit of P/Q-type voltage-gated calcium channels is specifically knocked out in cerebellar Purkinje cells. Interestingly, these mice develop similar motor impairments as observed in *tottering* as well as in the here described $Pcp2_{Mpin}$-Cre_{tg}:$RIM4^{fl/fl}$ mice, starting around 3 weeks after birth with ataxia and episodes of paroxysmal dyskineasias (Mark et al., 2011). However, episodes in *tottering* and *purky* mice are with a duration of +/- 40 min shorter than the ones observed in RIM4 KO mice which last up to 6 hours. Interestingly, the episodes of paroxysmal dyskinesias in *purky* mice were inducible by stress, for instance by a new environment or cage transport (Mark et al., 2011). The responsiveness to stress of $Pcp2_{Mpin}$-Cre_{tg}:$RIM4^{fl/fl}$ mice was not quantified in this study, while it was well observed that transporting the mice in closed, dark boxes for several minutes did induce the motor impairments. Apart from voltage-gated calcium channels, mice lacking the α-subunit of large-conductance voltage and calcium-activated potassium (BK) channels specifically in cerebellar Purkinje cells show signs of ataxia in behavioral test such as footprint and balance beam tests (Chen et al., 2010). However, no information about spontaneous episodic motor impairments have been published for PC $BK^{-/-}$ mice, pointing towards a different molecular mechanism compared to the one present in constitutive RIM4 KO and $Pcp2_{Mpin}$-Cre_{tg}:$RIM4^{fl/fl}$ mice.

In order to further characterize the episodic motor impairments of $Pcp2_{Mpin}$-Cre_{tg}:$RIM4^{fl/fl}$ mice and to potentially relate them to human episodic ataxia type 2, a treatment with 4-aminopyridine or chlorzoxazone could improve motor function and intrinsic Purkinje cell pacemaking in these mice as it has been shown for *tottering* mice (Alviña and Khodakhah, 2010a, 2010b; Walter et al., 2006).

In conclusion, $Pcp2_{Mpin}$-Cre_{tg}:$RIM4^{fl/fl}$ mice phenocopy the episodically occurring motor impairments observed in RIM4const KO and constitutive RIM4 KO 1st mice. Intriguingly, ataxic mouse models with mutations in the P/Q-type voltage-gated calcium channel of Purkinje cells show very similar phenotypes, pointing towards a potential involvement of RIM4 in voltage-gated calcium channel function and a possible calcium channelopathy, thereby potentially resembling human episodic ataxia type 2.

8.5 RIM4 is involved in the stability of cerebellar network activity

Early lesion studies already described the cerebellum as being involved in motor functions and movement (Flourens, 1824). The underlying cerebellar architecture is composed of highly regular neuronal units, each sharing the same basic microcircuitry (Roostaei et al., 2014). The main output of these microcircuits are cerebellar Purkinje cells, directly projecting to specific cell groups of the deep cerebellar nuclei. Purkinje cells receive excitatory input from climbing and parallel fibers as well as inhibitory input from stellate and basket cell interneurons. Cerebellar Purkinje cells have a characteristic firing pattern, consisting of two types of action potentials. Simple spikes are generated intrinsically by parallel fiber input, whereas complex spikes are elicited by climbing fiber input. Complex spikes are distinguishable from simple spikes by their unique waveform consisting of a single large spike followed by three to five smaller spikes (Arancillo et al., 2015; Schmolesky et al., 2002).

Since $\mathrm{Pcp2_{Mpin}}$-$\mathrm{Cre_{tg}}$:$\mathrm{RIM4^{fl/fl}}$ mice phenocopy the episodically occurring motor impairments of constitutive RIM4 KO mice, further experiments should prove the hypothesis that these mice show alterations in Purkinje cell discharges as it was already described in other ataxic mouse models (Hoxha et al., 2018). This would indicate a potential function of RIM4 in modulating the cerebellar output for motor coordination and movement. *In vivo* tetrode recordings were performed in freely moving $\mathrm{Pcp2_{Mpin}}$-$\mathrm{Cre_{tg}}$:$\mathrm{RIM4^{fl/fl}}$ mice and WT controls. Microdrives with four movable tetrodes were implanted using coordinates to reach the lobules V/VI of the cerebellar vermis. The acquired single unit recordings were clearly separable from noise. However, the separation of Purkinje cell waveforms from other cerebellar cell types by identification of complex spikes was not successful. On the one hand, this could be due to technical limitations in regard to filter settings during signal acquisition. On the other hand, it could not be entirely excluded that single unit recordings from other cerebellar cell types, for instance granule cells were acquired. Thus, the single unit data from the *in vivo* tetrode recordings were interpreted as cerebellar network activity, not discriminating between cell types. The here obtained results of *in vivo* single unit recordings point towards the recording of cerebellar Purkinje cells since comparable results of *in vivo* recordings in ataxic mouse have been shown in the literature (Tara et al., 2018). Though, it was not possible to confirm the recording of Purkinje cells.

In baseline conditions, $\mathrm{Pcp2_{Mpin}}$-$\mathrm{Cre_{tg}}$:$\mathrm{RIM4^{fl/fl}}$ mice tend to have an increased firing frequency of cerebellar network activity compared to WT controls, not reaching statistical significance. Furthermore, the coefficient of variation of interspike intervals was not altered, indicating unchanged variability of interspike intervals during baseline recordings (Figure 5.14). This result resembles the phenotypic appearance of Pcp2$_{Mpin}$-Cre$_{tg}$:RIM4$^{fl/fl}$ mice in absence of the motor impairments. The mice behave normally without obvious movement alterations. Similar results were described in the literature for mouse models with episodic ataxia, for instance in *tottering* or *leaner* mice (Raike et al., 2015; Walter et al., 2006). Under baseline conditions RIM4 seems to play a minor role in correct information processing of cerebellar Purkinje cells. However, potential subcellular alterations induced by the deletion of RIM4 could be taken over by other processes.

To further examine the alterations generated by the deletion of RIM4, the focus of the *in vivo* single unit recordings was set to analyze the cerebellar network activity during the episodically occurring motor impairments. As it was already described for constitutive RIM4 KO mice, the episodic motor impairments of Pcp2$_{Mpin}$-Cre$_{tg}$:RIM4$^{fl/fl}$ mice were inducible by single intraperitoneal injections of ethanol or caffeine and by stress (unpublished data, Katrin Michel and Nesrine Melliti). In this experimental setup caffeine injections were used to evoke the motor impairments in Pcp2$_{Mpin}$-Cre$_{tg}$:RIM4$^{fl/fl}$ mice during the single unit tetrode recordings. Interestingly, the normalized cerebellar firing frequency was significantly reduced during the dystonic phase of the motor impairments in Pcp2$_{Mpin}$-Cre$_{tg}$:RIM4$^{fl/fl}$ mice (Figure 5.15). Caffeine, similar to ethanol or stress, is a multi-target agent, acting at many different sites in the central nervous system. The three main mechanisms of action for caffeine are: mobilization of intracellular calcium, inhibition of phosphodiesterases and antagonization of adenosine receptors (Nehlig et al., 1992). The presence of high caffeine concentrations in the brain would lead to increased intracellular calcium concentrations by releasing Ca^{2+} from intracellular stores via IP3 and ryanodine receptors, thereby leading to the activation of multiple positive and negative feedback effects of Ca^{2+} favoring synchronized activation and rapid deactivation of calcium channels and by the homeostatic regulation of Ca^{2+} removal mechanisms (Bagur and Hajnóczky, 2017). In addition, caffeine would increase the concentrations of cyclic AMP in the brain by inhibition of phosphodiesterases. Since caffeine has been reported as a weak inhibitor of phosphodiesterases, its main function relies probably on the blockade of adenosine receptors (Choi et al., 1988). Adenosine receptors have been shown to be widely expressed in the brain. However, among all four different adenosine receptor subtypes, only the adenosine A1 receptor has been identified in the cerebellar structure, more precisely in cerebellar granule cells (Dixon et al., 1996; Wojcik and Neff, 1983). Adenosine A1 receptors are located presynaptically at parallel-fiber-Purkinje cell synapses, thereby leading to an adenosine-induced reduction of transmission via G_i proteins (Kocsis et al., 1984). Caffeine could in turn alter the input to Purkinje cells via inhibition of the A1 receptors on parallel fiber presynapses. By injection to Pcp2$_{Mpin}$-Cre$_{tg}$:RIM4$^{fl/fl}$ mice, caffeine triggers the episodic motor impairments probably by a mixture of the above mentioned mechanisms.

Several hypotheses for RIM4 function can be pointed out from the results of the *in vivo* single unit recordings in the current study. Ataxic mouse models usually share mutations in different ion channel subunits, leading to channelopathies which exhibit an ataxic phenotype as a major symptom. In this regard, it can be hypothesized that also the deletion of RIM4 in cerebellar Purkinje cells could lead to changes in ion channels, for instance voltage-gated calcium channels which in turn could lead to the ataxia-like episodically occurring motor impairments observed in RIM4 KO mice. Such ion channel changes could be for instance channel mislocalizations inside the cell or a reduction in functionality due to missing or incorrect subunit binding. In particular, RIM4 has been shown to be involved in the regulation of vesicular trafficking (Katrin Michel, Ph.D. Thesis), thereby ablation of RIM4 could lead to a reduction or mislocalization of ion channels at their specific sides of action. Further, RIM4 has been shown to directly bind to β-subunits of voltage-gated calcium channels, thereby influencing the gating-properties of these channels (Uriu et al., 2010).

In the literature *in vivo* recordings of cerebellar Purkinje cells in *tottering* mice during caffeine-triggered episodes of motor dysfunction unveiled a burst firing phenotype, indicating an altered regularity of Purkinje cell firing as a cause of the motor abnormalities in these mice (Tara et al., 2018). Moreover, this reduced precision of intrinsic Purkinje cell pacemaking in *tottering* mice occurred due to fewer calcium-activated potassium channel openings with each action potential, leading to smaller after-hyperpotentials (AHP). A mechanism that could be upregulated in this example is the increase in the calcium-affinity of SK channels, thereby activating more calcium-activated potassium channels and in turn restore the precision of Purkinje cell pacemaking (Walter et al., 2006). In terms of RIM4 deletion one could hypothesize, keeping in mind that the episodic motor impairments occur spontaneously once per day, that a certain threshold of intracellular signaling, for instance Ca^{2+} signaling must be reached in order to induce the impairments. Without reaching this threshold, the mouse would show a normal motor behavior, even with minor subcellular changes, not detectable in cerebellar firing rate and coefficient of variation of inter-spike intervals, as it was recorded in the here performed experiments. Interestingly, the coefficient of variation of interspike intervals of cerebellar firing also significantly changed during the dystonic phase of the episodic motor impairments in $Pcp2_{Mpin}$-Cre_{tg}:$RIM4^{fl/fl}$ mice, pointing towards an altered regularity, together with a reduced cerebellar firing frequency (Figure 5.15; Figure 5.16). However, in this study the reduction of the coefficient of variation after caffeine injection and therefore motor impairment induction points towards a more regular firing of cerebellar activity in contrast to the findings in *tottering* mice. The significant reduction of cerebellar firing frequency could be a result of less excitation in cerebellar microcircuits, for instance by reduced Ca^{2+} entry via alterations in voltage-gated calcium channels. This in turn could lead to reduced activation of calcium-dependent potassium channels which would cause a more depolarized membrane potential that would then block sodium channel activation (Donato et al., 2006; Hoxha et al., 2018). Caffeine can be seen in this scenario as an effector by changing the cellular calcium homeostasis via IP3 and ryanodine receptors as well as increasing the intracellular cyclic AMP concentration and inhibit presynaptic adenosine A1 receptors on parallel fibers, thereby modulating the synaptic input to Purkinje cells.

Since the observed episodic motor impairments in RIM4 mice are very similar to the ataxic attacks of mice carrying mutations in voltage-gated calcium channels, it could be further hypothesized that RIM4 could be involved in intracellular signaling or transport pathways, thereby potentially regulating calcium homeostasis. Furthermore, RIM4 could function in the correct localization, abundance and also kinetics of voltage-gated calcium channels for instance by binding to β-subunits as published previously (Uriu et al., 2010). In general, β-subunits enhance functional voltage-gated calcium channel trafficking to the plasma membrane, modify multiple kinetic properties of these channels and are involved in the association to other proteins (Bichet et al., 2000; Mori et al., 1991; Varadi et al., 1991). This hypothesis would be supported by the cytoplasmic disposition of β-subunits as well as by the finding that RIM3 and RIM4 affect activation kinetics of P/Q-type voltage-gated calcium channels significantly more compared to α-RIMs (Uriu et al., 2010).

A recent study described an involvement of RIM4 in intracellular vesicle trafficking mechanisms important for axonal and dendritic growth. Interestingly, this finding is accompanied by a condensation and reduction of total size of the Golgi apparatus *in vitro* (Alvarez-Baron et al., 2013). RIM4 could be for instance involved in trafficking of post-Golgi vesicles or even the exocytosis of these vesicles to release their cargo into the plasma membrane. Deletion of RIM4 would therefore reduce the trafficking of membrane components, thereby leading to an altered axonal and dendritic structure. Besides the subcellular changes discussed above, the structural alterations could be another reason of the occurrence of the episodic motor impairments in constitutive RIM4 KO and $\text{Pcp2}_{\text{Mpin}}\text{-Cre}_{\text{tg}}\text{:RIM4}^{\text{fl/fl}}$ mice.

Summarizing, the *in vivo* single unit recordings could identify that the deletion of RIM4 in cerebellar Purkinje cells leads to a reduced but more regular firing of the cerebellar network during the dystonic phase of the episodically occurring motor impairments. Thereby pointing towards potential roles of RIM4 in subcellular processes involved in calcium channel localization or function, calcium homeostasis and vesicle trafficking mechanisms. Nevertheless, it is possible that the underlying mechanism of the episodic motor impairments in RIM4 KO mice is not solely related to changes in P/Q-type voltage-gated calcium channels but more complex. The fact that in Purkinje cells P/Q-type voltage-gated calcium channels co-cluster for instance with voltage- and calcium-dependent potassium channels (BK and SK2 channels) suggests a potential additional involvement of these channels (Indriati et al., 2013; Womack et al., 2004).

8.6 SRPK2 abundance mildly influences synaptic and extrasynaptic ELKS clusters

Neurons can adjust their presynaptic neurotransmitter release to changes in neuronal activity, thereby keeping synaptic transmission in a physiological range. This presynaptic homeostatic plasticity has been shown to be regulated via posttranslational modifications of proteins involved in synaptic release. Such a posttranslational modification is for example the phosphorylation of a protein. Studies in *Drosophila* mutants identified Bruchpilot, the homolog of ELKS being phosphorylated by SRPK79D, the homolog of SRPK2 (Johnson et al., 2009; Nieratschker et al., 2009). More recently, co-immunoprecipitation experiments in murine neuronal cells suggested RIM1 and to a lesser extend ELKS as being phosphorylated by SRPK2 (Julia Betzin Ph.D. Thesis; Müller, Betzin et al., 2022). In our study, we wanted to investigate if the presynaptic ELKS abundance changes in the presence of SRPK2, thereby obtaining an indirect read-out of a potential interaction of ELKS with this kinase (chapter 4.8.6).

Super-resolution imaging using the dSTORM method revealed that synaptic ELKS localizations were significantly decreased when SRPK2 was knocked-down in cortical neurons, whereas all other investigated parameters such as ELKS cluster count per synapse as well as cluster area and density remained unchanged (Figure 7.1). These results indicate that the absence of SRPK2 probably influences the number of ELKS molecules per synapse whereas the increased presence of SRPK2 does not lead to an increase in synaptic ELKS molecules. In contrast, overexpression of SRPK79D in *Drosophila* disrupts synaptic Bruchpilot by perturbing T-bar assembly or organization (Johnson et al., 2009), indicating differences in the mode of action between SRPK79D and SRPK2. The effect of SRPK2 on mammalian cells appears small because the number of ELKS clusters remained unchanged in presence or absence of SRPK2. In addition, previously performed immunocytochemistry experiments in primary hippocampal cultures showed no regulation of synaptic ELKS by SRPK2 (Julia Betzin Ph.D. Thesis). These results point towards a minor stabilizing effect of ELKS molecules by SRPK2, potentially via phosphorylation. ELKS proteins are part of the presynaptic active zone and bind to several other active zone components such as voltage-gated calcium channels, RIM1/2 and Munc13 (Ohtsuka et al., 2002; Wang et al., 2009; Wang et al., 2002). The minor effect of SRPK2 on synaptic ELKS molecules could be due to other presynaptic kinases which are involved in the phosphorylation of CAST/ELKS. A recent study identified serine/threonine kinase SAD-B to phosphorylate CAST in rat brain as well as sympathetic neurons and showed that phosphorylated CAST is tightly associated with active zones (Hamada and Ohtsuka, 2018; Mochida et al., 2016). Furthermore, a genomic and proteomic analyses revealed more than 600 protein kinases in humans, however neither all of them would be expressed in brain tissue nor at synapses (Manning et al., 2002). These results corroborate that potentially not only one kinase is responsible for the phosphorylation of synaptic proteins upon changes in neuronal activity. In addition, other known presynaptically active protein kinases are for instance protein kinase A (PKA) or Calcium/calmodulin-dependent protein kinase II (CaMKII; (Engholm-Keller et al., 2019; Nguyen and Woo, 2003; Soderling, 2000). Thus, there is a high likelihood that other kinases apart from SRPK2 phosphorylate ELKS and thereby influence its synaptic abundance.

Experiments in *Drosophila* showed an accumulation of Bruchpilot in axons in absence of SRPK79D (Johnson et al., 2009; Nieratschker et al., 2009). Therefore, a potential influence of SRPK2 on extrasynaptic ELKS clusters was investigated here for the first time in mammalian neurons. Extrasynaptic ELKS localizations, the ELKS cluster count per acquisition and the ELKS cluster area remained unchanged. Only the ELKS cluster density was significantly decreased in the presence of SRPK2 (Figure 7.2). In addition, the synaptic and extrasynaptic ELKS cluster distribution remained unchanged (Figure 7.3). These results point out that the influence of SRPK2 on extrasynaptic ELKS clusters is very small in mammalian neurons compared to Bruchpilot in *Drosophila* and does not lead to an accumulation of ELKS clusters in axons. The significant reduction in ELKS cluster density could be a result of SRPK2 expression repressing other physiologically active kinases active at extrasynaptic sites, thereby destabilizing ELKS clusters. However, the effects appeared small because other investigated parameters were not changed.

There are several potential reasons why our results do not reflect the results obtained in the *Drosophila* studies. The studies by Nieratschker et al. and Johnson et al. were performed in neuromuscular junctions which potentially provide a different molecular background compared to the murine primary cortical neurons used in this study (Johnson et al., 2009; Nieratschker et al., 2009). Furthermore, it has been shown that the amino acid sequence of Bruchpilot has a homology to mammalian ELKS of up to 67% in the N-terminus of the protein. However, for the large coiled-coil rich C-terminus, no direct vertebrate homolog could be detected (Wagh et al., 2006). Moreover, SRPK79D and SPRK2 share only 54% sequence homology (Nieratschker et al., 2009). A recent study identified several SRPK79D phosphorylation sites of Bruchpilot (Driller et al., 2019). However, these phosphorylation sites have been shown to be not regulated by SRPK2 in mammalian cells. In addition, only 3 phosphorylation sites were detected for ELKS in contrast to 15 in Bruchpilot (Julia Betzin, Ph.D. Thesis). These data underline the differences between *Drosophila* and mammalian neurons and could explain the distinct results regarding Bruchpilot and ELKS localizations.

In mammalian neuronal and non-neuronal cell lines it has been shown that SRPK2 is involved in the regulation of CAST1/ERC2 oligomerization via the CC1 and CC4 domains by reducing aggregates of the protein (Arancibia et al., 2019). In contrast in the here presented experiments, an increase in extrasynaptic or synaptic ELKS cluster area could not be detected in absence of SRPK2 (Figure 7.1, Figure 7.2). In addition, ELKS cluster distribution remained unchanged (Figure 7.3). One potential reason for these diverging results could be the usage of different antibodies. In our study we used the ERC1b/2 antibody (Synaptic Systems) which was directed against the amino acids 939 to 948 from rat ERC1b, located at the C-terminal end of the protein (Uniprot-ID: Q811U3). Whereas, the CAST/ERC1 antibody used by Arancibia et al. was self-produced and directed against the amino acids 107 to 138 of the rat protein in the more N-terminal part. The different epitopes could influence the binding affinity of the antibodies and therefore also indirectly influence the fluorescence intensities of the secondary antibodies. Furthermore, the experiments performed by Arancibia et al. were carried out in HEK293T and in the human derived SH-SY5Y neuroblastoma cells, both being common cell lines for expression studies due to their relatively easy cultivation and proliferation. In contrast, the experiments performed in this study were carried out in primary neuronal cultures from murine cortical tissue, representing a more physiological model compared to the previously mentioned cell lines. Also, the differences in expression systems could lead to the alternating results.

Furthermore, co-immunoprecipitation experiments showed that SRPK2 and CAST1/ERC2 are present in a molecular complex, indicating a potential direct interaction of both proteins (Arancibia et al., 2019). This study further supports the hypothesis that SRPK2 interacts with ELKS at mammalian synapses but could not directly show if the reduction of CAST/ELKS oligomers by SRPK2 would also take place at synapses.

In conclusion, the interaction between SRPK2 and ELKS at synapses as well as in extrasynaptic areas appears smaller than it has been shown for SPRK2 and RIM1 (Müller, Betzin et al., 2022). Other kinases might be more important for the interaction and potentially phosphorylation and stabilization of ELKS molecules, thereby responding to alterations in neuronal activity and synaptic plasticity.

9 Summary

The newly generated conditional and constitutive knockout mouse lines provided a physiological environment for the functional analyses of RIM4 and to a minor extend RIM3 in neuronal circuits. In this study we could identify RIM4 as a novel candidate involved in cerebellar signal generation and transduction.

The selective KO of RIM4 in cerebellar Purkinje cells of mice led to episodic motor impairments as well as a reduction in body weight similarly observed in constitutive RIM4 KO mice. Using these Purkinje cell-specific RIM4 KO mice for *in vivo* tetrode recordings we showed that the cerebellar network activity is changed during the ataxia-like episodic motor impairments occurring in these mice.

In addition to previously published results, high RIM4 expression could be detected in the inferior olive, as a part of the brain stem and highly connected to cerebellar Purkinje cells, further pointing towards an involvement of RIM4 in cerebellar signaling mechanisms and in turn the generation of movement. Furthermore, cell culture experiments unveiled that *Rims4* gene expression is regulated in an activity-dependent manner, which indicates an activity dependent functional mechanism of RIM4 in excitatory neurons. Surprisingly, the transcriptome and proteome of murine cerebellar and cortical tissue was not altered upon RIM4 deletion.

Combining all these information one could hypothesize that RIM4 could be involved in subcellular processes participating in voltage-gated channel localization or function, calcium homeostasis or vesicle trafficking mechanisms, thereby shaping cerebellar information processing and output. However, further experiments should be performed to unravel the cellular mechanism by which RIM4 is regulating Purkinje cell activity and thereby influencing the cerebellar network and in turn the motor output.

Independent of RIM4 function, we could show that the presynaptic kinase SRPK2 interacts with ELKS to a lesser extend as it has been shown for RIM1, thereby modulating the synaptic ultrastructure.

10 Outlook

Further experiments are needed to answer the questions which are raised by the results obtained in the here presented study.

On a molecular level, the dSTORM technique would be a tool to unravel mechanistic features of RIM3 and RIM4 on a nanoscale level. However, the approach would include the precise labelling of RIM3 or RIM4 and for instance voltage-gated calcium channels in order to understand their subcellular co-localization. To date, the antibody labelling of both proteins remains challenging and for more precise dSTROM studies, a very small fluorescent tag would be preferable. Additionally, it is still not clear how RIM4 influences synaptic scaling mechanisms or other cellular processes involved in neuronal signaling. For further investigations a single-cell RNAseq approach could be useful to identify clusters of cells expressing a defined subset of genes upon RIM4 deletion.

Apart from the molecular function of RIM4, it would be important to know if RIM4 could be involved in the generation of ataxias, maybe even in human patients with episodic ataxia type 2. The generation of $Pcp2_{Mpin}$-Cre_{tg}:$RIM4^{fl/fl}$ identified cerebellar Purkinje cells as one of the main cell types with functional relevance of RIM4. In order to further characterize the episodic motor impairments of the $Pcp2_{Mpin}$-Cre_{tg}:$RIM4^{fl/fl}$ mice, behavioral tests would give further insights into the defects in motor coordination of these mice which are caused by the deletion of RIM4 in cerebellar Purkinje cells. Furthermore, EMG recordings could reveal potential muscular alterations of $Pcp2_{Mpin}$-Cre_{tg}:$RIM4^{fl/fl}$ mice during the episodically occurring motor impairments and could provide further information about a potential relation to human ataxia. In addition, rescue experiments could help to unravel the functional relevance of RIM4 in the generation of the episodically occurring motor impairments. In *tottering* mice, the administration of L-type calcium channel blocker intracerebroventricularly and subcutaneously significantly reduced the induction of ataxia-like attacks, suggesting that L-type calcium channels are upregulated in these mice in response to the induced mutation in P/Q-type calcium channels (Campbell and Hess, 1999). Furthermore, the direct injection of a SK channel activator into the cerebellum of *tottering* mice restored the regularity of Purkinje cell activity during ataxia-like attacks (Tara et al., 2018). Similar experiments could be performed in $Pcp2_{Mpin}$-Cre_{tg}:$RIM4^{fl/fl}$ mice, maybe even in an *in vivo* setup. In order to further characterize potential changes in intracellular calcium homeostasis, an *in vivo* calcium imaging approach would be feasible.

In addition to the results obtained for RIM4, the results of the experiments in constitutive RIM3 KO mice suggest a potentially different functional mechanism of RIM3, already by its high expression levels in murine thalamic tissue. The loss of RIM3 in constitutive RIM3 KO mice would need further investigations mainly in regard to a potential schizophrenia-related phenotype of these mice. It has been shown that RIM3 together with Piccolo and RIM2 is up-regulated in the amygdala of schizophrenia patients (Weidenhofer et al., 2006). Therefore, for instance behavioral test could help to identify a potential schizophrenia-like behavior in these mice.

11 Appendix

11.1 Breeding and genotyping of RIM3 and RIM4 KO mouse lines

Constitutive RIM3 KO as well as constitutive RIM3 KO 1st mouse lines were bred such that most effectively offspring with WT and KO genotypes were generated. Therefore, a homozygous RIM3 KO mouse was mated with a heterozygous RIM3 mouse. This breeding scheme was applied for the constitutive RIM3 KO and the constitutive RIM3 KO 1st mouse strains.

All RIM4 KO mouse strains used in this study have in common, that they develop episodically occurring motor impairments. Since this phenotype dramatically impairs the RIM4 KO mice in their normal behavior, it was only allowed to breed these strains in a heterozygous manner. For RIM4const KO as well as constitutive RIM4 KO 1st mouse strains this would result in 25% of offspring carrying the RIM4 KO allele homozygously. According to Luo et al., 2020 the conditional Cre-driver mouse line B6.129-Tg(Pcp2-cre)2Mpin/J obtains a 14-84% probability of germline recombination, depending on the exact targeting gene locus if the male mouse carries the Cre recombinase. In order to prevent germline recombination in the newly generated $Pcp2_{Mpin}$-Cre_{tg}:$RIM4^{fl/fl}$ mice, male $RIM4^{fl/fl}$ mice without Cre recombinase expression were mated with heterozygous $Pcp2_{Mpin}$-Cre_{tg}:$RIM4^{fl/+}$ mice. In turn, 50% of the offspring of these breedings would express the Cre recombinase under the Pcp2-promotor. Thereby leading to a Purkinje cell-specific RIM4 KO in these mice.

To further verify that only RIM3 and RIM4 mice carrying the correct genotype were used for experiments, the following genotyping protocol was applied for all RIM3 and RIM4 KO mouse lines with the exception that Cre recombinase expression was not verified in constitutive RIM3 KO^{1st} and constitutive RIM4 KO^{1st} mouse lines:

For all genotyping reactions DNA extracted from tail cuts or ear punches of the mice was used. DNA was extracted by a standard column-based protocol of DNA isolation kits (e.g. provided by Sigma Aldrich). Three different PCR reactions were performed, each with individual primer pairs and PCR reactions (Figure 11.1; Table 6).

1. Reaction - WT/flox reaction: In this reaction the primer pairs g0006 (RIM3 5’arm) and g0008 (RIM3 3’arm) or g0018 (RIM4 5’arm) and g0019 (RIM4 3’arm) were used for amplification. The annealing temperature in the PCR reaction was set to 58°C. The resulting PCR products are mentioned in Table 6.

2. Reaction - WT/flox/rec reaction: In this reaction the primer g0006 (RIM3 5’arm) and g0014 (RIM3 rev01) or g0018 (RIM4 5’arm) and g0023 (RIM4 rev01) were used for amplification. The annealing temperature for the PCR reaction was set to 60°C. The resulting PCR products could have three different sizes, depending on the recombination status of the RIM3-floxed or RIM4-floxed alleles. See Table 6 for further details.
3. Reaction - Cre reaction: In this reaction the primer g0070 (‘Cre forward’) and g0071 (‘Cre reverse’) were used for amplification. The annealing temperature for the PCR reaction was set to 60°C. If Cre recombinase was present in the tissue, the resulting PCR product had a size of 454 bp. Tissues without Cre recombinase showed no PCR products in this reaction.

Table 6: Genotyping primer pairs for knock-out mouse lines.

Gene	ID	Primer sequences (5’-3’)	Resulting band sizes	
Rims3	g0006 g0008	GGACCACACTGCAATGCTAA ACCAGACTCCAAAGCCCTCT	WT Flox	324 bp 485 bp
	g0006 g0014	GGACCACACTGCAATGCTAA GTGAGTAATGGGAGGCAGGA	WT Flox Recombined	1000 bp 1288 bp 472 bp
Rims4	g0018 g0019	GCATGATGGGAAGGAATGCCAAGC GTTCAGGCCAGGGCTTCTCCATGC	WT Flox	324 bp 494 bp
	g0018 g0023	GCATGATGGGAAGGAATGCCAAGC CCCACTTTGAGTGTGGGTCT	WT Flox Recombined	1000 bp 1288 bp 472 bp
Cre recombinase	g0070 g0071	CATTTGGGCCAGCTAAACAT CCCGGCAAAACAGGTAGTTA	Cre pos.	454 bp

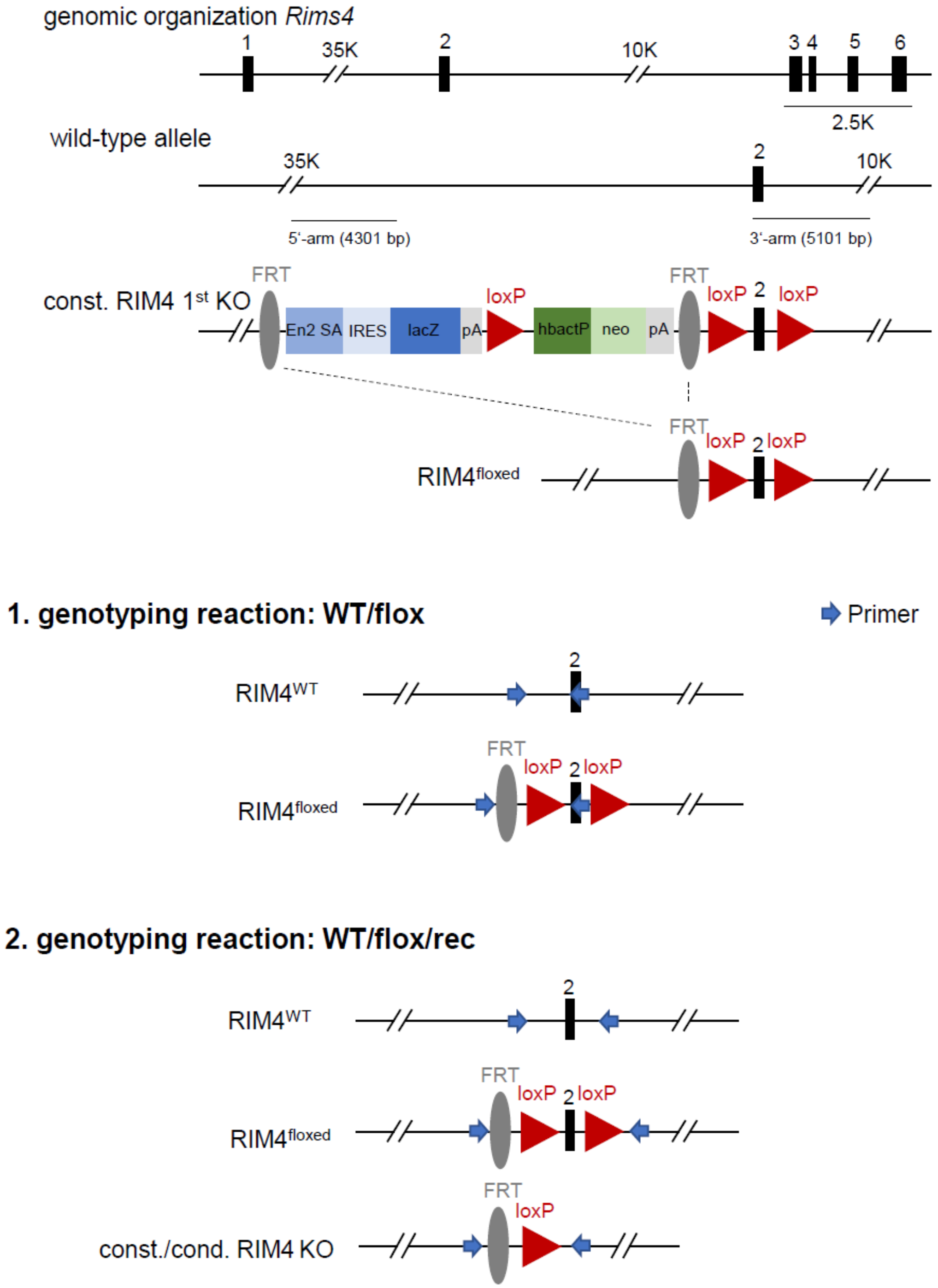

Figure 11.1: Genotyping strategy for RIM4 KO mouse lines. Insertion of a LacZ splice acceptor cassette in between exon 1 and 2 introduces splicing of RIM4 after exon 1 and causes disruption of normal protein expression (constitutive RIM4 KO 1st). FLP-mediated recombination leads to the excision of the splice acceptor cassette and reconstitutes normal RIM4 protein expression (RIM4floxed). Cre recombinase-mediated recombination results in the excision of exon 2 and thereby abolishes RIM4 protein expression (constitutive/conditional RIM4 KO). Locations of primer pairs used in the 1st and 2nd genotyping reaction are depicted by blue arrows (adapted from Katrin Michel, Ph.D. Thesis).

The following mastermix composition was used for all 3 PCR reactions:

Table 7: Mastermix composition for genotyping PCR reactions.

Component	Volume
EconoTaq PLUS GREEN 2x Master Mix	5 µl
5’ primer	1 µl (1:10 dilution of stock; 1 µM)
3’ primer	1 µl (1:10 dilution of stock; 1 µM)
Water	2 µl
gDNA (concentration not determined)	1 µl

The following PCR conditions were used for the individual reactions:

Table 8: PCR conditions for genotyping.

	WT/flox reaction	WT/flox/rec reaction	Cre reaction
	95 °C for 5 min		
35 cycles	95°C 40 sec 58°C 50 sec 72°C 90 sec	95°C 40 sec 60°C 50 sec 72°C 90 sec	95°C 40 sec 60°C 50 sec 72°C 90 sec
	72°C for 10 min		
	4°C		

After successful amplification, PCR products were size-separated on a 1.5% agarose gel together with a 1kb ladder (Thermo Fisher) to correlate sizes of the resulting bands. GelGreen DNA stain was to visualize bands on the gel by UV light illumination.

For the Purkinje cell-specific RIM4 KO mouse line, a specific interpretation of genotyping results was needed. In an ideal case, Cre recombinase expression under the Pcp2-promotor would only appear in cerebellar Purkinje cells and would not be visible in DNA from tail cuts or ear punches. However, a faint band for the recombined RIM4 allele was visible in most of the genotyping PCR of Pcp2$_{\mathrm{Mpin}}$-Cre$_{\mathrm{tg}}$:RIM4$^{\mathrm{fl/fl}}$ mice. This was probably due to an already earlier described leakage of the Pcp2-promotor (Barski et al., 2000). In order to discriminate between a potential germline-recombination and the smaller fraction of Pcp2-promotor leakage, Hyuntae Kim, AG Dietrich, University Clinic Bonn established a thresholding method for the interpretation of genotyping results for this specific mouse line. Thereby the fluorescence intensity of the floxed-band was compared against the fluorescence intensity of the recombined band in genotyping reaction 2. If the ratio floxed vs. recombined band was smaller than 0.2, the genotype of the mouse was interpreted as Pcp2$_{\mathrm{Mpin}}$-Cre$_{\mathrm{tg}}$:RIM4$^{\mathrm{fl/fl}}$. Mice carrying allele ratios greater than 0.2 were discarded and not used for experiments or breedings since it could not be ruled out that a strong Cre recombinase expression outside Purkinje cells is taking place.

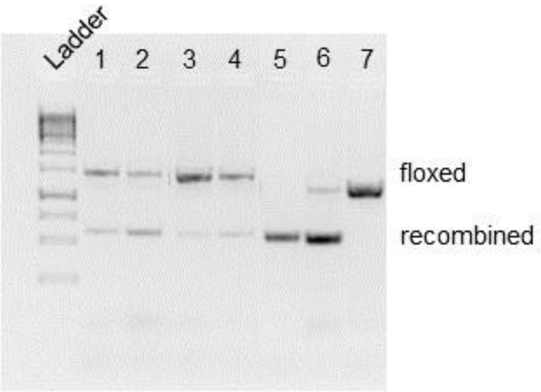

Figure 11.2: Example of genotyping results for reaction 2. Amplification products of mice 1-4 show weak recombined bands, whereas mouse 6 shows strong recombination of the RIM4 KO alleles. Mouse 5 is a RIM4const KO as control obtaining no floxed RIM4 allele and mouse 7 is a RIM4$^{\mathrm{fl/fl}}$ control.

11.2 List of antibodies and primers for molecular biological methods

Primers for quantitative real-time RT-PCR

Table 9: Oligonucleotide primer pairs for quantitative real-time RT-PCR reactions.

Gene	ID	Primer sequences (5'-3')
β-actin	q0095	ACCGTGAAAAGATGACCCAGA
	q0096	ATGGGCACAGTGTGGGTGA
Rims1α	q0787	CCTCCCCCTATGCAAGAACT
	q0788	TTCCTCCTCTTCCTTCTGCC
Rims1 total	q0848	CCGACGTGTGGAATCTGTCA
	q0849	CACAGCGTGCACAGAACTTG
Rims2α	q0813	CTCTCAACCTCCTCCGCAG
	q0814	TGACGATCCATGACAGCCAG
Rims2 total	q0832	AGATGGCAGCATGAACAGCT
	q0833	CCAGGCCATCCAGGAAATCA
Rims2γ	q0795	AGCCTCTCTGCCTCTTTTGA
	q0796	GAACAGTGCTCCGTAGCTTTT
Rims3	q0894	TAACGGGGAGCCTGGTCC
	q0895	CAGCTTGCTGGGATCCACA
Rims4	q0799	CTCGCCATCTACTTCCCGT
	q0800	CCCTGTCTCTGTGCTTCTCT

Antibodies for immunohistochemistry

Table 10: Primary antibodies used for immunohistochemical stainings.

Protein	Species	Concentration	Company	Catalog No.
RIM3	Rabbit	1:100	Pineda Antibody Service	Animal 3
mGluR1	Rabbit	1:500	Frontier Institute	AB-2571799
Calbindin	mouse	1:500	Swant	D-28K
KCND3	Rabbit	1:500	Abcam	Ab65794

Antibodies for immunoblotting

Table 11: Primary antibodies for immunoblot stainings.

Protein	Species	Concentration	Company	Catalog No.
β-Actin	Mouse	1:10000	abcam	ab6276
GRIP	Mouse	1:500	BD Biosciences	611319
Liprin-α3	Rabbit	1:1000	Self-made (Zürner et al., 2011)	
Munc13-1	Mouse	1:500	Synaptic Systems	126111
Munc18-3	Rabbit	1:500	Synaptic Systems	116202
PSD95	Mouse	1:500	Millipore	MAB1598
RIM1	Rabbit	1:500	Synaptic Systems	140023
RIM3	Rabbit	1:50	Pineda Antibody Service	Animal 3
RIM4	Rabbit	1:50	Pineda Antibody Service	Animal 2
SNAP25	Rabbit	1:500	Synaptic Systems	111002
Syt-1	Mouse	1:500	Synaptic Systems	105011
VAMP2	Mouse	1:500	Synaptic Systems	104211

11.3 dSTORM setup

Antibodies for dSTORM immunocytochemical stainings

Table 12: Antibodies for channel crosstalk analysis.

Primary antibody	Species	Concentration	Company	Catalog No.
Bassoon	Mouse	1:10000	Enzo LifeSciences	SAP7F407

Secondary antibody	Species	Concentration	Company	Catalog No.
α-mouse-Alexa488	Goat	1:200	Invitrogen	A-28175
α-mouse-Alexa532	Goat	1:200	Invitrogen	A-11002
α-mouse-Alexa647	Goat	1:200	Invitrogen	A-21236

Table 13: Antibodies for 3D dSTORM imaging of synapses.

Primary antibody	Species	Concentration	Company	Catalog No.
Bassoon	Mouse	1:500	Enzo LifeSciences	SAP7F407
Homer1	Guinea pig	1:1000	Synaptic Systems	160004

Secondary antibody	Species	Concentration	Company	Catalog No.
α-mouse-Alexa488	Goat	1:200	Invitrogen	A-28175
α-guinea pig-Alexa647	Goat	1:200	Invitrogen	A-21450

Table 14: Antibodies for ELKS cluster analysis.

Primary antibody	Species	Concentration	Company	Catalog No.
ERC1b/2	Rabbit	1:1000	Synaptic Systems	140003
Synapsin1/2	Guinea pig	1:3000	Synaptic Systems	106004

Secondary antibody	Species	Concentration	Company	Catalog No.
α-Cy3	Donkey	1:400	Jackson ImmunoResearch	706-165-148
α-rabbit-Alexa647	Goat	1:200	Invitrogen	A-21244

Filter details

Table 15: Excitation filter properties.

488nm single filter	532nm single filter	642nm single filter	Quad filter
400-410 nm	400-410 nm	400-410 nm	397-413 nm
483-493 nm	527-537 nm	637-647 nm	483-493 nm
			527-537 nm
			635-645 nm

Table 16: Emission filter properties.

488nm single filter	532nm single filter	642nm single filter	Quad filter
500-600 nm	550-650 nm	660-760 nm	419-475 nm
			499-521 nm
			550-620 nm
			665-725 nm

12 List of Abbreviations

A

AF488	Alexa fluor 488
AF532	Alexa fluor 532
AF647	Alexa fluor 647
AHP	After-hyperpotential
AMP	Adenosine monophosphate
AMPA	α-amino-3-hydroxy-5-methyl-4-isoxazolepropionic acid

B

BK channel	Large conductance voltage- and Ca^{2+}-activated K^{+} channel
BME	Basal Medium Eagle
BSA	Bovine serum albumin

C

cAMP	Cyclic adenosine monophosphate
CaMKII	Calcium/calmodulin-dependent protein kinase II
CAZ	Cytomatrix at the active zone
CB	Cerebellum
cDNA	Complementary desoxyribonucleic acid
CID	Collision induced dissociation
CoV	Coefficient of variation
CX	Cortex

D

DAPI	4’,6-Diamidin-2-phenylindol

D

DIV	Days in vitro
DKO	Double knock-out
DNA	Desoxyribonucleic acid
dSTORM	Direct stochastic optical reconstruction microscopy
DTT	Dithiothreitol
DG	Dentate gyrus

E

EA2	Episodic ataxia type 2
EDTA	Ethylene diamine tetraacetic acid
EGTA	Ethylene glycol tetraacetic acid
EIB-18	16-channel electrode interface board
ELKS	Protein rich in the amino acids E (glutamic acid), L (leucine), K (lysine), S (serine)
EMG	Electromyography
EPSC	Excitatory postsynaptic current

F

FA	Formic acid
FC	Fold change
Flp	Flippase

G

GABA	Gamma-aminobutyric acid
GluD2	Glutamate receptor delta type 2
GPCR	G-protein coupled receptor
GWAS	Genome-wide association studies

H

HC	Hippocampus
HCD	Higher energy collision induced dissociation

I

IP3	Inositol 1,4,5-trisphosphate
ISH	*In-situ* hybridization
ISI	Inter-spike interval

K

KO	Knock-out
KO 1st	Knock-out first
KOMP	Knock-out mouse project consortium

L

LFP	Local field potential
LTD	Long-term depression

M

MEA	β-mercaptoethylamine
MEM	Minimal Essentail Medium
mEPSC	Miniature excitatory postsynaptic current
MGI	Mouse genome informatics
mGluR1	Metabotropic glutamate receptor 1
MR-1	Myofibrillogenesis regulator 1
mRNA	Messenger ribonucleic acid

N

N.A.	Numerical aperture
NaF	Sodium fluoride
NMR	Nuclear magnetic resonance
NGS	Next generation sequencing

O

OCT	Optimal cutting temperature compound

P

PBS	Phosphate-buffered saline
PBST	Phosphate-buffered saline + 0.1% Triton-X100
PBT	Phosphate-buffered saline + 0.1% Tween20
PC	Principal component
PCA	Principal component analysis
PCR	Polymerase chain reaction
Pcp2	Purkinje-cell protein 2
PES	Polyethersulfone
PFA	Paraformaldehyde
PIP_2	Phosphatidylinositol 4,5-bisphosphate
PKA	Protein kinase A
PMSF	Phenylmethylsulfonyl fluoride

P

PNKD	Paroxysmal nonkinesigenic dyskinesia
PVDF	Polyvinylidene difluoride

Q

qRT-PCR	Quantitative real-time polymerase chain reaction

R

RIM	Rab3A-interacting molecule
RIM-BP	RIM-binding protein
RNA	Ribonucleic acid
ROI	Region of interest
RORα	Retinoid-related orphan receptor alpha

S

SCA	Spinocerebellar ataxia
SDC	Sodium deoxycholate
SDS	Sodium dodecyl sulfate
SDS-PAGE	Sodium dodecyl sulfate polyacrylamide gel electrophoresis
SRPK2	Serine-arginine protein kinase 2
STED	Stimulated emission depletion microscopy
SuMo	Suppressed motion stage

T

TEAB	Triethylammonium bicarbonate buffer

T

TFA	Trifluoroacetic acid
TH	Thalamus
TIRF	Total internal fluorescence
TRIS	Tris(hydroxymethyl)amino methane
TTX	Tetrodotoxin

W

WT	Wildtype

13 References

Aiba, A., Chen, C., Herrup, K., Rosenmund, C., Stevens, C. F., & Tonegawa, S. (1994). Reduced hippocampal long-term potentiation and context-specific deficit in associative learning in mGluR1 mutant mice. *Cell*, *79*(2), 365–375.

Alvarez-Baron, E., Michel, K., Mittelstaedt, T., Opitz, T., Schmitz, F., Beck, H., … Schoch, S. (2013). RIM3 and RIM4 are key regulators of neuronal arborization. *Journal of Neuroscience*, *33*(2), 824–839.

Alviña, K., & Khodakhah, K. (2010a). K Ca channels as therapeutic targets in episodic ataxia type-2. *Journal of Neuroscience*, *30*(21), 7249–7257.

Alviña, K., & Khodakhah, K. (2010b). The therapeutic mode of action of 4-aminopyridine in cerebellar ataxia. *Journal of Neuroscience*, *30*(21), 7258–7268.

Arancibia, D., Lira, M., Cruz, Y., Barrera, D. P., Montenegro-Venegas, C., Godoy, J. A., … Torres, V. I. (2019). Serine–arginine protein kinase SRPK2 modulates the assembly of the active zone scaffolding protein CAST1/ERC2. *Cells*, *8*(11), 1333.

Arancillo, M., White, J. J., Lin, T., Stay, T. L., & Sillitoe, R. V. (2015). In vivo analysis of Purkinje cell firing properties during postnatal mouse development. *Journal of Neurophysiology*, *113*(2), 578–591.

Bagur, R., & Hajnóczky, G. (2017). Intracellular Ca2+ sensing: role in calcium homeostasis and signaling. *Molecular Cell*, *66*(6), 780–788.

Barclay, J., Balaguero, N., Mione, M., Ackerman, S. L., Letts, V. A., Brodbeck, J., … Rees, M. (2001). Ducky mouse phenotype of epilepsy and ataxia is associated with mutations in the Cacna2d2 gene and decreased calcium channel current in cerebellar Purkinje cells. *Journal of Neuroscience*, *21*(16), 6095–6104.

Barski, J. J., Dethleffsen, K., & Meyer, M. (2000). Cre recombinase expression in cerebellar Purkinje cells. *Genesis*, *28*(3–4), 93–98.

Basson, M. A., & Wingate, R. J. (2013). Congenital hypoplasia of the cerebellum: Developmental causes and behavioral consequences. *Frontiers in Neuroanatomy*, *7*(29), 1–16.

Bates, M., Blosser, T. R., & Zhuang, X. (2005). Short-range spectroscopic ruler based on a single-molecule optical switch. *Physical Review Letters*, *94*(10), 108101.

Bates, M., Huang, B., Dempsey, G. T., & Zhuang, X. (2007). Multicolor super-resolution imaging with photo-switchable fluorescent probes. *Science*, *317*(5845), 1749–1753.

Bates, M., Huang, B., & Zhuang, X. (2008). Super-resolution imaging by nanoscale localization of photo-switchable fluorescent probes. *Current Opinion in Chemical Biology*, *12*(5), 505–514.

Becker, E. B. E. (2014). The Moonwalker mouse: New insights into TRPC3 function, cerebellar development, and ataxia. *Cerebellum*, *13*(5), 628–636.

Benedetti, B., Benedetti, A., & Flucher, B. E. (2016). Loss of the calcium channel β4 subunit impairs parallel fibre volley and Purkinje cell firing in cerebellum of adult ataxic mice. *European Journal of Neuroscience*, *43*(11), 1486–1498.

Betz, A., Thakur, P., Junge, H. J., Ashery, U., Rhee, J.-S., Scheuss, V., … Brose, N. (2001). Functional interaction of the active zone proteins Munc13-1 and RIM1 in synaptic vesicle priming. *Neuron*, *30*(1), 183–196.

Bichet, D., Cornet, V., Geib, S., Carlier, E., Volsen, S., Hoshi, T., … De Waard, M. (2000). The I-II loop of the Ca2+ channel α1 subunit contains an endoplasmic reticulum retention signal antagonized by the β subunit. *Neuron*, *25*(1), 177–190.

Blundell, J., Kaeser, P. S., Südhof, T. C., & Powell, C. M. (2010). RIM1α and interacting proteins involved in presynaptic plasticity mediate prepulse inhibition and additional behaviors linked to schizophrenia. *Journal of Neuroscience*, *30*(15), 5326–5333.

Burgess, D. L., Jones, J. M., Meisler, M. H., & Noebels, J. L. (1997). Mutation of the Ca2+ channel beta subunit gene Cchb4 is associated with ataxia and seizures in the lethargic (lh) mouse. *Cell*, *88*(3), 385–392.

Burgess, D. L., & Noebels, J. L. (1999). Single gene defects in mice: The role of voltage-dependent calcium channels in absence models. *Epilepsy Research*, *36*(2–3), 111–122.

Campbell, D. B., & Hess, E. J. (1996). Chromosomal localization of the neurological mouse mutations tottering (tg), Purkinje cell degeneration (pcd), and nervous (nr). *Molecular Brain Research*, *37*, 79–84.

Campbell, D. B., & Hess, E. J. (1999). L-type calcium channels contribute to the tottering mouse dystonic episodes. *Molecular Pharmacology*, *55*(1), 23–31.

Campbell, D. B., North, J. B., & Hess, E. J. (1999). Tottering mouse motor dysfunction is abolished on the Purkinje cell degeneration (pcd) mutant background. *Experimental Neurology*, *160*(1), 268–278.

Castillo, P. E., Schoch, S., Schmitz, F., Südhof, T. C., & Malenka, R. C. (2002). RIM1α is required for presynaptic long-term potentiation. *Nature*, *415*(6869), 327–330.

Castillo, P. E., Weisskopf, M. G., & Nicoll, R. A. (1994). The role of Ca2+ channels in hippocampal mossy fiber synaptic transmission and long-term potentiation. *Neuron*, *12*(2), 261–269.

Cendelin, J. (2014). From mice to men: lessons from mutant ataxic mice. *Cerebellum & Ataxias*, *1*, 4.

Chen, X., Kovalchuk, Y., Adelsberger, H., Henning, H. A., Sausbier, M., Wietzorrek, G., …

Konnerth, A. (2010). Disruption of the olivo-cerebellar circuit by Purkinje neuron-specific ablation of BK channels. *Proc Natl Acad Sci U S A*, *107*(27), 12323–12328.

Choi, O. H., Shamim, M. T., Padgett, W. L., & Daly, J. W. (1988). Caffeine and theophylline analogues: Correlation of behavioral effects with activity as adenosine receptor antagonists and as phosphodiesterase inhibitors. *Life Sciences*, *43*(5), 387–398.

Coppola, T., Magnin-Lüthi, S., Perret-Menoud, V., Gattesco, S., Schiavo, G., & Regazzi, R. (2001). Direct interaction of the Rab3 effector RIM with Ca2+ channels, SNAP-25, and synaptotagmin. *Journal of Biological Chemistry*, *276*(35), 32756–32762.

Corbalan-Garcia, S., & Gómez-Fernández, J. C. (2014). Signaling through C2 domains: More than one lipid target. *Biochimica et Biophysica Acta*, *1838*(6), 1536–1547.

Couteaux, R., & Pécot-Dechavassine, M. (1970). Synaptic vesicles and pouches at the level of “active zones” of the neuromuscular junction. *C R Acad Hebd Seances Acad Sci D.*, *271*(25), 2346–2349.

Craig, P. J., McAinsh, A. D., McCormack, A. L., Smith, W., Beattie, R. E., Priestley, J. V., … Volsen, S. G. (1998). Distribution of the voltage-dependent calcium channel alpha(1A) subunit throughout the mature rat brain and its relationship to neurotransmitter pathways. *Journal of Comparative Neurology*, *397*(2), 251–267.

Dani, A., Huang, B., Bergan, J., Dulac, C., & Zhuang, X. (2010). Superresolution imaging of chemical synapses in the brain. *Neuron*, *68*(5), 843–856.

de Jong, A. P. H., Roggero, C. M., Ho, M.-R., Wong, M. Y., Brautigam, C. A., Rizo, J., & Kaeser, P. S. (2018). RIM C2B domains target presynaptic active zone functions to PIP2-containing membranes. *Neuron*, *98*(2), 335–349.

De Zeeuw, C. I., Simpson, J. I., Hoogenraad, C. C., Galjart, N., Koekkoek, S. K. E., & Ruigrok, T. J. H. (1998). Microcircuitry and function of the inferior olive. *Trends in Neurosciences*, *21*(9), 391–400.

Dietrich, D., Kirschstein, T., Kukley, M., Pereverzev, A., von der Brelie, C., Schneider, T., & Beck, H. (2003). Functional specialization of presynaptic Cav2.3 Ca2+ channels. *Neuron*, *39*(3), 483–496.

Dieudonné, S., & Dumoulin, A. (2000). Serotonin-driven long-range inhibitory connections in the cerebellar cortex. *Journal of Neuroscience*, *20*(5), 1837–1848.

Dixon, A. K., Gubitz, A. K., Sirinathsinghji, D. J. S., Richardson, P. J., & Freeman, T. C. (1996). Tissue distribution of adenosine receptor mRNAs in the rat. *British Journal of Pharmacology*, *118*(6), 1461–1468.

Dobin, A., Davis, C. A., Schlesinger, F., Drenkow, J., Zaleski, C., Jha, S., … Gingeras, T. R.

(2013). STAR: Ultrafast universal RNA-seq aligner. *Bioinformatics*, *29*(1), 15–21.

Donato, R., Page, K. M., Koch, D., Nieto-Rostro, M., Foucault, I., Davies, A., … Dolphin, A. C. (2006). The ducky2J mutation in Cacna2d2 results in reduced spontaneous Purkinje cell activity and altered gene expression. *Journal of Neuroscience*, *26*(48), 12576–12586.

Driller, J. H., Lützkendorf, J., Depner, H., Siebert, M., Kuropka, B., Weise, C., … Wahl, M. C. (2019). Phosphorylation of the Bruchpilot N-terminus in Drosophila unlocks axonal transport of active zone building blocks. *Journal of Cell Science*, *132*(6), 1–14.

Duarri, A., Lin, M.-C. A., Fokkens, M. R., Meijer, M., Smeets, C. J. L. M., Nibbeling, E. A. R., … Verbeek, D. S. (2015). Spinocerebellar ataxia type 19/22 mutations alter heterocomplex Kv4.3 channel function and gating in a dominant manner. *Cellular and Molecular Life Sciences*, *72*(17), 3387–3399.

Dymecki, S. M. (1996). Flp recombinase promotes site-specific DNA recombination in embryonic stem cells and transgenic mice. *Proc Natl Acad Sci U S A*, *93*(12), 6191–6196.

Engholm-Keller, K., Waardenberg, A. J., Müller, J. A., Wark, J. R., Fernando, R. N., Arthur, J. W., … Graham, M. E. (2019). The temporal profile of activity-dependent presynaptic phospho-signalling reveals longlasting patterns of poststimulus regulation. *PLoS Biology*, *17*(3), 1–46.

Fletcher, C. F., Lutz, C. M., O’Sullivan, T. N., Shaughnessy Jr., J. D., Hawkes, R., Frankel, W. N., … Jenkins, N. A. (1996). Absence epilepsy in tottering mutant mice is associated with calcium channel defects. *Cell*, *87*(4), 607–617.

Frank, C. A., Kennedy, M. J., Goold, C. P., Marek, K. W., & Davis, G. W. (2006). Mechanisms underlying the rapid induction and sustained expression of synaptic homeostasis. *Neuron*, *52*(4), 663–677.

Fromer, M., Pocklington, A. J., Kavanagh, D. H., Williams, H. J., Dwyer, S., Gormley, P., … O’Donovan, M. C. (2014). De novo mutations in schizophrenia implicate synaptic networks. *Nature*, *506*(7487), 179–184.

Gerst, R., & Hölzer, M. (2018). PCAGO: An interactive web service to analyze RNA-Seq data with principal component analysis. *BioRxiv*, *433078*.

Goldowitz, D., & Hamre, K. (1998). The cells and molecules that make a cerebellum. *Trends in Neurosciences*, *21*(9), 375–382.

Green, M., & Sidman, L. (1962). Tottering-a neuromuscular mutation in the mouse. *The Journal of Heredity*, *53*(5), 233–237.

Guan, R., Dai, H., Tomchick, D. R., Dulubova, I., Machius, M., Südhof, T. C., & Rizo, J. (2007). Crystal structure of the RIM1α C2B domain at 1.7 Å resolution. *Biochemistry*, *46*(31), 8988–8998.

Hamada, S., & Ohtsuka, T. (2018). CAST: Its molecular structure and phosphorylation-dependent regulation of presynaptic plasticity. *Neuroscience Research*, *127*, 25–32.

Han, Y., Kaeser, P. S., Südhof, T. C., & Schneggenburger, R. (2011). RIM determines Ca2+ channel density and vesicle docking at the presynaptic active zone. *Neuron*, *69*(2), 304–316.

Hermey, G., Mahlke, C., Gutzmann, J. J., Schreiber, J., Blüthgen, N., & Kuhl, D. (2013). Genome-wide profiling of the activity-dependent hippocampal transcriptome. *PLoS ONE*, *8*(10), e76903.

Heuzé, P., Féron, C., & Baudoin, C. (1997). Early behavioral development of mice is affected by staggerer mutation as soon as postnatal day three. *Brain Res Dev Brain Res.*, *101*(1–2), 81–84.

Hibino, H., Pironkova, R., Onwumere, O., Vologodskaia, M., Hudspeth, A. J., & Lesage, F. (2002). RIM-binding proteins (RBPs) couple Rab3-interacting molecules (RIMs) to voltage-gated Ca2+ channels. *Neuron*, *34*(3), 411–423.

Hills, L. B., Masri, A., Konno, K., Kakegawa, W., Lam, A. T. N., Lim-Melia, E., … Mochida, G. H. (2013). Deletions in GRID2 lead to a recessive syndrome of cerebellar ataxia and tonic upgaze in humans. *Neurology*, *81*(16), 1378–1386.

Hoxha, E., Balbo, I., Miniaci, M. C., & Tempia, F. (2018). Purkinje cell signaling deficits in animal models of ataxia. *Frontiers in Synaptic Neuroscience*, *10*(6), 1–17.

Huang, B., Wang, W., Bates, M., & Zhuang, X. (2008). Three-dimensional super-resolution imaging by stochastic optical reconstruction microscopy. *Science*, *319*(5864), 810–813.

Huber, W., Von Heydebreck, A., Sültmann, H., Poustka, A., & Vingron, M. (2002). Variance stabilization applied to microarray data calibration and to the quantification of differential expression. *Bioinformatics*, *18 Suppl 1*, S96–S104.

Ibata, K., Sun, Q., & Turrigiano, G. G. (2008). Rapid synaptic scaling induced by changes in postsynaptic firing. *Neuron*, *57*(6), 819–826.

Imai, T., Yoshida, T., Baba, M., Nishimura, M., Kakizaki, M., & Yoshie, O. (1996). Molecular cloning of a novel T cell-directed CC chemokine expressed in thymus by signal sequence trap using Epstein-Barr virus vector. *Journal of Biological Chemistry*, *271*(35), 21514–21521.

Indriati, D. W., Kamasawa, N., Matsui, K., Meredith, A. L., Watanabe, M., & Shigemoto, R. (2013). Quantitative localization of Cav2.1 (P/Q-Type) voltage-dependent calcium channels in Purkinje cells: Somatodendritic gradient and distinct somatic coclustering with calcium-activated potassium channels. *Journal of Neuroscience*, *33*(8), 3668–3678.

Iossifov, I., Ronemus, M., Levy, D., Wang, Z., Hakker, I., Rosenbaum, J., … Wigler, M. (2012). De novo gene disruptions in children on the Autistic Spectrum. *Neuron*, *74*(2), 285–299.

Ito, M. (2001). Cerebellar long-term depression: Characterization, signal transduction, and functional roles. *Physiological Reviews*, *81*(3), 1143–1195.

Ito, M. (2002). Historical review of the significance of the cerebellum and the role of Purkinje cells in motor learning. *Annals of the New York Academy of Sciences*, *978*, 273–288.

Ito, M. (2006). Cerebellar circuitry as a neuronal machine. *Progress in Neurobiology*, *78*(3–5), 272–303.

Jarvis, C. I., Staels, B., Brugg, B., Lemaigre-Dubreuil, Y., Tedgui, A., & Mariani, J. (2002). Age-related phenotypes in the staggerer mouse expand the RORα nuclear receptor's role beyond the cerebellum. *Molecular and Cellular Endocrinology*, *186*(1), 1–5.

Jen, J. C., Graves, T. D., Hess, E. J., Hanna, M. G., Griggs, R. C., & Baloh, R. W. (2007). Primary episodic ataxias: Diagnosis, pathogenesis and treatment. *Brain*, *130*(Pt 10), 2484–2493.

Jen, J. C., & Wan, J. (2018). *Episodic ataxias*. *Handbook of Clinical Neurology* (1st ed., Vol. 155). Elsevier B.V.

Johnson, E. L., Fetter, R. D., & Davis, G. W. (2009). Negative regulation of active zone assembly by a newly identified SR protein kinase. *PLoS Biology*, *7*(9), e1000193.

Jung, S., Oshima-Takago, T., Chakrabarti, R., Wong, A. B., Jing, Z., Yamanbaeva, G., … Moser, T. (2015). Rab3-interacting molecules 2α and 2β promote the abundance of voltage-gated CaV1.3 Ca2+ channels at hair cell active zones. *Proc Natl Acad Sci U S A*, *112*(24), E3141–E3149.

Kaeser, P. S., Deng, L., Fan, M., & Südhof, T. C. (2012). RIM genes differentially contribute to organizing presynaptic release sites. *Proc Natl Acad Sci U S A*, *109*(29), 11830–11835.

Kaeser, P. S., Deng, L., Wang, Y., Dulubova, I., Liu, X., Rizo, J., & Südhof, T. C. (2011). RIM proteins tether Ca2+ channels to presynaptic active zones via a direct PDZ-domain interaction. *Cell*, *144*(2), 282–295.

Kaeser, P. S., Kwon, H.-B., Chiu, C. Q., Deng, L., Castillo, P. E., & Südhof, T. C. (2008). RIM1α and RIM1β are synthesized from distinct promoters of the RIM1 gene to mediate differential but overlapping synaptic functions. *Journal of Neuroscience*, *28*(50), 13435–13447.

Kalinichenko, S. G., & Pushchin, I. I. (2018). The modular architecture and neurochemical patterns in the cerebellar cortex. *Journal of Chemical Neuroanatomy*, *92*, 16–24.

Käll, L., Storey, J. D., MacCoss, M. J., & Stafford Noble, W. (2008). Assigning significance to peptides identified by tandem mass spectrometry using decoy databases. *Journal of Proteome Research*, *7*(1), 29–34.

Kano, M., Hashimoto, K., Kurihara, H., Watanabe, M., Inoue, Y., Aiba, A., & Tonegawa, S. (1997). Persistent multiple climbing fiber innervation of cerebellar Purkinje cells in mice lacking mGluR1. *Neuron*, *18*(1), 71–79.

Kano, M., & Watanabe, T. (2017). Type-1 metabotropic glutamate receptor signaling in cerebellar Purkinje cells in health and disease. *F1000Research*, *6*(0), 416.

Katz, B., & Miledi, R. (1969). Tetrodotoxin-resistant electric activity in presynaptic terminals. *Journal of Physiology*, *203*(2), 459–487.

Khan, M. A., Khan, S., Windpassinger, C., Badar, M., Nawaz, Z., & Mohammad, R. M. (2016). The molecular genetics of autosomal recessive nonsyndromic intellectual disability: a mutational continuum and future recommendations. *Annals of Human Genetics*, *80*(6), 342–368.

Kiyonaka, S., Wakamori, M., Miki, T., Uriu, Y., Nonaka, M., Bito, H., … Mori, Y. (2007). RIM1 confers sustained activity and neurotransmitter vesicle anchoring to presynaptic Ca2+ channels. *Nature Neuroscience*, *10*(6), 691–701.

Kocsis, J. D., Eng, D. L., & Bhisitkul, R. B. (1984). Adenosine selectively blocks parallel-fiber-mediated synaptic potentials in rat cerebellar cortex. *Proc Natl Acad Sci U S A*, *81*(20), 6531–6534.

Kohl, Z., Ben Abdallah, N., Vogelgsang, J., Tischer, L., Deusser, J., Amato, D., … Winkler, J. (2016). Severely impaired hippocampal neurogenesis associates with an early serotonergic deficit in a BAC α-synuclein transgenic rat model of Parkinson’s disease. *Neurobiology of Disease*, *85*, 206–217.

Koushika, S. P., Richmond, J. E., Hadwiger, G., Weimer, R. M., Jorgensen, E. M., & Nonet, M. L. (2001). A post-docking role for active zone protein Rim. *Nature Neuroscience*, *4*(10), 997–1005.

Kozareva, V., Martin, C., Osorno, T., Rudolph, S., Guo, C., Vanderburg, C., … Macosko, E. (2021). A transcriptomic atlas of mouse cerebellar cortex comprehensively defines cell types. *Nature*, *598*(7879), 214–219.

Kumar, R. A., Sudi, J., Babatz, T. D., Brune, C. W., Oswald, D., Yen, M., … Dobyns, W. B. (2010). A de novo 1p34.2 microdeletion identifies the synaptic vesicle gene RIMS3 as a novel candidate for autism. *Journal of Medical Genetics*, *47*(2), 81–90.

Kusunoki, M., Gottlieb, J., & Goldberg, M. E. (2000). The lateral intraparietal area as a salience map: The representation of abrupt onset, stimulus motion, and task relevance. *Vision Research*, *40*(10–12), 1459–1468.

Lallemand, Y., Luria, V., Haffner-Krausz, R., & Lonai, P. (1998). Maternally expressed PGK-Cre transgene as a tool for early and uniform activation of the Cre site-specific recombinase. *Transgenic Research*, *7*(2), 105–112.

Lalonde, R., & Strazielle, C. (2003). Motor coordination, exploration, and spatial learning in a natural mouse mutation (nervous) with Purkinje cell degeneration. *Behavior Genetics*, *33*(1), 59–66.

Lalouette, A., Guénet, J. L., & Vriz, S. (1998). Hotfoot mouse mutations affect the δ2 glutamate receptor gene and are allelic to lurcher. *Genomics*, *50*(1), 9–13.

Lam, Y. W., & Sherman, S. M. (2010). Functional organization of the somatosensory cortical layer 6 feedback to the thalamus. *Cerebral Cortex*, *20*(1), 13–24.

Larsell, O. (1937). The cerebellum: A review and interpretation. *Archives of Neurology And Psychiatry*, *38*(3), 580–607.

Lazarevic, V., Schöne, C., Heine, M., Gundelfinger, E. D., & Fejtova, A. (2011). Extensive remodeling of the presynaptic cytomatrix upon homeostatic adaptation to network activity silencing. *Journal of Neuroscience*, *31*(28), 10189–10200.

Leblond, C. S., Cliquet, F., Carton, C., Huguet, G., Mathieu, A., Kergrohen, T., … Bourgeron, T. (2019). Both rare and common genetic variants contribute to autism in the Faroe Islands. *Npj Genomic Medicine*, *4*(1).

Lee, H.-Y., Xu, Y., Huang, Y., Ahn, A. H., Auburger, G. W. J., Pandolfo, M., … Ptáček, L. J. (2004). The gene for paroxysmal non-kinesigenic dyskinesia encodes an enzyme in a stress response pathway. *Human Molecular Genetics*, *13*(24), 3161–3170.

Lee, H. Y., Nakayama, J., Xu, Y., Fan, X., Karouani, M., Shen, Y., … Ptaćek, L. J. (2012). Dopamine dysregulation in a mouse model of paroxysmal nonkinesigenic dyskinesia. *Journal of Clinical Investigation*, *122*(2), 507–518.

Lee, Y.-C., Durr, A., Majczenko, K., Huang, Y.-H., Liu, Y.-C., Lien, C.-C., … Soong, B.-W. (2012). Mutations in KCND3 cause spinocerebellar ataxia type 22. *Annals of Neurology*, *72*(6), 859–869.

León, I. R., Schwämmle, V., Jensen, O. N., & Sprenger, R. R. (2013). Quantitative assessment of in-solution digestion efficiency identifies optimal protocols for unbiased protein analysis. *Molecular and Cellular Proteomics*, *12*(10), 2992–3005.

Leto, K., Rolando, C., & Rossi, F. (2012). The genesis of cerebellar GABAergic neurons: Fate potential and specification mechanisms. *Frontiers in Neuroanatomy*, *6*, 1–10.

Liang, F., Zhang, B., Tang, J., Guo, J., Li, W., Ling, E. A., … Cao, Q. (2007). RIM3gamma is a postsynaptic protein in the rat central nervous system. *The Journal of Comparative Neurology*, *503*(4), 501–510.

Liao, Y., Smyth, G. K., & Shi, W. (2014). featureCounts: An efficient general purpose program for assigning sequence reads to genomic features. *Bioinformatics*, *30*(7), 923–930.

Love, M. I., Huber, W., & Anders, S. (2014). Moderated estimation of fold change and dispersion for RNA-seq data with DESeq2. *Genome Biology*, *15*(12), 550.

Luo, L., Ambrozkiewicz, M. C., Benseler, F., Chen, C., Dumontier, E., Falkner, S., … Craig, A. M. (2020). Optimizing nervous system-specific gene targeting with Cre driver lines: Prevalence of germline recombination and influencing factors. *Neuron*, *106*(1), 37-65.e5.

Malone, A., Manto, M., & Hass, C. (2014). Dissecting the links between cerebellum and dystonia. *Cerebellum*, *13*(6), 666–668.

Manning, G., Whyte, D. B., Martinez, R., Hunter, T., & Sudarsanam, S. (2002). The protein kinase complement of the human genome. *Science*, *298*(5600), 1912–1934.

Manto, M., Gandini, J., Feil, K., & Strupp, M. (2020). Cerebellar ataxias : an update. *Current Opinion in Neurology*, *33*(1), 150–160.

Manza, L. L., Stamer, S. L., Ham, A.-J. L., Codreanu, S. G., & Liebler, D. C. (2005). Sample preparation and digestion for proteomic analyses using spin filters. *Proteomics*, *5*(7), 1742–1745.

Marder, E., & Prinz, A. A. (2002). Modeling stability in neuron and network function: The role of activity in homeostasis. *BioEssays*, *24*(12), 1145–1154.

Mark, M. D., Maejima, T., Kuckelsberg, D., Yoo, J. W., Hyde, R. A., Shah, V., … Herlitze, S. (2011). Delayed postnatal loss of P/Q-type calcium channels recapitulates the absence epilepsy, dyskinesia, and ataxia phenotypes of genomic Cacna1A mutations. *Journal of Neuroscience*, *31*(11), 4311–4326.

Martin, M. (2011). Cutadapt removes adapter sequences from high-throughput sequencing reads. *EMBnet.Journal*, 10–12.

Masuda, T., Tomita, M., & Ishihama, Y. (2008). Phase transfer surfactant-aided trypsin digestion for membrane proteome analysis. *Journal of Proteome Research*, *7*(2), 731–740.

Mellacheruvu, D., Wright, Z., Couzens, A. L., Lambert, J.-P., St-Denis, N., Li, T., … Nesvizhskii, A. I. (2013). The CARPome: a contaminant repository for affinity purification mass spectrometry data. *Nature Methods*, *10*(8), 730–736.

Miale, I. L., & Sidman, R. L. (1961). An autoradiographic analysis of histogenesis in the mouse cerebellum. *Experimental Neurology*, *4*, 277–296.

Michel, K., Müller, J. A., Oprişoreanu, A. M., & Schoch, S. (2015). The presynaptic active zone: A dynamic scaffold that regulates synaptic efficacy. *Experimental Cell Research*, *335*(2), 157–164.

Mochida, S., Hida, Y., Tanifuji, S., Hagiwara, A., Hamada, S., Abe, M., … Ohtsuka, T. (2016). SAD-B phosphorylation of CAST controls active zone vesicle recycling for synaptic depression. *Cell Reports*, *16*(11), 2901–2913.

Molgaard, S., Ulrichsen, M., Boggild, S., Holm, M.-L., Vaegter, C., Nyengaard, J., & Glerup, S. (2014). Immunohistochemical visualization of mouse interneuron subtypes. *F1000Research*, *3*, 242.

Molinari, M., Filippini, V., & Leggio, M. G. (2002). Neuronal plasticity of interrelated cerebellar and cortical networks. *Neuroscience*, *111*(4), 863–870.

Mori, Y., Friedrich, T., Kim, M.-S., Mikami, A., Nakai, J., Ruth, P., … Numa, S. (1991). Primary structure and functional expression from complementary DNA of a brain calcium channel. *Nature*, *350*(6317), 398–402.

Mori, Y., Wakamori, M., Oda, S.-I., Fletcher, C. F., Sekiguchi, N., Mori, E., … Imoto, K. (2000). Reduced voltage sensitivity of activation of P/Q-type Ca2+ channels is associated with the ataxic mouse mutation rolling Nagoya (tg(rol)). *Journal of Neuroscience*, *20*(15), 5654–5662.

Mugnaini, E., Sekerková, G., & Martina, M. (2011). The unipolar brush cell: A remarkable neuron finally receiving deserved attention. *Brain Research Reviews*, *66*(1–2), 220–245.

Mullen, R. J., Eicher, E. M., & Sidman, R. L. (1976). Purkinje cell degeneration, a new neurological mutation in the mouse. *Proc Natl Acad Sci U S A*, *73*(1), 208–212.

Müller, J. A., Betzin, J., Santos-Tejedor, J., Mayer, A., Oprişoreanu, A. M., Engholm-Keller, K., … Schoch, S. (2022). A presynaptic phosphosignaling hub for lasting homeostatic plasticity. *Cell Reports*, *39*(3), 110696.

Müller, M., & Davis, G. W. (2012). Transsynaptic control of presynaptic Ca2+ influx achieves homeostatic potentiation of neurotransmitter release. *Current Biology*, *22*(12), 1102–1108.

Müller, M., Liu, K. S. Y., Sigrist, S. J., & Davis, G. W. (2012). RIM controls homeostatic plasticity through modulation of the readily-releasable vesicle pool. *Journal of Neuroscience*, *32*(47), 16574–16585.

Murthy, V. N., Schikorski, T., Stevens, C. F., & Zhu, Y. (2001). Inactivity produces increases in neurotransmitter release and synapse size. *Neuron*, *32*(4), 673–682.

Nahidiazar, L., Agronskaia, A. V., Broertjes, J., Van Broek, B. Den, & Jalink, K. (2016). Optimizing imaging conditions for demanding multi-color super resolution localization microscopy. *PLoS ONE*, *11*(7), 1–18.

Nakazawa, K., Zsiros, V., Jiang, Z., Nakao, K., Kolata, S., Zhang, S., & Belforte, J. E. (2012). GABAergic interneuron origin of schizophrenia pathophysiology. *Neuropharmacology*, *62*(3), 1574–1583.

Nehlig, A., Daval, J.-L., & Debry, G. (1992). Caffeine and the central nervous system: mechanisms of action, biochemical, metabolic and psychostimulant effects. *Brain Research Reviews*, *17*(2), 139–170.

Nguyen, P. V., & Woo, N. H. (2003). Regulation of hippocampal synaptic plasticity by cyclic AMP-dependent protein kinases. *Progress in Neurobiology*, *71*(6), 401–437.

Nieratschker, V., Schubert, A., Jauch, M., Bock, N., Bucher, D., Dippacher, S., … Buchner, E. (2009). Bruchpilot in ribbon-like axonal agglomerates, behavioral defects, and early death in SRPK79D kinase mutants of Drosophila. *PLoS Genetics*, *5*(10), e1000700.

Nishimura, Y., Martin, C. L., Vazquez-Lopez, A., Spence, S. J., Alvarez-Retuerto, A. I., Sigman, M., … Geschwind, D. H. (2007). Genome-wide expression profiling of lymphoblastoid cell lines distinguishes different forms of autism and reveals shared pathways. *Human Molecular Genetics*, *16*(14), 1682–1698.

Noebels, J. L., & Sidman, R. L. (1979). Inherited epilepsy: Spike-wave and focal motor seizures in the mutant mouse tottering. *Science*, *204*(4399), 1334–1336.

Oda, S. (1973). The observation of rolling mouse Nagoya (rol), a new neurological mutant, and its maintenance. *Jikken Dobutsu*, *22*(4), 281–288.

Ohtsuka, T., Takao-Rikitsu, E., Inoue, E., Inoue, M., Takeuchi, M., Matsubara, K., … Takai, Y. (2002). CAST: A novel protein of the cytomatrix at the active zone of synapses that forms a ternary complex with RIM1 and Munc13-1. *Journal of Cell Biology*, *158*(3), 577–590.

Ophoff, R. A., Terwindt, G. M., Vergouwe, M. N., van Eijk, R., Oefner, P. J., Hoffman, S. M. G., … Frants, R. R. (1996). Familial hemiplegic migraine and episodic ataxia type-2 are caused by mutations in the Ca2+ channel gene CACNL1A4. *Cell*, *87*(3), 543–552.

Pageon, S. V., Nicovich, P. R., Mollazade, M., Tabarin, T., & Gaus, K. (2016). Clus-DoC: A combined cluster detection and colocalization analysis for single-molecule localization microscopy data. *Molecular Biology of the Cell*, *27*(22), 3627–3636.

Perlman, S. L. (2000). Cerebellar ataxia. *Current Treatment Options in Neurology*, *2*, 215–224.

Pers, T. H., Timshel, P., Ripke, S., Lent, S., Sullivan, P. F., O’Donovan, M. C., … Hirschhorn, J. N. (2016). Comprehensive analysis of schizophrenia-associated loci highlights ion channel pathways and biologically plausible candidate causal genes. *Human Molecular Genetics*, *25*(6), 1247–1254.

Picher, M. M., Oprisoreanu, A.-M., Jung, S., Michel, K., Schoch, S., & Moser, T. (2017). Rab interacting molecules 2 and 3 directly interact with the pore-forming CaV1.3 Ca2+ channel subunit and promote its membrane expression. *Frontiers in Cellular Neuroscience*, *11*, 160.

Plumel, M., Dumont, S., Maes, P., Sandu, C., Felder-Schmittbuhl, M.-P., Challet, E., & Bertile, F. (2019). Circadian analysis of the mouse cerebellum proteome. *International Journal of Molecular Sciences*, *20*(8), 1852.

Powell, C. M., Schoch, S., Monteggia, L., Barrot, M., Matos, M. F., Feldmann, N., … Nestler, E. J. (2004). The presynaptic active zone protein RIM1a is critical for normal learning and memory. *Neuron*, *42*(1), 143–153.

Raike, R. S., Hess, E. J., & Jinnah, H. A. (2015). Dystonia and cerebellar degeneration in the leaner mouse mutant. *Brain Research*, *1611*, 56–64.

Rajakulendran, S., Kaski, D., & Hanna, M. G. (2012). Neuronal P/Q-type calcium channel dysfunction in inherited disorders of the CNS. *Nature Reviews Neurology*, *8*(2), 86–96.

Ritchie, M. E., Phipson, B., Wu, D., Hu, Y., Law, C. W., Shi, W., & Smyth, G. K. (2015). limma powers differential expression analyses for RNA-sequencing and microarray studies. *Nucleic Acids Research*, *43*(7), e47.

Roostaei, T., Nazeri, A., Sahraian, M. A., & Minagar, A. (2014). The human cerebellum: A review of physiologic neuroanatomy. *Neurologic Clinics*, *32*(4), 859–869.

Rust, M. J., Bates, M., & Zhuang, X. (2006). Sub-diffraction-limit imaging by stochastic optical reconstruction microscopy (STORM). *Nature Methods*, *3*(10), 793–795.

Saab, C. Y., & Willis, W. D. (2003). The cerebellum: Organization, functions and its role in nociception. *Brain Research Reviews*, *42*(1), 85–95.

Sausbier, M., Hu, H., Arntz, C., Feil, S., Kamm, S., Adelsberger, H., … Ruth, P. (2004). Cerebellar ataxia and Purkinje cell dysfunction caused by Ca2+-activated K+ channel deficiency. *Proc Natl Acad Sci U S A*, *101*(25), 9474–9478.

Schanzenbächer, C. T., Sambandan, S., Langer, J. D., & Schuman, E. M. (2016). Nascent proteome remodeling following homeostatic scaling at hippocampal synapses. *Neuron*, *92*(2), 358–371.

Schaukovitch, K., Reese, A. L., Kim, S.-K., Kilaru, G., Joo, J.-Y., Kavalali, E. T., & Kim, T.-K. (2017). An intrinsic transcriptional program underlying synaptic scaling during activity suppression. *Cell Reports*, *18*(6), 1512–1526.

Scheu, S., Ali, S., Ruland, C., Arolt, V., & Alferink, J. (2017). The C-C chemokines CCL17 and CCL22 and their receptor CCR4 in CNS autoimmunity. *International Journal of Molecular Sciences*, *18*(11), 2306.

Schindelin, J., Arganda-Carreras, I., Frise, E., Kaynig, V., Longair, M., Pietzsch, T., … Cardona, A. (2012). Fiji: An open-source platform for biological-image analysis. *Nature Methods*, *9*(7), 676–682.

Schmolesky, M. T., Weber, J. T., De Zeeuw, C. I., & Hansel, C. (2002). The making of a complex spike: Ionic composition and plasticity. *Annals of the New York Academy of Sciences*, *978*, 359–390.

Schnitzbauer, J., Strauss, M. T., Schlichthaerle, T., Schueder, F., & Jungmann, R. (2017). Super-resolution microscopy with DNA-PAINT. *Nature Protocols*, *12*(6), 1198–1228.

Schoch, S., Castillo, P. E., Jo, T., Mukherjee, K., Geppert, M., Wang, Y., … Südhof, T. C. (2002). RIM1alpha forms a protein scaffold for regulating neurotransmitter release at the active zone. *Nature*, *415*(6869), 321–326.

Schoch, S., & Gundelfinger, E. D. (2006). Molecular organization of the presynaptic active zone. *Cell and Tissue Research*, *326*(2), 379–391.

Schoch, S., Mittelstaedt, T., Kaeser, P. S., Padgett, D., Feldmann, N., Chevaleyre, V., … Südhof, T. C. (2006). Redundant functions of RIM1α and RIM2α in Ca2+-triggered neurotransmitter release. *EMBO Journal*, *25*(24), 5852–5863.

Scholle, H. C., Jinnah, H. A., Arnold, D., Biedermann, F. H. W., Faenger, B., Grassme, R., … Schumann, N. P. (2010). Kinematic and electromyographic tools for characterizing movement disorders in mice. *Movement Disorders*, *25*(3), 265–274.

Shen, Y., Ge, W. P., Li, Y., Hirano, A., Lee, H. Y., Rohlmann, A., … Ptáček, L. J. (2015). Protein mutated in paroxysmal dyskinesia interacts with the active zone protein RIM and suppresses synaptic vesicle exocytosis. *Proc Natl Acad Sci U S A*, *112*(10), 2935–2941.

Sidman, R. L., Lane, P. W., & Dickie, M. M. (1962). Staggerer, a new mutation in the mouse affecting the cerebellum. *Science*, *137*(3530), 610–612.

Smets, K., Duarri, A., Deconinck, T., Ceulemans, B., van de Warrenburg, B. P., Züchner, S., … Baets, J. (2015). First de novo KCND3 mutation causes severe Kv4.3 channel dysfunction leading to early onset cerebellar ataxia, intellectual disability, oral apraxia and epilepsy. *BMC Medical Genetics*, *16*, 51.

Snell, G. D. (1955). Ducky, a new second chromosome mutation in the mouse. *Journal of Heredity*, *46*(1), 27–29.

Soderling, T. R. (2000). CaM-kinases: Modulators of synaptic plasticity. *Current Opinion in Neurobiology*, *10*(3), 375–380.

Song, J. Y., Ichtchenko, K., Südhof, T. C., & Brose, N. (1999). Neuroligin 1 is a postsynaptic cell-adhesion molecule of excitatory synapses. *Proc Natl Acad Sci U S A*, *96*(3), 1100–1105.

Stettler, O., Moya, K. L., Zahraoui, A., & Tavitian, B. (1994). Developmental changes in the localization of the synaptic vesicle protein rab3A in rat brain. *Neuroscience*, *62*(2), 587–600.

Südhof, T. C. (2012). The presynaptic active zone. *Neuron*, *75*(1), 11–25.

Takada, Y., Hirano, M., Kiyonaka, S., Ueda, Y., Yamaguchi, K., Nakahara, K., … Mori, Y. (2015). Rab3 interacting molecule 3 mutations associated with autism alter regulation of voltage-dependent Ca2+ channels. *Cell Calcium*, *58*(3), 296–306.

Tang, A.-H., Chen, H., Li, T. P., Metzbower, S. R., MacGillavry, H. D., & Blanpied, T. A. (2016). A trans-synaptic nanocolumn aligns neurotransmitter release to receptors. *Nature*, *536*(7615), 210–214.

Tara, E., Vitenzon, A., Hess, E., & Khodakhah, K. (2018). Aberrant cerebellar Purkinje cell activity as the cause of motor attacks in a mouse model of episodic ataxia type 2. *Disease Models & Mechanisms*, *11*(9), dmm034181.

Testa, G., Schaft, J., Van Der Hoeven, F., Glaser, S., Anastassiadis, K., Zhang, Y., … Stewart, A. F. (2004). A reliable lacZ expression reporter cassette for multipurpose, knockout-first alleles. *Genesis*, *38*(3), 151–158.

Thompson, R. E., Larson, D. R., & Webb, W. W. (2002). Precise nanometer localization analysis for individual fluorescent probes. *Biophysical Journal*, *82*(5), 2775–2783.

Tinevez, J.-Y., Perry, N., Schindelin, J., Hoopes, G. M., Reynolds, G. D., Laplantine, E., … Eliceiri, K. W. (2017). TrackMate: An open and extensible platform for single-particle tracking. *Methods*, *115*(2017), 80–90.

tom Dieck, S., Sanmartí-Vila, L., Langnaese, K., Richter, K., Kindler, S., Soyke, A., … Gundelfinger, E. D. (1998). Bassoon, a novel zinc-finger CAG/glutamine-repeat protein selectively localized at the active zone of presynaptic nerve terminals. *Journal of Cell Biology*, *142*(2), 499–509.

Torres, V. I., & Inestrosa, N. C. (2018). Vertebrate presynaptic active zone assembly: A role accomplished by diverse molecular and cellular mechanisms. *Molecular Neurobiology*, *55*(6), 4513–4528.

Torres, V. I., Vallejo, D., & Inestrosa, N. C. (2017). Emerging synaptic molecules as candidates in the etiology of neurological disorders. *Neural Plasticity*, *2017*, 8081758.

Tsuji, S., & Meier, H. (1971). Evidence for allelism of leaner and tottering in the mouse. *Genetical Research*, *17*(1), 83–88.

Turrigiano, G. G., Leslie, K. R., Desai, N. S., Rutherford, L. C., & Nelson, S. B. (1998). Activity-dependent scaling of quantal amplitude in neocortical neurons. *Nature*, *391*(6670), 892–896.

Turrigiano, G. G., & Nelson, S. B. (2004). Homeostatic plasticity in the developing nervous system. *Nature Reviews Neuroscience*, *5*(2), 97–107.

Unterberger, I., & Trinka, E. (2008). Diagnosis and treatment of paroxysmal dyskinesias revisited. *Therapeutic Advances in Neurological Disorders*, *1*(2), 4–11.

Uriu, Y., Kiyonaka, S., Miki, T., Yagi, M., Akiyama, S., Mori, E., … Mori, Y. (2010). Rab3-interacting molecule γ isoforms lacking the Rab3-binding domain induce long lasting currents but block neurotransmitter vesicle anchoring in voltage-dependent P/Q-type Ca2+ channels. *Journal* *of Biological Chemistry*, *285*(28), 21750–21767.

Varadi, G., Lory, P., Schultz, D., Varadi, M., & Schwartz, A. (1991). Acceleration of activation and inactivation by the β subunit of the skeletal muscle calcium channel. *Nature*, *352*(6331), 159–162.

Voogd, J., Gerrits, N. M., & Ruigrok, T. J. H. (1996). Organization of the vestibulocerebellum. *Annals of the New York Academy of Sciences*, *781*, 553–579.

Wagh, D. A., Rasse, T. M., Asan, E., Hofbauer, A., Schwenkert, I., Dürrbeck, H., … Buchner, E. (2006). Bruchpilot, a protein with homology to ELKS/CAST, is required for structural integrity and function of synaptic active zones in Drosophila. *Neuron*, *49*(6), 833–844.

Walter, J. T., Alviña, K., Womack, M. D., Chevez, C., & Khodakhah, K. (2006). Decreases in the precision of Purkinje cell pacemaking cause cerebellar dysfunction and ataxia. *Nature Neuroscience*, *9*(3), 389–397.

Wang, X., Hu, B., Zieba, A., Neumann, N. G., Kasper-Sonnenberg, M., Honsbein, A., … Kilimann, M. W. (2009). A protein interaction node at the neurotransmitter release site: Domains of aczonin/piccolo, bassoon, CAST, and RIM converge on the N-terminal domain of Munc13-1. *Journal of Neuroscience*, *29*(40), 12584–12596.

Wang, Y., Liu, X., Biederer, T., & Südhof, T. C. (2002). A family of RIM-binding proteins regulated by alternative splicing: Implications for the genesis of synaptic active zones. *Proc Natl Acad Sci U S A*, *99*(22), 14464–14469.

Wang, Y., Okamoto, M., Schmitz, F., Hofmann, K., & Südhof, T. C. (1997). RIM is a putative Rab3 effector in regulating synaptic-vesicle fusion. *Nature*, *388*(6642), 593–598.

Wang, Y., & Südhof, T. C. (2003). Genomic definition of RIM proteins: Evolutionary amplification of a family of synaptic regulatory proteins. *Genomics*, *81*(2), 126–137.

Weidenhofer, J., Bowden, N. A., Scott, R. J., & Tooney, P. A. (2006). Altered gene expression in the amygdala in schizophrenia: Up-regulation of genes located in the cytomatrix active zone. *Molecular and Cellular Neuroscience*, *31*(2), 243–250.

Weidenhofer, J., Scott, R. J., & Tooney, P. A. (2009). Investigation of the expression of genes affecting cytomatrix active zone function in the amygdala in schizophrenia: Effects of antipsychotic drugs. *Journal of Psychiatric Research*, *43*(3), 282–290.

Westenbroek, R. E., Sakurai, T., Elliott, E. M., Hell, J. W., Starr, T. V., Snutch, T. P., & Catterall, W. A. (1995). Immunochemical identification and subcellular distribution of the alpha 1A subunits of brain calcium channels. *Journal of Neuroscience*, *15*(10), 6403–6418.

Wiśniewski, J. R., Zougman, A., Nagaraj, N., & Mann, M. (2009). Universal sample preparation method for proteome analysis. *Nature Methods*, *6*(5), 359–362.

Wizeman, J. W., Guo, Q., Wilion, E. M., & Li, J. Y. H. (2019). Specification of diverse cell types during early neurogenesis of the mouse cerebellum. *ELife*, *8*, 1–24.

Wojcik, W. J., & Neff, N. H. (1983). Adenosine A1 receptors are associated with cerebellar granule cells. *Journal of Neurochemistry*, *41*(3), 759–763.

Womack, M. D., Chevez, C., & Khodakhah, K. (2004). Calcium-activated potassium channels are selectively coupled to P/Q-type calcium channels in cerebellar Purkinje neurons. *Journal of Neuroscience*, *24*(40), 8818–8822.

Wu, B., Blot, F. G. C., Wong, A. B., Osório, C., Adolfs, Y., Pasterkamp, R. J., … Schonewille, M. (2019). TRPC3 is a major contributor to functional heterogeneity of cerebellar Purkinje cells. *ELife*, *8*, e45590.

Xie, G., Clapcote, S. J., Nieman, B. J., Tallerico, T., Huang, Y., Vukobradovic, I., … Roder, J. C. (2007). Forward genetic screen of mouse reveals dominant missense mutation in the P/Q-type voltage-dependent calcium channel, CACNA1A. *Genes, Brain and Behavior*, *6*(8), 717–727.

Zeisel, A., Hochgerner, H., Lönnerberg, P., Johnsson, A., Memic, F., van der Zwan, J., … Linnarsson, S. (2018). Molecular architecture of the mouse nervous system. *Cell*, *174*(4), 999-1014.e22.

Zürner, M., Mittelstaedt, T., tom Dieck, S., Becker, A., & Schoch, S. (2011). Analyses of the spatiotemporal expression and subcellular localization of liprin-α proteins. *Journal of Comparative Neurology*, *519*(15), 3019–3039.

Zwingman, T. A., Neumann, P. E., Noebels, J. L., & Herrup, K. (2001). Rocker is a new variant of the voltage-dependent calcium channel gene Cacna1a. *Journal of Neuroscience*, *21*(4), 1169–1178.

Books:

Ebner T.J., Chen G. (2013) Tottering Mouse. In: Manto M., Schmahmann J.D., Rossi F., Gruol D.L., Koibuchi N. (eds) Handbook of the Cerebellum and Cerebellar Disorders. Springer, Dordrecht

Flourens, P. (1824) Recherches Expérimentales sur les Propriétés et les Fonctions du Systém Merveux dans les Animaux Vertébres. Paris: Crevot.

Kandel, E.R., Schwartz, J.H., Jessell, T.M., Siegelbaum, S.A., Hudspeth, A.J., Mack, S. (2013). Principles of neural science (Fifth edition.). New York, N.Y.: McGraw-Hill Education LLC.

Purves D., Augustine G.J., Fitzpatrick D., et al., editors. (2001) Organization of the Cerebellum. Neuroscience. 2nd edition. Sunderland (MA): Sinauer Associates; Available from: https://www.ncbi.nlm.nih.gov/books/NBK11132/

14 Acknowledgements

The realization of this Ph.D. thesis would not have been possible without the help and support of others. Therefore, I would like to express my gratitude to all people who contributed to this work.

I would like to thank Prof. Dr. Susanne Schoch McGovern for giving me the opportunity to work on this versatile project and to provide me with help and guidance whenever needed.

I would like to cordially thank Prof. Dr. Albert Haas for being the second assessor of my Ph.D. thesis.

I would like to thank Prof. Dr. Dirk Dietrich for the co-supervision of my Ph.D. thesis.

I would like to thank Assistant Prof. Dr. Laura A. Ewell for all the help and support in the *in vivo* studies of my Ph.D. thesis. I would like to thank you for writing all the code for the analysis and for all the time you spent for this project.

I would like to thank the whole AG Schoch/Becker and AG Dietrich with all the current and past members for all your support and help throughout my time in the lab. You made work always enjoyable and fun. Especially, I would like to thank Julia for being the best office-room mate, for the RIM/ELKS/STORM discussions and the very scientific conversations about road bikes and football. Thank you to Annika, Despina, Idil and Annachiara for offering help whenever needed and for always listening to my complains about mice and experiments. I would like to thank Hyuntae for being a great co-worker on the RIM4 project and for sharing thoughts and hypotheses as well as for the help in answering scientific questions.

I would like to thank my family and friends for supporting me at any time and for being always there whenever I needed help or just somebody to talk to. Most importantly, I would like to thank Björn for all your support and motivation, understanding and patience.